JUSTUS-LIEBIG-
UNIVERSITÄT
GIESSEN

A Novel Method for the Measurement of Half-Lives and Decay Branching Ratios of Exotic Nuclei with the FRS Ion Catcher

Inauguraldissertation zur Erlangung des Doktorgrades der
Naturwissenschaftlichen Fakultät der Justus-Liebig-Universität Gießen

vorgelegt von

Ivan Miskun
geboren in Selenogorsk, Russland

Fachbereich 07 - Mathematik und Informatik, Physik, Geographie

II. Physikalisches Institut Justus-Liebig-Universität Gießen

Gießen 2019

Selbstständigkeitserklärung

Ich erkläre: Ich habe die vorgelegte Dissertation selbständig und ohne unerlaubte fremde Hilfe und nur mit den Hilfen angefertigt, die ich in der Dissertation angegeben habe. Alle Textstellen, die wörtlich oder sinngemäß aus veröffentlichten Schriften entnommen sind, und alle Angaben, die auf mündlichen Auskünften beruhen, sind als solche kenntlich gemacht. Ich stimme einer evtl. Überprüfung meiner Dissertation durch eine Antiplagiat-Software zu. Bei den von mir durchgeführten und in der Dissertation erwähnten Untersuchungen habe ich die Grundsätze guter wissenschaftlicher Praxis, wie sie in der „Satzung der Justus-Liebig-Universität Gießen zur Sicherung guter wissenschaftlicher Praxis“ niedergelegt sind, eingehalten.

Datum	Ivan Miskun

Erstgutachter: Prof. Dr. Christoph Scheidenberger
Zweitgutachter: Prof. Dr. Dr. h.c. Hans Geissel

Contents

Motivation and goals

One of the main questions of modern nuclear astrophysics is the origin of the chemical elements heavier than iron. There is strong evidence that these elements are mainly produced in three astrophysical nucleosynthesis processes: *s*-, *p*-, and *r*-processes [Iliadis, 2015]. Whereas the *s*- and *p*-processes are relatively well investigated and understood, the *r*-process is still a hot topic of experimental and theoretical studies. In order to improve the understanding of the *r*-process, the physical conditions and astronomical sites have to be accurately identified. They are studied by means of astronomical observations and modeling of stellar processes and explosions. A particular example is the observation of the neutron-star merger event in 2017, GW170817, which has triggered a lot of progress [Abbott et al., 2017, Pian et al., 2017]. In addition, accurate knowledge of nuclear properties of very exotic neutron-rich nuclei is required. Masses, half-lives, and decay branching ratios of these nuclei are an essential input to the complex astrophysical models. However, as the *r*-process path lies far away from the valley of stability, the desired nuclei are very challenging to access experimentally due to their short half-lives and low production cross sections. Experimental data are scarce, especially for the decay branching ratios. There is a need for new complementary measurement techniques, which pave the way towards a better understanding of the origin of the matter in the Universe.

The main goal of this work is to develop, implement and use a novel method for the measurement of half-lives and decay branching ratios of exotic nuclei at the FRS Ion Catcher experiment [Plaß et al., 2013a] located at the GSI accelerator facility in Darmstadt, Germany. The method comprises the first ever use of a gas-filled cryogenic stopping cell (CSC) [Ranjan et al., 2011, Reiter, 2015, Ranjan et al., 2015] as an ion trap for controllable storage of the ions of interest and retrapping of their decay recoils. The mother and daughter nuclides are simultaneously extracted out of the CSC, measured, identified, and counted with a multiple-reflection time-of-flight mass spectrometer (MR-TOF-MS) [Plaß et al., 2008a, Dickel, 2010, Dickel et al., 2015b]. From the measured abundances, the half-life and decay branching ratios of the mother nuclide are deduced. A unique combination of performance characteristics of the fragment separator (FRS) [Geissel et al., 1992a] used for in-flight production and separation of exotic nuclei, of the CSC and of the MR-TOF-MS results in a fast, efficient and universal measurement technique. Its important advantage is that, unlike the conventional methods, it does not rely on the detection of light particles emitted in decay, which gives rise to significant systematic uncertainties, but on the detection of the produced daughter nuclides.

The goals of this doctoral thesis are to implement the mentioned method at the FRS

Ion Catcher and to perform systematic investigations and pilot measurements. This requires additional technical upgrades of the existing setup and detailed characterization of the system performance. Therefore, this work also addresses such aspects as improvement of the total efficiency of the FRS Ion Catcher, enhancement of the selectivity of ion transport, and implementation of new calibrant ion sources. The cleanliness of the CSC, optimal and efficient stopping, extraction, and delivery of ions for high-resolution mass measurements with the MR-TOF-MS are as well among the subjects investigated within the frames of this thesis. These upgrades and investigations are essential for the preparation of the FRS Ion Catcher for the upcoming experiments in the FAIR Phase-0 campaign in 2019 and 2020.

1 Experiments with exotic nuclei

The ordinary matter in our Universe consists of atoms. Atoms are composed of a positively-charged nucleus built from protons and neutrons and negatively-charged electrons revolving around it. A neutral atom contains the same number of electrons and protons. This number is called the atomic number Z and it defines the chemical properties of the atom. Atoms that have the same number of protons Z but a different number of neutrons N are called isotopes of the chemical element X and are denoted as ${}^{A}_{Z}X$, where $A = Z + N$ is the mass number.

All isotopes of all chemical elements, measured and predicted to exist, are plotted on the so-called nuclide chart shown in Fig. 1.1. The isotopes that have already been measured are plotted in yellow, whereas the predicted ones are depicted in green. Depending on the number of protons and neutrons contained in a nucleus, the isotopes can be stable or unstable. Stable isotopes are plotted in Fig. 1.1 in black. This region of the nuclide chart is called the valley of stability. For higher atomic masses, the valley of stability shifts towards larger N/Z due to the increasing Coulomb repulsion between protons in the atomic nucleus. Unstable isotopes undergo radioactive decay in order to obtain a more stable configuration. Neutron and proton drip lines are shown on the nuclide chart as dashed lines. They indicate the boundaries of positive one-nucleon separation energies S_n and S_p correspondingly. Beyond the drip lines, S_n and S_p values are negative, and the nuclides decay by nucleon emission. Nuclei with a very unusual N/Z ratio, lying far away from the valley of stability, are called the exotic nuclei. They are of particular scientific interest due to their novel properties like new modes of radioactive decay or peculiar nuclear structure effects. Exotic nuclei are very short-lived, they do not exist on Earth and are produced in laboratories or stars, star explosions, and neutron star mergers.

The origin of matter in the Universe is still one of the most important questions for nuclear astrophysics. Chemical elements up to iron can be forged in exothermic fusion reactions occurring in the stars. There is strong evidence that elements above iron mainly produced in three astrophysical nucleosynthesis processes: s-process (slow neutron capture), r-process (rapid neutron capture), and p-process (proton capture) [Iliadis, 2015].

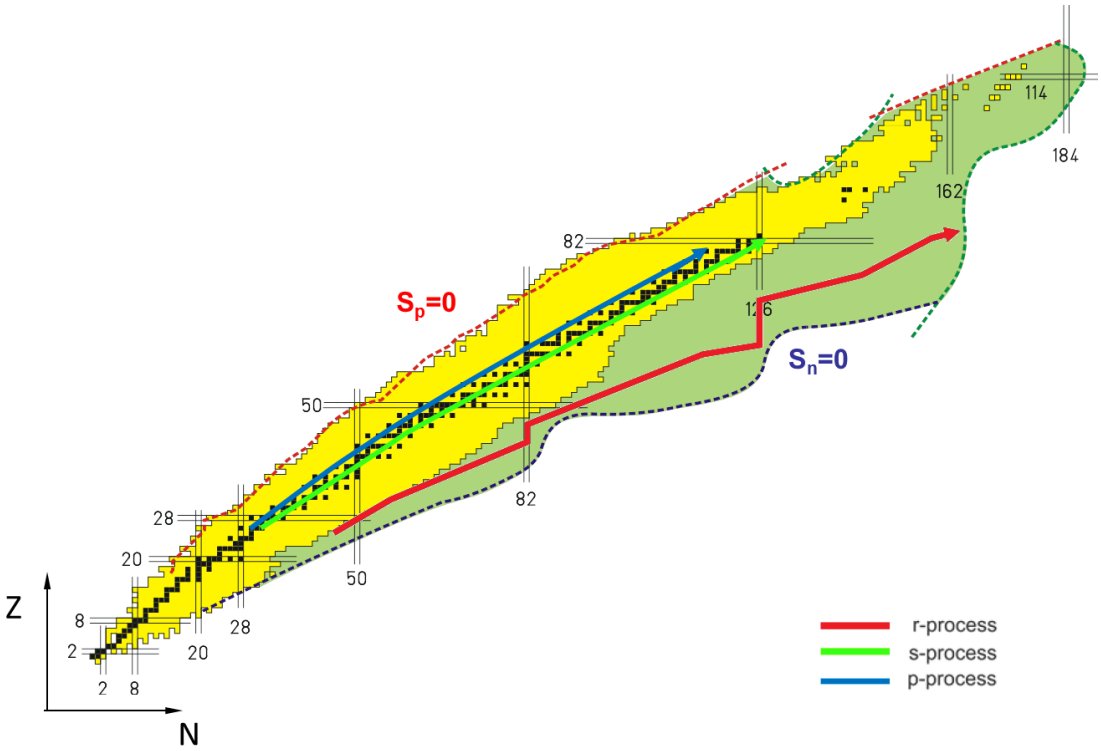

Figure 1.1: Chart of the nuclides with schematically depicted s-, r-, and p- nucleosynthesis processes. Measured isotopes are plotted in yellow; isotopes predicted to exist – in green; stable isotopes – in black. Drip lines are shown as dashed lines.

1.1 Role of exotic nuclei

As can be seen from Fig. 1.1, the s- and p-processes are going along the valley of stability or in its proximity. They can be studied from the properties of stable and close-to-stable nuclei and, therefore, are relatively well understood. On the other hand, the r-process path lies far away from the valley of stability close to the neutron drip line. For a better understanding of the r-process, accurate knowledge of nuclear properties of very exotic nuclei is required.

In the r-process, nuclei rapidly capture free neutrons until the equilibrium between the neutron capture (n, γ) and photodisintegration (γ, n) reactions is reached and then undergo β^--decay moving to higher Z. The equilibrium point depends on the stellar environment and the neutron separation energy S_n, which can be calculated from the masses of the isotope of interest ${}^{A}_{Z}X$ and its neighbor ${}^{A-1}_{Z}X$. In the regions of enhanced stability, e.g. the closed neutron shells at $N = 50$, 82, and 126, a buildup of the nuclei occurs. In the late stage of the process, all exotic nuclei distributed along the nucleosynthesis path decay towards the stability valley by β^--decay and β-delayed neutron emission. In order to calculate the resulting abundances of stable isotopes produced in the r-process, it is necessary to know half-lives of exotic nuclei determining the abundances distribution along the nucleosynthesis path and their

decay branching ratios. Branching between β^--decay and β-delayed neutron emission not only determines the decay path of nuclei towards the stability but also affects the nucleosynthesis process dynamics by supplying additional free neutrons.

In order to improve the understanding of the r-process, network calculation models are developed, which use masses, half-lives, decay branching ratios, and fission barriers as input parameters. However, experimental data are scarce, as exotic nuclei are very challenging to study due to their short half-lives and low production cross sections. Therefore, there is a need for novel, fast, efficient, accurate, and precise measurement techniques to provide the essential input for the theoretical calculations.

1.2 Production and separation of exotic nuclides

Exotic nuclei do not exist on Earth and, therefore, have to be produced at accelerator facilities. They are produced in nuclear reactions occurring when an accelerated primary beam impinges on a target. Depending on the energy of the primary beam and the impact parameter value, different nuclear reactions may occur, such as fusion, fission, and fragmentation. Production cross sections are defined by the type of nuclear reaction and by the selected combination of projectile and target nuclides. After the exotic nuclei have been produced, they have to be separated and delivered to different experiments. The challenge of this task lies in small production cross sections and short half-lives of the nuclides of interest. There are two main approaches used at accelerator laboratories around the world for production and separation of exotic nuclei: the isotope separation on-line (ISOL) method and the in-flight method [Geissel et al., 1995, Blumenfeld et al., 2013]. They are discussed in details in the following subsections.

1.2.1 Isotope separation on-line method

At an ISOL facility, the exotic nuclei are produced in target fission and fragmentation (also called spallation) reactions. The outline of this method is shown in Fig. 1.2. A proton beam of high energy (up to 1 GeV) and intensity (up to 100 μA) impinges on a thick target. The nuclei produced by spallation diffuse out of the hot target and get ionized by an ion source. Then, they are accelerated to energies of 10-100 keV, separated in an electromagnetic separator and delivered to low-energy experiments. After the separation, the ions can also be further accelerated and used for the production of exotic nuclei in a secondary target.

The ISOL method has certain advantages and disadvantages compared to the in-flight method. Proton primary beams can be produced with high intensities, which results in high production rates of the exotic nuclei. Besides, the ions of interest are extracted out of the target at low energies and, therefore, are available for high-accuracy low-

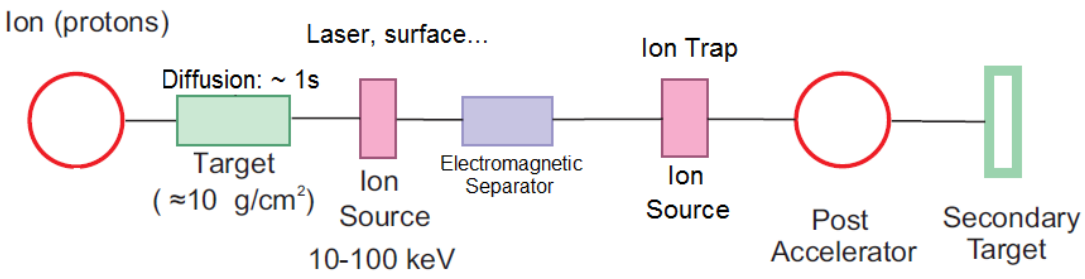

Figure 1.2: Schematic figure of the isotope separation on-line (ISOL) method [Geissel et al., 1995].

energy experiments. On the other hand, the diffusion process is slow (ions extraction out of the target might take up to 1 s) and element-dependent. Only the isotopes of non-refractory elements with half-lives longer than ~ 10 ms may be extracted and delivered to the experiments. An example of production yields at the ISOL facility is shown in the top part of Fig. 1.3 [Reiter, 2015]. Here, the isotope production yields experimentally measured at ISOLDE, CERN are depicted [ISOLDE, 2015]. Also, due to the low energy of the ions, the electromagnetic separator has a mass resolving power of ~ 2000 only. This complicates particle identification of the ion beam and may lead to severe isobaric contamination of the ions of interest.

1.2.2 In-flight method

The in-flight method is complementary to the ISOL method. At an in-flight facility, primary heavy-ion beams of high kinetic energies bombard a thin target producing exotic nuclei in projectile fusion, fission and fragmentation reactions. The products emerge from the target with high kinetic energies and can be further guided and separated by electric and magnetic fields. A schematic figure of the in-flight method is shown in Fig. 1.4.

Primary beams of energies close to the Coulomb barrier (~ 5 MeV/u) are used to produce exotic nuclei in a fusion reaction. The projectile and target nuclei fuse and form a compound nucleus, which de-excites by evaporating a few nucleons. The products can be separated from the primary beam by electric and magnetic fields, e.g. by a velocity filter, and then are transported towards the experiments.

Heavy-ion beams accelerated to relativistic energies of up to 1-1.5 GeV/u are used for the production of exotic nuclei in projectile fragmentation or projectile fission reactions. These reactions are shown schematically in Fig. 1.5. In the fragmentation reaction (Fig. 1.5a), a part of a projectile nucleus is abrased on a light nucleus of the target material, e.g. beryllium. The rest part de-excites by evaporating a few nucleons (the process, which is also called ablation) and emitting gamma rays resulting in a fragmentation product. If the excitation energy of the nucleus is too high, it may undergo fission reaction after the abrasion (Fig. 1.5b). Fission of the projectile nucleus

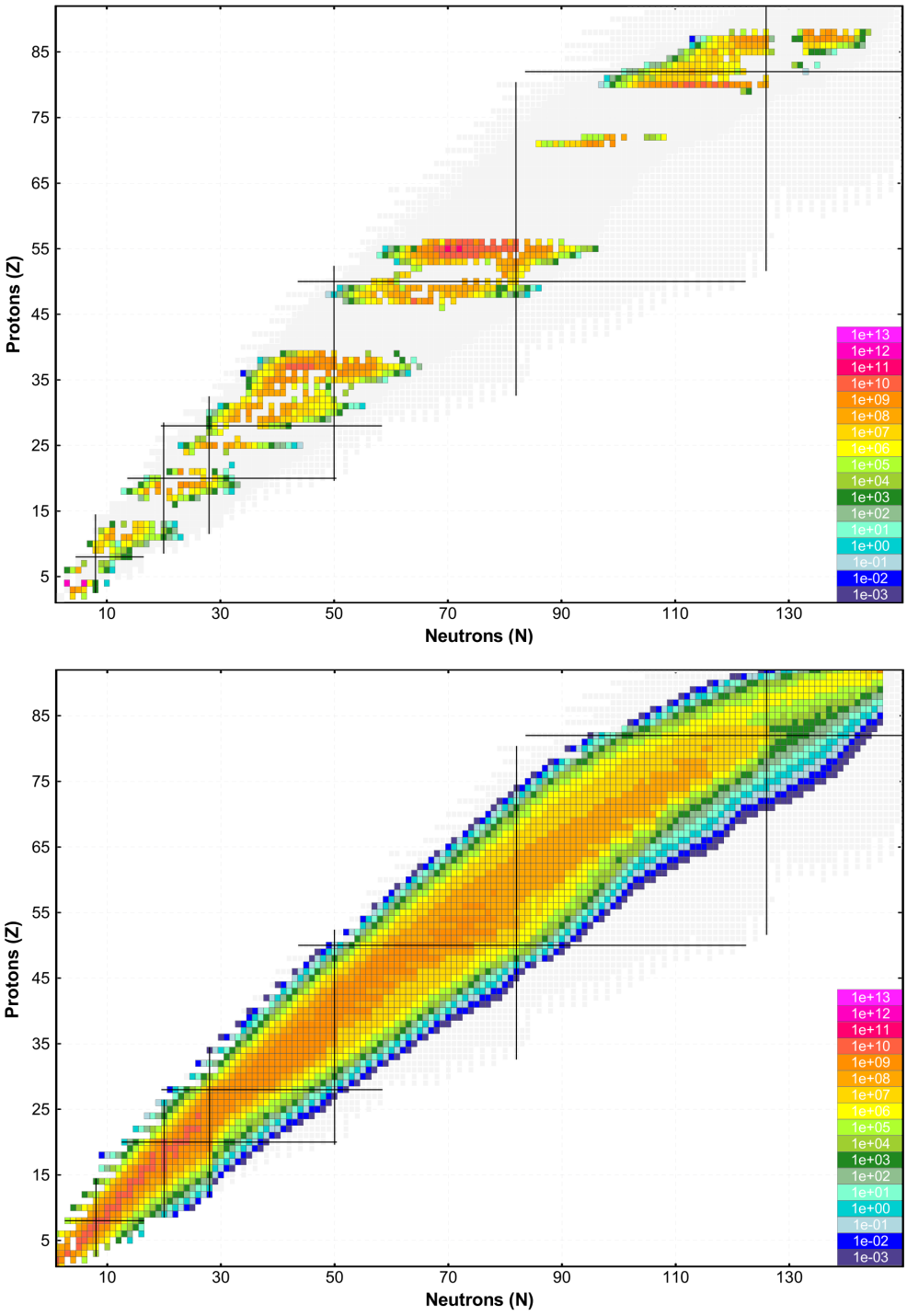

Figure 1.3: Charts of the nuclides illustrating the qualitative difference in isotope production by the ISOL and the in-flight methods [Reiter, 2015]. The isotope production yields are plotted in the color code described at the bottom right of each figure. Top part shows production yields measured at ISOLDE facility [ISOLDE, 2015]; bottom part – simulated production yields for the Super-FRS at FAIR [Pietri, 2015]. Presented yields of two production methods are not to be compared quantitatively between each other.

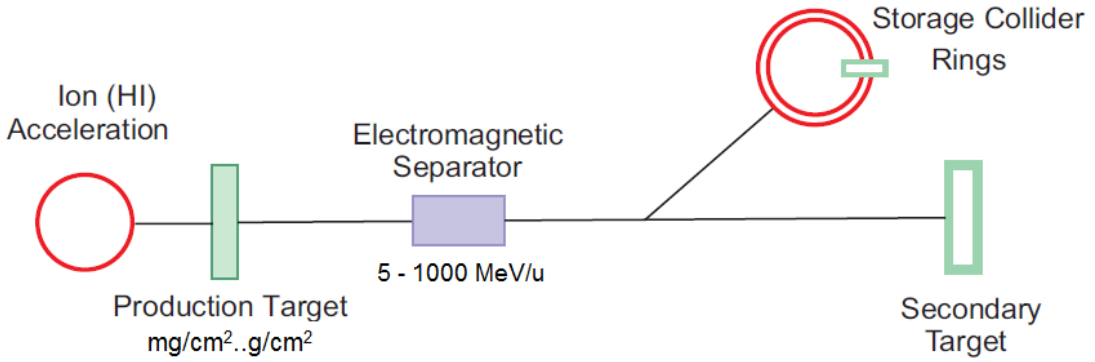

Figure 1.4: Schematic figure of the in-flight method [Geissel et al., 1995].

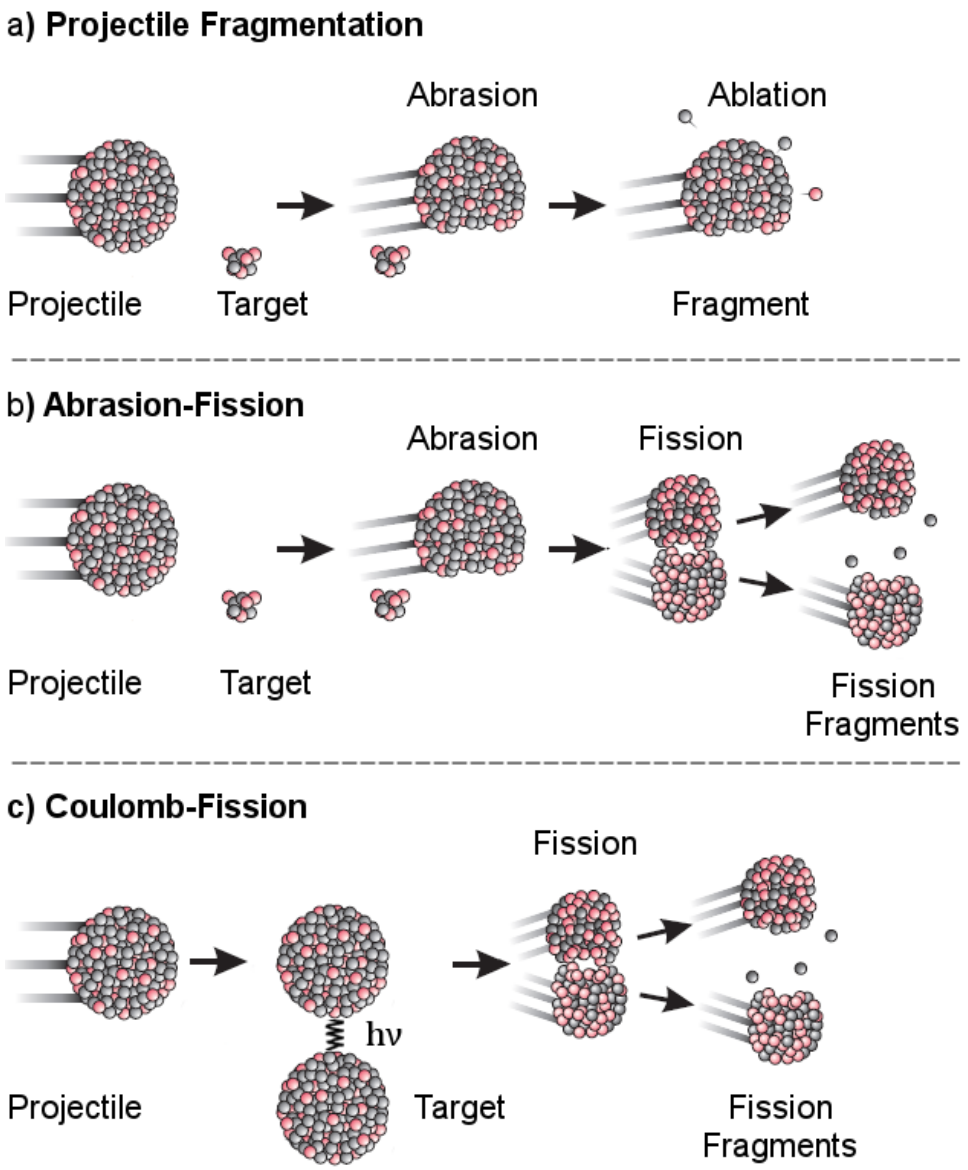

Figure 1.5: Schematic figure of: a) fragmentation reaction; b) abrasion-fission reaction; c) Coulomb-fission reaction.

can be also triggered by the excitation due to the exchange of virtual photon with the target nucleus, typically with a high atomic number Z (Fig. 1.5c). This reaction is called the Coulomb fission. Produced nuclei are stripped of their electrons in a thin metal foil, separated in-flight in a magnetic separator, and delivered to high-energy experiments, such as storage rings. The produced secondary beam can be also used for the production of even more exotic nuclei in a secondary target.

In-flight separation of relativistic ions is done with magnetic fields and an element-specific energy loss in matter. In the first stage of a magnetic separator, the ions are spatially separated by their magnetic rigidity $B\rho$, which is proportional to the mass-to-charge ratio, or A/Z in case of fully ionized nuclei. The range of A/Z corresponding to the ions of interest is selected by slits at the dispersive intermediate focal plane. The ions pass through a thick wedge-shaped aluminum degrader, where they lose energy ΔE proportional to their Z^2. Afterwards, they fly through another $B\rho$ separation stage. The combination of these steps results in an isotopically separated beam at the final focal plane of the separator. This method of the in-flight separation is called $B\rho - \Delta E - B\rho$ method [Geissel et al., 1992a]. An example of it being employed at the fragment separator (FRS) at GSI is shown in Fig. 1.6 [Geissel et al., 2013]. Simulation of production and in-flight separation of the ^{78}Ni isotope is demonstrated. The nuclei are produced in the projectile reaction of ^{86}Kr at the energy of 500 MeV/u. After the first magnetic separation stage, the ion species with $A/Z \sim 78/28$ are selected. Then, they pass through the energy degrader and the second separation stage. At the final focal plane, the ions are isotopically separated and the ^{78}Ni isotope is selected.

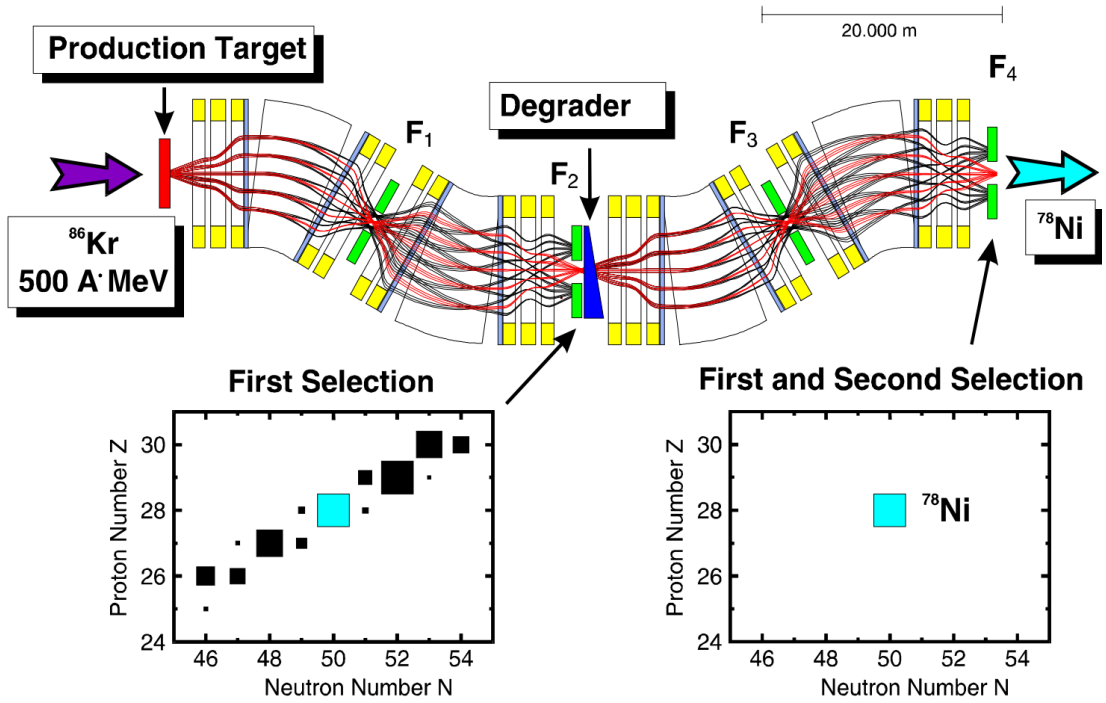

Figure 1.6: Simulation of the ^{78}Ni isotope production and separation in the FRS [Geissel et al., 1992a]. Separation is performed by $B\rho - \Delta E - B\rho$ method. Calculated envelopes are shown. Secondary beam compositions at the intermediate and final focal planes are shown in the two insets.

Compared to the ISOL method, the in-flight method is chemistry-independent and fast. The exotic nuclei of all chemical elements can be produced and delivered to the experiments in less than a microsecond, which gives access to a very broad range of nuclides with half-lives down to $\sim$ 100 ns. Simulated production yields for the Super-FRS [Geissel et al., 2003] at FAIR are shown in the bottom part of Fig. 1.3 [Reiter, 2015]. For the beams produced at relativistic energies, good particle identification is possible with a sensitivity to single ions, which makes this method a very powerful technique for the search for new isotopes [Thoennessen, 2013]. Another feature of the in-flight method is that the ions produced at relativistic energies have a broad angular and momenta spread. Therefore, for some of the high-accuracy experiments, a cooling of ions is required.

1.2.3 Hybrid method

In order to enable low-energy experiments with ions produced at relativistic energies, a hybrid method was introduced. A schematic representation of this method is shown in Fig. 1.7. In-flight produced and separated ions are slowed down and thermalized in a gas-filled stopping cell [Wada, 2013], extracted, reaccelerated to energies of eV to keV, and delivered to high-accuracy low-energy experiments. This combination of experimental techniques provides the advantages of both the ISOL and the in-flight methods. The stopping cell can provide fast (down to few ms) and efficient stopping and extraction of ions, thus making also very short-lived exotic nuclei accessible. An example of the hybrid system is the FRS Ion Catcher experiment [Plaß et al., 2013a] at GSI, which is described in detail in Section 2.2.

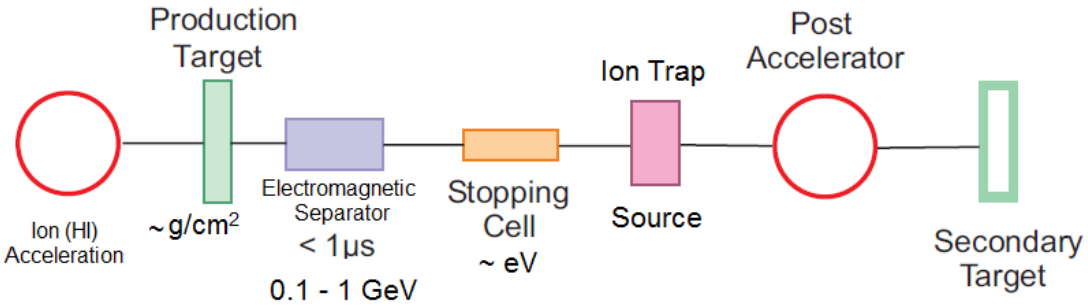

Figure 1.7: Schematic figure of the hybrid method [Geissel et al., 1995].

1.3 Ion motion in fields and matter

At a hybrid facility, ion beams are produced at relativistic energies and then converted to energies of a few eV to keV. The ions lose most of their energy in specially-shaped degraders installed in the beamline. When flying through matter, ions experience atomic and nuclear interactions, which lead to the energy loss, but also to a broadening of the energy distribution (energy straggling), change of the direction of ion flight and even of their charge state [Geissel et al., 2002]. Once the ions are thermalized in a gas-filled stopping cell, they are extracted out of the stopping gas and directed to experimental stations. Understanding of all these processes is of crucial importance for the experiments. Corresponding physical aspects are addressed in the following subsections.

1.3.1 Slowing down and stopping of relativistic ion beams

Energy loss and energy loss straggling

According to the classical description by Nils Bohr [Bohr, 1913], ions lose energy when passing through matter in multiple inelastic collisions with atomic electrons. The mean energy loss $\langle \Delta E \rangle$ of a projectile ion passing through matter with a thickness of Δx and an atomic density of n is given by

$$\langle \Delta E \rangle = n \Delta x \sum_i \sigma_i T_i, \tag{1.1}$$

where T_i is the kinetic energy loss in the i'th collision with the collision cross section of σ_i. Using the classical approach, Bohr derived the following formula for the energy loss dE per distance dx, that the ion passes in matter [Bohr, 1913]:

$$-\frac{dE}{dx} = \frac{4\pi Z_1^2 Z_2 n e^4}{m_e v^2} \cdot \ln\left(\frac{1.123\ m_e v^3}{Z_1 e^2 \nu}\right), \tag{1.2}$$

where e is the elementary charge, $Z_1 e$ and $Z_2 e$ are the charges of the projectile ion and the target nucleus, correspondingly, v is the velocity of the projectile ion, m_e is the mass of the electron, and ν is the mean electron frequency. The quantity dE/dx is also called the stopping power.

Bohr's classical formula contains all the essential features of electronic collision loss by charged particles, but it does not take into account quantum effects. Hans Bethe approached the same problem with quantum mechanical perturbation theory [Bethe, 1932]. He used the first-order Born approximation and obtained the following expression for relativistic ions:

$$-\frac{dE}{dx} = \frac{4\pi Z_1^2 Z_2 n e^4}{m_e c^2 \beta^2} \cdot L \tag{1.3}$$

with the so-called stopping number L, which is, according to Bethe, given by:

$$L_{\text{Bethe}} = \ln\left(\frac{2m_e c^2\beta^2\gamma^2}{I}\right) - \beta^2, \tag{1.4}$$

where I is the mean ionization potential of the target atoms, c is the speed of light, γ is the Lorentz factor, and $\beta = v/c$.

With further development of the theory, additional corrections were implemented to the stopping number expression in order to better describe experimental data:

- **The density effect ($-\delta/2$):** originates from the fact that the electric field of the projectile ion polarizes the target atoms, which results in a screening effect for the electrons located further away from the ion path. Because of this, these distant electrons contribute less to the total energy loss. The density effect was first calculated by Enrico Fermi [Fermi, 1940] and then extended by Sternheimer and Peierls [Sternheimer and Peierls, 1971].

- **The Bloch correction (ΔL_{Bloch}):** addresses the differences between classical and quantum mechanical treatments, especially for the cases of small impact parameters [Bloch, 1933].

- **The Mott correction (ΔL_{Mott}):** corrects the stopping cross sections for exact solutions of the Dirac equation for the atomic electrons of target material [Mott, 1929]. It has the highest impact at high Z_1 and β of the projectile ion.

- **Other corrections (Barcas effect, shell correction, etc.)**, which are not significant for the energy loss of heavy relativistic ions in matter.

First experimental studies of stopping powers for relativistic heavy ions with the FRS were conducted in [Scheidenberger et al., 1994]. Later, Lindhard and Sørenson [Lindhard et al., 1996] calculated the stopping cross sections using the exact solutions of the Dirac equation and taking into account the charge distribution of the projectile ion, not treating it as a point-like charge. Their calculations (ΔL_{LS}) included the Bloch (ΔL_{Bloch}) and Mott (ΔL_{Mott}) corrections and demonstrated good agreement with experimental results [Scheidenberger et al., 1996]. Therefore, the formula for the stopping power of heavy relativistic ions in matter can be rewritten as

$$-\frac{dE}{dx} = \frac{4\pi Z_1^2 Z_2 n e^4}{m_e c^2 \beta^2} \cdot \left(L_{\text{Bethe}} + \Delta L_{\text{LS}} - \frac{\delta}{2}\right). \tag{1.5}$$

Besides the general energy reduction of the ion beam passing through matter, the width of the ions energy distribution is broadened. This broadening is called the energy loss straggling Ω_E and it is calculated as the standard deviation of the energy loss:

$$\Omega_E^2 = \left\langle (\Delta E - \langle \Delta E \rangle)^2 \right\rangle. \tag{1.6}$$

The energy straggling occurs due to the statistical nature of the collisions that the ions undergo when passing through matter. The higher the initial energy of the projectile ions and the longer the path in matter they have traveled, the larger is the collisional energy loss straggling. Another effect, which can strongly contribute to the energy straggling is the charge exchange. The charge change of the projectile ion can occur as the result of an electron capture or an ionization process and it strongly affects the stopping power. It has been shown that the charge-exchange energy straggling can significantly increase the width of the energy distribution of the ions [Weick et al., 2000].

Range and range straggling

As ions lose their energy when passing through matter, there will be a certain moment when they will be stopped. The amount of matter required to stop the ion beam is called the stopping range. The range distribution of ions is of special interest for experiments with gas-filled stopping cells used for the beam thermalization. Analytically, the mean range of heavy ions in matter R can be calculated within the continuous-slowing-down model [Ziegler and Biersack, 1985] as the definite integral from the initial energy of the projectile ions E_0 to the thermal energy of the stopping medium $E_{\min}$:

$$R = \int_{E_{\min}}^{E_0} \left(\frac{dE}{dx}\right)^{-1} dE. \tag{1.7}$$

Deviations in momenta of the projectile ions and the energy loss straggling result in the broadening of the range distribution or the so-called range straggling. The range straggling Ω_R can be described by the following analytical expression [Lindhard, 1964]:

$$\Omega_R^2 = \int_{E_{\min}}^{E_0} \frac{\frac{d\Omega_E^2}{dx}}{\left(\frac{dE}{dx}\right)^3} dE. \tag{1.8}$$

An example of the range and the range straggling is shown in Fig. 1.8 [Reiter, 2015] for an ion beam of ^{132}Sn with an initial kinetic energy of 500 MeV/u. The black curve represents the fraction of ions left in the ion beam after passing a certain range in helium gas. Blue and red curves reflect the range straggling for a monoenergetic beam and for a beam with a relative momentum spread of $\delta_{p0} = 0.1$ %, respectively. The mean of the range distributions corresponds to the point where half of the projectile ions are stopped in the helium gas. Calculations of the range and the range straggling were done with the ATIMA [Weick et al., 2018] software. As can be seen from the plot, even the presence of a very small momentum spread results in a significant increase in the range straggling. In experiments at hybrid facilities, the ions pass most of their range in aluminum degraders, and only the final part, determined by the range straggling, in the buffer gas of the stopping cell. In order to thermalize all projectile ions, the thickness of the stopping volume of the gas cell must be larger than the range straggling value. A technical advantage of the use of monoenergetic beams for such experiments is evident.

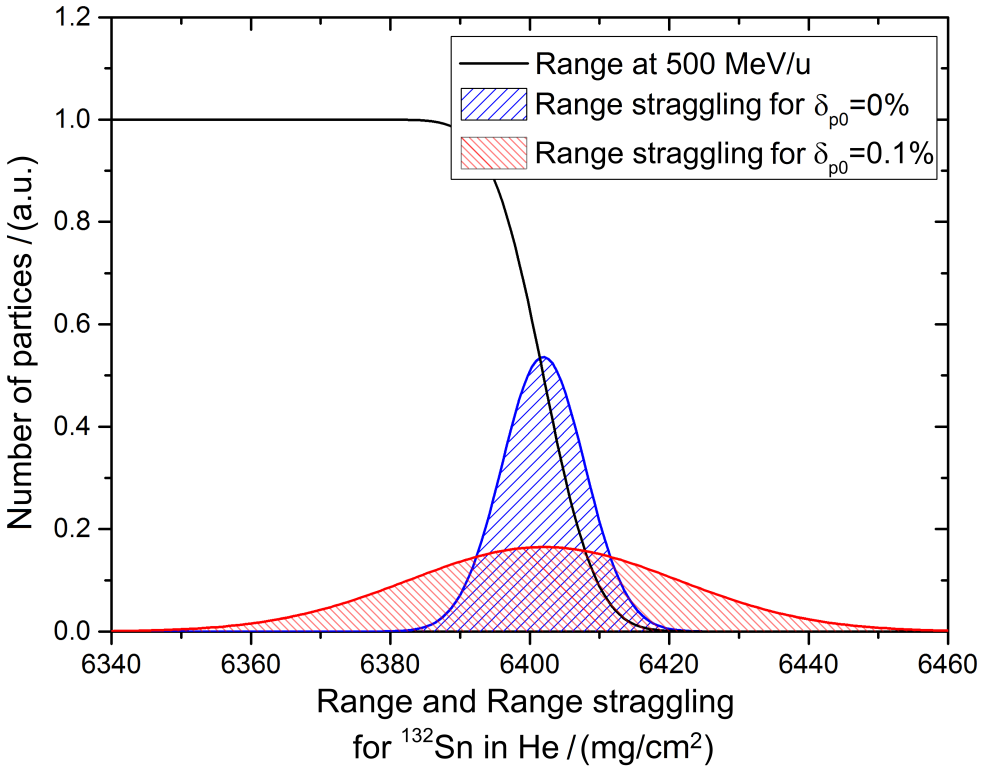

Figure 1.8: Calculated range and range straggling of the ^{132}Sn ions with an initial kinetic energy of 500 MeV/u in helium gas [Reiter, 2015]. Calculations were done with the ATIMA [Weick et al., 2018] software. Black curve represents the number of ions left in the beam at certain helium range; blue and red curves – the range distributions for the ion beams with the momentum spread δ_{p0} of 0 % and 0.1 % respectively.

As it has already been mentioned, slowing down of the projectile ions from a high initial kinetic energy will result in a broad energy and, therefore, also broad range distributions. At the existing GSI and future FAIR facilities, exotic nuclei are produced at relativistic energies of 1-1.5 GeV/u. A calculation of the amount of helium gas required to stop the ion beams produced at these energies was done in ATIMA [Weick et al., 2018]. Results of the calculations for the ^{132}Sn ions are plotted in Fig. 1.9 [Winfield et al., 2013]. The left vertical axis indicates the range of ions in units of helium areal density, whereas the right vertical axis gives the range value in meters of a stopping helium gas at 100 mbar and 300 K – the typical operating conditions for conventional gas-filled stopping cells. In black color, the mean range is plotted. Red and blue curves represent the range straggling for an ion beam with the relative momentum spread $\delta_{p0} = 2.5$ % and for a monoenergetic beam, respectively. The results show that for the ion beams produced at 1 GeV/u, the mean range of ions exceeds 10 km of helium gas. Even if the biggest part of the range can be substituted by the equivalent thickness of a degrader, the stopping volume of the gas cell has to cover a reasonable part of the range straggling. It can be seen that only the range straggling of the monoenergetic beam allows the use of a stopping cell with a technically reasonable length for the efficient thermalization of ions. Nevertheless, even for the monoenergetic beam, the areal density of the stopping gas of more than 30 mg/cm^2

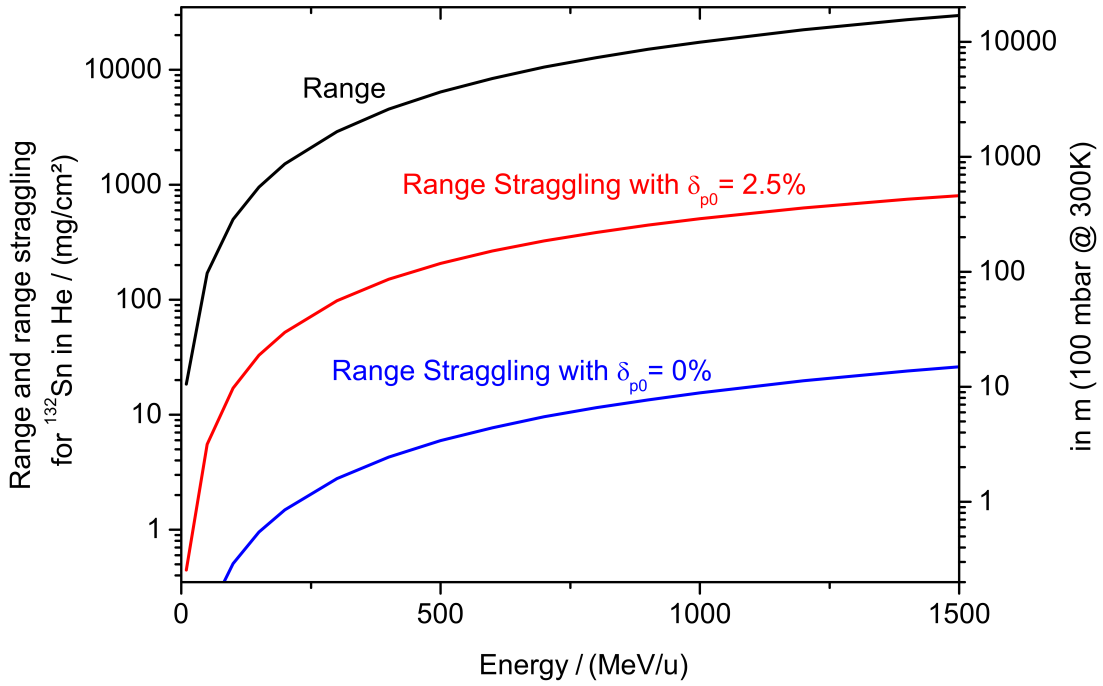

Figure 1.9: Range and range straggling of the ^{132}Sn ions in helium gas calculated with the ATIMA [Weick et al., 2018] software for different initial kinetic energies of the beam [Winfield et al., 2013]. Black line represents the mean range of ions; red and blue lines – the range straggling components for the ion beams with the momentum spread δ_{p0} of 2.5 % and 0 % respectively. Values of range straggling are given as standard deviation.

is required in order to cover the part of the range distribution corresponding to two standard deviations.

1.3.2 Ion motion in gas and electric fields

Once ions are thermalized in the stopping volume of the gas-filled cell, they continue to move in a viscous gas medium and applied electric field. Pressures of the stopping gas reach hundreds of millibar, therefore, the ions collide mostly with neutral atoms of the gas and not with each other. The number of injected ions is very small compared to the density of the stopping gas, so the Coulomb interaction between them can be also neglected. The ion motion is then described in terms of collisions with the gas atoms, diffusion, and the presence of an external electric field $\vec{E}$. For any charged particles, the corresponding equation of fluid motion [Batchelor, 1967] can be written as

$$\begin{aligned} mn\frac{d\vec{v}}{dt} &= mn\left(\frac{\delta\vec{v}}{\delta t} + (\vec{v}\cdot\nabla)\,\vec{v}\right) \\ &= \pm qn\vec{E} - \nabla p - mnf\vec{v}, \end{aligned} \tag{1.9}$$

where m, $\pm q$, n, and $\vec{v}$ are respectively the mass, the charge, the density, and the velocity of the charged particles, ∇p is the pressure gradient, and f is the collision frequency.

If the motion of the fluid is significantly slower than the time between particles collisions, the steady state can be assumed. The left part of Eq. (1.9) is then equal to zero and the equation can be rewritten as

$$0 = \pm qn\vec{E} - \nabla p - mnf\vec{v}. \tag{1.10}$$

This equation solved with respect to the velocity $\vec{v}$ gives

$$\vec{v} = \frac{1}{mnf}\left(\pm qn\vec{E} - \nabla p\right). \tag{1.11}$$

For the isothermal conditions, Eq. (1.11) can be modified to

$$\begin{aligned}\vec{v} &= \frac{1}{mnf}\left(\pm qn\vec{E} - k_{\mathrm{B}}T\nabla n\right) \\ &= \pm\frac{q}{mf}\vec{E} - \frac{k_{\mathrm{B}}T}{mf}\frac{\nabla n}{n},\end{aligned} \tag{1.12}$$

where k_{B} is the Boltzmann constant and T is the temperature of the gas medium. This expression shows that the ion motion is influenced by the electric field and the gas density gradient. The coefficients in front of $\vec{E}$ and $\nabla n/n$ are called the ion mobility K and the diffusion coefficient D:

$$K = \frac{q}{mf} \quad [\mathrm{cm}^2/(\mathrm{V}\cdot\mathrm{s})], \qquad D = \frac{k_{\mathrm{B}}T}{mf} \quad [\mathrm{cm}^2/\mathrm{s}]. \tag{1.13}$$

These coefficients are connected by the Nernst-Einstein relation:

$$K = \frac{qD}{k_{\mathrm{B}}T}. \tag{1.14}$$

If there is no electric field applied, Eq. (1.12) can be transformed into the Fick's law of diffusion [Fick, 1855]. In the case of a homogeneous gas medium, the ions will have a drift velocity defined by the electric field $\vec{E}$.

The ion mobility K is inversely proportional to the gas density. Therefore, usually the value of the reduced mobility K_0 under the normal conditions ($p_0 = 1.013$ bar and $T_0 = 273.15$ K) is reported and used:

$$K = K_0\frac{T}{T_0}\frac{p_0}{p}. \tag{1.15}$$

1.3.3 Ion motion at RF carpet

For the extraction of ions out of the stopping cell, different methods are used. In some stopping cells, ions are extracted with a gas flow. An example of such a device

is employed in the IGISOL technique [Dendooven, 1997]. Other stopping cells use the combination of the gas flow and electric fields. Applications of the radio-frequency electric fields in the viscous medium were first studied in [Masuda and Fujibayashi, 1970] and were later adopted for the fast ion extraction out of gas-filled stopping cells [Wada, 2013]. In this work, the RF carpet was used to repel the ions, preventing them from hitting the electrodes and to guide them towards the extraction nozzle. The RF carpet has a number of concentric electrode rings on the flat printed circuit board, to which a radio-frequency signal of a few megahertz is applied. The neighboring rings have the 180° phase-shifted RF voltage, which results in an inhomogeneous RF field that repels the ions. More details on the technical design of the RF carpet are given in Subsection 2.2.1.

In order to analytically describe the ion motion at the RF carpet, the concept of a pseudopotential [Dehmelt, 1967] is used. In this concept, the RF electric field is averaged over a cycle in order to estimate the effective electric field that affects the ions. The effective electric field E_{eff} of an RF structure calculated from the pseudopotential approach by [Tolmachev et al., 1997, Wada et al., 2003] can be written as

$$E_{\text{eff}} = \frac{qV_{\text{RF}}^2}{2mr_0^3} \cdot \left(\frac{r}{r_0}\right) \cdot \frac{\tau^2}{1+\Omega^2\tau^2}, \tag{1.16}$$

where m and q are the mass and the charge of the ions, V_{RF} and $\Omega/2\pi$ are the amplitude and the frequency of the applied RF voltage, and r_0 is the half of the electrode pitch size (the distance between centers of neighboring electrodes). The parameter τ is called the velocity relaxation time. It characterizes the time that ions need to lose the velocity they gained by the electric field in the collisions with atoms of the stopping gas. It is the reciprocal of the collision frequency f and can be calculated from Eq. (1.13):

$$\tau = \frac{1}{f} = K\frac{m}{q}. \tag{1.17}$$

In the high-pressure environment of the stopping cell, the collision frequency f is very high, which results in $\Omega^2\tau^2 \ll 1$. In this case, Eq. (1.16) can be modified to

$$\begin{aligned} E_{\text{eff}} &= \frac{qV_{\text{RF}}^2}{2mr_0^3} \cdot \left(\frac{r}{r_0}\right) \tau^2 \\ &= \frac{V_{\text{RF}}^2}{2r_0^3} \cdot \left(\frac{r}{r_0}\right) K^2 \frac{m}{q}. \end{aligned} \tag{1.18}$$

Substitution of Eq. (1.15) gives

$$E_{\text{eff}} = \frac{1}{2}V_{\text{RF}}^2 \, \frac{1}{r_0^3} \left(\frac{r}{r_0}\right) \left(K_0 \frac{T}{T_0}\frac{p_0}{p}\right)^2 \frac{m}{q}. \tag{1.19}$$

Equation (1.19) describes the effective repelling field of the RF carpet. It also demonstrates a complex interplay of many operating parameters, which have to be set up correctly for efficient extraction of ions out of the stopping cell.

1.3.4 Ion motion in RFQ

After ions are extracted out of the gas-filled stopping cell, they are transported to downstream experiments. For the transport of the low-energy ions, radio-frequency quadrupoles (RFQs) can be used. A quadrupole consists of four round or hyperbolically shaped parallel rods, to which a radio-frequency voltage is applied. Opposite rods of the RFQ are electrically connected and supplied with an RF voltage, which is 180 degrees phase-shifted compared to the other pair of rods. The RF field confines ions radially inside of the RFQ.

According to [Dawson, 1976], the electric potential Φ inside of the RFQ can be expressed as

$$\Phi = \Phi_0 \frac{x^2 - y^2}{r_0^2}, \tag{1.20}$$

where r_0 is the half of the distance between opposite electrodes and Φ_0 is the potential difference between the two pairs of rods. In the case of an applied constant quadrupolar voltage U and a radio-frequency quadrupolar voltage V with the angular frequency Ω, the expression for Φ_0 can be calculated as

$$\Phi_0 = U + V \cos \Omega t. \tag{1.21}$$

Therefore, the equations of motion for the ions with the mass m and the charge q inside of the RFQ are

$$\begin{aligned} m\frac{d^2x}{dt^2} &= -\frac{2q}{r_0^2}\left(U + V\cos\Omega t\right)x, \\ m\frac{d^2y}{dt^2} &= \frac{2q}{r_0^2}\left(U + V\cos\Omega t\right)y. \end{aligned} \tag{1.22}$$

By expressing time in terms of the parameter $\xi = \Omega t/2$, the equations of motion can be modified to

$$\begin{aligned} \frac{d^2x}{d\xi^2} &= -\frac{8q}{m\Omega^2 r_0^2}\left(U + V\cos 2\xi\right)x, \\ \frac{d^2y}{d\xi^2} &= \frac{8q}{m\Omega^2 r_0^2}\left(U + V\cos 2\xi\right)y. \end{aligned} \tag{1.23}$$

Here, the Mathieu stability parameters $a_{x,y}$ and $q_{x,y}$ can be introduced:

$$a_x = -a_y = \frac{8qU}{m\Omega^2 r_0^2}, \tag{1.24}$$

$$q_x = -q_y = \frac{4qV}{m\Omega^2 r_0^2}. \tag{1.25}$$

The equations of motion can be then rewritten in a general form:

$$\frac{d^2u}{d\xi^2} + (a_u - 2q_u \cos 2\xi)\, u = 0, \tag{1.26}$$

where u is either x or y.

This equation describes the ion motion inside of the RFQ in terms of stability. Only for the combinations of a_u and q_u parameters, which result in real (not complex) solutions of the equation, the ion motion in the RFQ is stable. The ranges of the Mathieu parameters corresponding to the stable ion motion are shown in the top panel of Fig. 1.10. Filled areas represent the stable motion of ions in either x- or y-direction. The intersections of these areas are called the stability regions. Only if both a_u and q_u parameters values lie within the stability region, the ion motion in the RFQ is stable.

For practical reasons, most often RFQs are operated in the first region of stability closest to the point of $q_u = a_u = 0$. This stability region is shown in detail in the bottom panel of Fig. 1.10. For fixed operating parameters of the RFQ (r_0, V, Ω, U), the Mathieu parameters depend only on the mass m and the charge q of the ion. From the Eqs. (1.24) and (1.25), it can be seen that all masses lie on the line with a slope $a_u/q_u = 2U/V$. This line is called the mass-scan line. Only the ions with masses lying on this line inside of the stability region are transported through the RFQ, the rest become unstable and are lost on the RFQ rods.

If the RFQ is operated without a constant quadrupolar voltage U ($a_u = 0$), it works as an ion guide transmitting the ions of a broad range of masses. Only the ions with a Mathieu parameter q_u higher than 0.908 are not transmitted. This threshold is called the low-mass cut-off. If a constant quadrupolar voltage U is applied ($a_u \neq 0$), the RFQ works in a mass-filtering mode [Paul and Steinwedel, 1953]. An example is shown in the bottom panel of Fig. 1.10. The mass scan line nearly crosses the apex of the stability region ($a_u \sim 0.237$, $q_u \sim 0.706$). Only the masses in a very narrow mass window around the mass m_2 are transported through the RFQ mass filter and all the higher masses (e.g. m_1) and the lower masses (e.g. m_3) are filtered out.

In order to transport the ions in a longitudinal direction, different methods are used. An additional z-component of the electric field can be created: a) by segmenting the RFQ rods and applying different DC potentials to the segments [Javahery and Thomson, 1997, Dodonov et al., 1997]; b) by introducing additional DC electrodes mounted in between the RFQ rods and tilted in longitudinal direction, the solution called LINAC RFQ rods [Loboda et al., 2000]; c) by building the RFQ rods out of resistive material, so the DC gradient can be applied along the electrodes [Takamine et al., 2007, Simon, 2008].

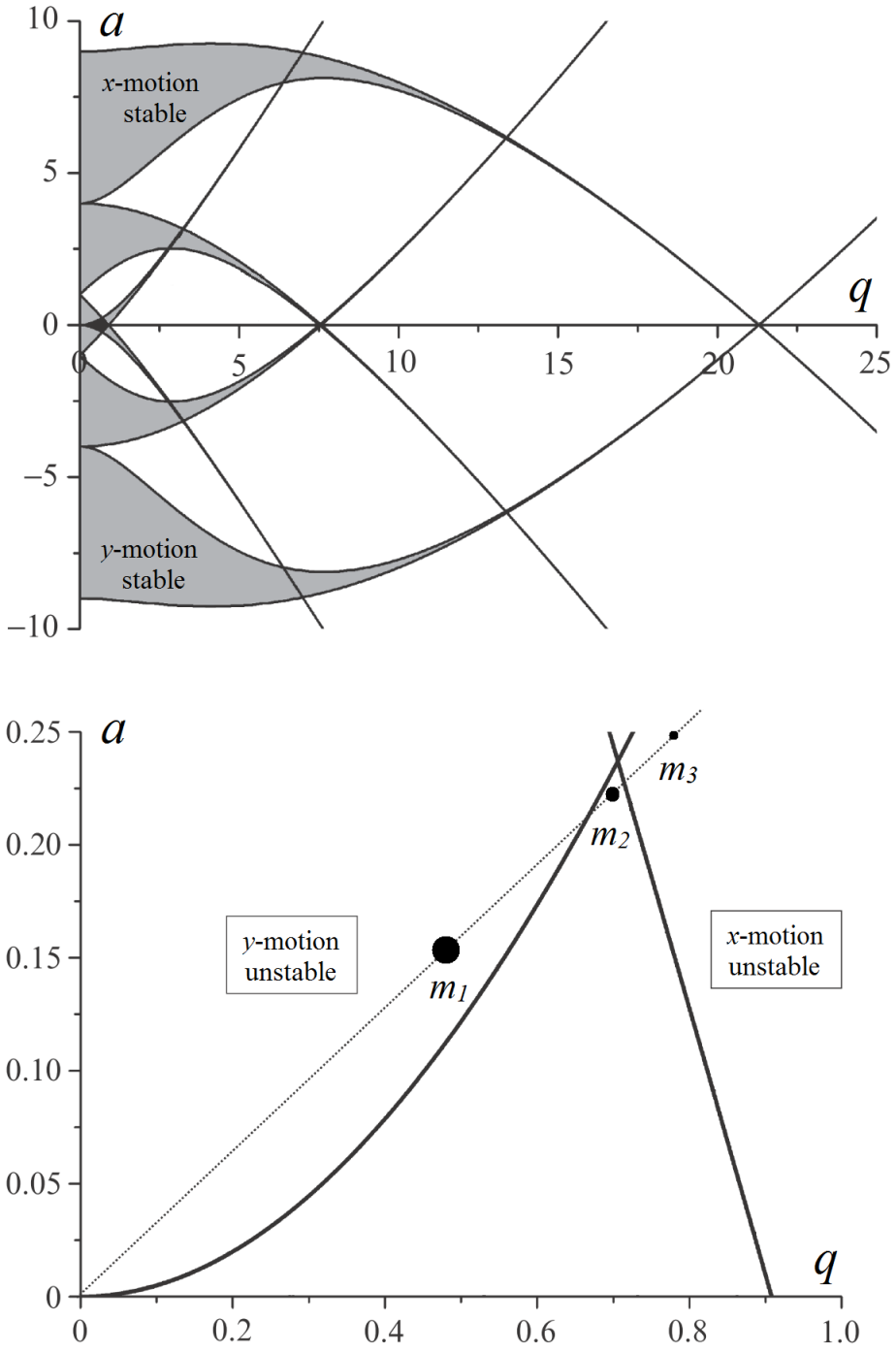

Figure 1.10: Top panel: stability diagram of a radio-frequency quadrupole [Yavor, 2009]. Filled areas correspond to the Mathieu parameters a_u and q_u, which allow the stable ion motion in x- and y-direction. The ions are transmitted by the RFQ if a_u and q_u values are in the intersections of these areas. Bottom panel: first stability region of the stability diagram. Only the ions with masses lying on the mass scan line inside of the stability region (m_2) are transported through the RFQ, whereas the higher (m_1) and the lower (m_3) masses are filtered out.

1.4 Experimental techniques for measurements of half-lives and branching ratios

Half-lives are characteristic properties of nuclei. They are an essential input to the astrophysical nucleosynthesis models required for the understanding of the origin and the abundance of chemical elements beyond iron [Iliadis, 2015]. The half-lives of exotic nuclei lying far away from the valley of stability are of the most interest. Exotic nuclei undergo different types of radioactive decay in order to obtain a more stable configuration. Three main decay types are α-, β-, and γ-decays. In addition, the nuclei can undergo single and multiple nucleon emission (e.g. p- and $2p$-decays), β-delayed nucleon emission (e.g. βn- and βp-decays) and spontaneous fission [Pfützner et al., 2012]. Some of the unstable nuclides have a probability to undergo not just one type of decay, but several. The relative probabilities for the different types of decay are called the decay branching ratios and they reflect the nuclear structure features of the mother nuclide. Branching ratios can significantly affect the astrophysical nucleosynthesis processes and have to be included in the models' calculations.

A broad variety of experimental techniques can be used for simultaneous measurements of half-lives and branching ratios. They all can be divided into three main groups:

1. **Implantation** — the most widely used method. This method is based on the most commonly used technique, where the mother nuclei are implanted into a position-sensitive detector and undergo decay. This decay is identified and measured by coincidental detection of emitted light particles (α, β, nucleons) and characteristic γ-lines of the daughter nuclei. Examples of measurements using the classical method for different decay types performed in different accelerator laboratories all over the world are given in [Mukha et al., 2006, Dillmann and Tarifeño-Saldivia, 2018, Nieto et al., 2009, Lorusso et al., 2012]. However, typically, the bottleneck to the application of this technique is the detection efficiency. The efficiency is decreased due to the geometrical factor (only a part of the solid angle is covered by the detectors) and due to the detection sensitivity, which for some of the emitted particles, like neutrons, can be energy-dependent and small.

2. **In-trap decay without retrapping of recoils** — the mother nuclei are stored in a trapping device confined in a small volume and undergo decay. The decay is identified and measured by the detection of emitted light particles inside [Äystö and Jokinen, 2003, Weber et al., 2013] or outside of the trap [Weissman et al., 2002, Rissanen et al., 2007, Brunner et al., 2013]. The recoiling daughter nuclei are not retrapped, though they can be measured by time-of-flight [Yee et al., 2013] or retardation [Kozlov et al., 2008] spectrometers. Half-lives can be determined by the decrease in the number of the mother nuclei with time [Wolf et al., 2016] or by the temporal behavior of the number of detected light particles.

3. **In-trap decay with retrapping of recoils** — the mother nuclei are stored in a trapping device (e.g. Penning trap or storage ring) and undergo decay. The daughter nuclei produced in the decay are retrapped and also stored in the trap. The decay is identified and measured by the decrease in the number of the mother nuclei with time and detection of the daughter nuclei [Franzke et al., 2008, Herlert et al., 2012]. The advantage of this method is its relative simplicity, as no additional light-particle detectors and coincidence spectroscopy are required. Therefore, these methods are less prone to systematic uncertainties and yield higher efficiency.

In the course of this work, the third group of methods is applied and discussed in detail. To perform the half-life and branching ratio measurements using the in-trap decay with retrapping of recoils, it is necessary to trap and store the mother nuclei, to retrap the produced daughter nuclei and to identify and count the mother and daughter nuclei after the storage time is over. The identification of ions can be performed by various techniques. For example, in [Jung et al., 1992] and [Bosch et al., 1996], the daughter nuclei were identified by the change in their magnetic rigidity $B\rho$ and deflection in the dipole stage of the experimental storage ring [Franzke, 1987] at GSI. However, the identification of ions by direct mass measurement is the most advantageous technique. In addition to half-life and branching ratios, direct mass measurements give information about the Q-value of the decay, not mentioning the masses themselves and deducible nucleon separation energies. Different technical solutions for the in-trap decay with retrapping of recoils and identification by direct mass measurement are discussed in the following subsections.

1.4.1 Traps for storage and retrapping of decay recoils

Ion traps of various types and working principles are nowadays successfully used for nuclear physics experiments [Eronen et al., 2016]. For the in-trap decay with retrapping of produced recoils, not all types of these ion traps can be utilized. In radioactive decay, a light particle is emitted from the mother nucleus. The light particle and the daughter nucleus recoil in opposite directions with the energies defined by the law of momentum conservation. In Table 1.1, the orders of magnitude of the recoil energies for different decay types are given. The recoil energy has to be compensated by the trapping device in order to recapture the daughter nuclei. A capability of recapturing the recoiling daughter nucleus, i.e. a retrapping efficiency, is one of the most crucial characteristics of the trapping device. In the following, a few examples of the devices, which were successfully used or proposed for the in-trap decay studies with retrapping of recoils, are presented.

Type of decay	Approximate recoil energy, eV
γ	10
β	10^2
p, n, βn, βp	10^4
α	10^5

Table 1.1: Orders of magnitude of the recoil energy for different decay types.

Penning trap

Penning traps [Brown and Gabrielse, 1986] are devices that use a combination of a homogeneous magnetic field and a quadrupolar electrostatic potential to trap ions. If only a magnetic field B is present, ions with a mass m and a charge q are confined in the radial direction perpendicular to the magnetic field lines and move with a cyclotron frequency ω_c:

$$\omega_c = \frac{qB}{m}. \tag{1.27}$$

The quadrupolar electrostatic potential is used to restrict the axial motion of the ions along the magnetic field lines. A schematic view of a Penning trap is shown in Fig. 1.11a. The quadrupolar electrostatic potential is created by a ring electrode located in the middle of the trap and two endcap electrodes. Typically, the electrodes have hyperbolic (as shown in Fig. 1.11a) or cylindrical shape.

The combination of homogeneous magnetic and quadrupolar electrostatic fields results in the ion motion consisting out of three components – axial motion ω_z, magnetron motion ω_-, and reduced cyclotron motion ω_+. The ion motion in the Penning trap is shown in Fig. 1.11b with all its components labeled. The frequencies of motion components can be expressed by the following formulas:

$$\omega_z = \sqrt{\frac{qU_0}{md^2}}, \tag{1.28}$$

$$\omega_\pm = \frac{\omega_c}{2} \pm \sqrt{\frac{\omega_c^2}{4} - \frac{\omega_z^2}{2}}, \tag{1.29}$$

where U_0 is the trapping potential and d is the characteristic trap dimension.

At radioactive ion beam facilities, often a system of two Penning traps is utilized for mass measurements. The first Penning trap is needed for the isobaric separation of ions of interest by buffer-gas-assisted mass-selective centering [Savard et al., 1991], whereas the second trap performs ultrahigh-accuracy mass measurements (see Subsection 1.4.2). It was also demonstrated that the gas-filled Penning trap can be used for storage of β-decaying nuclei and retrapping of their daughters [Herlert et al., 2005, Herlert et al., 2012]. However, the main focus of these experiments was to perform the mass spectrometry of the nuclides, that could not be produced by the ISOL

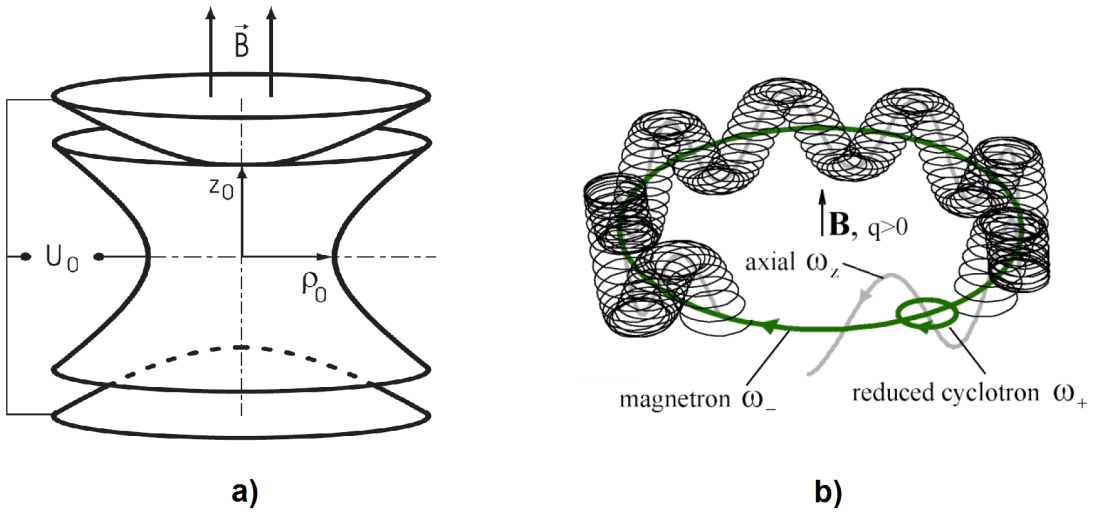

Figure 1.11: Schematic view of a) a hyperbolic Penning trap; b) the ion motion inside a Penning trap [Kozlov, 2006]. Ions are confined by a homogeneous magnetic field and a quadrupolar electrostatic field created by a ring electrode located in the middle of the trap and two endcap electrodes.

method and thus were produced by in-trap decays. The half-life of the mother isotope was measured only by the corresponding decrease in the number of trapped mother nuclei with storage time. The reason for this is the limited retrapping efficiency.

The recoil energy in β^+- or β^--decay is on the order of a few hundreds of electronvolts (see Table 1.1). If the daughter nucleus recoils in the radial direction in the strong magnetic field of a few Tesla, this recoil energy results in a cyclotron radius of a few millimeters. The size of most Penning traps allows accommodation of such cyclotron motion. In the environment of $1 \cdot 10^{-4}$ mbar of helium buffer gas, the fast cyclotron motion is efficiently cooled down to its thermal amplitudes. At the same time, in the axial direction, the ions are trapped by the quadrupolar electrostatic potential, which has a typical depth of about 100 V. If the daughter nucleus recoiling in the axial direction has its energy-to-charge ratio larger than the potential depth, then this nucleus is lost. In other words, for all decay types except for γ-decay, only the daughter nuclei recoiling at large angles to the magnetic field lines are retrapped. Accurate calculation of the retrapping efficiency is complicated because of the broad energy distribution of the recoils and the dependency on the recoil direction. Additional uncertainty is brought by different charge states of the daughter nuclei and by charge-exchange processes with the buffer gas atoms. It is also evident that retrapping of more energetic recoils produced by decays with larger recoil energy (e.g. α-decay, nucleon emission) would not be possible.

Storage ring

Storage rings are large and complex devices used for accumulation, storage and high-accuracy measurements of exotic nuclei. An example of the storage ring is the ex-

perimental storage ring (ESR) [Franzke, 1987] at GSI. Its schematic view is shown in Fig. 1.12. It has a circumference of 108 m and consists of two magnetic arcs with the maximum bending power of 10 Tm and two long straight sections. Dipole magnets are used for bending the ion beam, whereas quadrupole magnets are used for focusing. In the straight sections, an electron cooler [Steck et al., 1996] and particle detectors are installed. The whole storage ring is pumped down to an ultra-high vacuum of $10^{-11} - 10^{-12}$ mbar in order to preserve the charge state of the circulating ions. The ESR has a large momentum acceptance of $\Delta p/p \sim \pm 2$ %, which allows storing multi-component beams with different magnetic rigidities $B\rho$. With the maximum magnetic rigidity of 10 Tm, it is possible to store ions of chemical elements ranging from helium ($Z = 2$) to uranium ($Z = 92$) with kinetic energies of up to 560 MeV/u. At these high kinetic energies, also the heaviest fragments emerge from the production target as bare, H-, He-, and Li-like ions. This opens up perspectives for decay studies with radioactive highly-charged ions.

In the ESR, different types of nuclear decays were successfully studied. The retrapping and identification of the produced daughter nuclei have been demonstrated for internal transition, nuclear electron capture decay, and bound-state β-decay, which was discovered in the ESR [Franzke et al., 2008]. Retrapping efficiency limitations

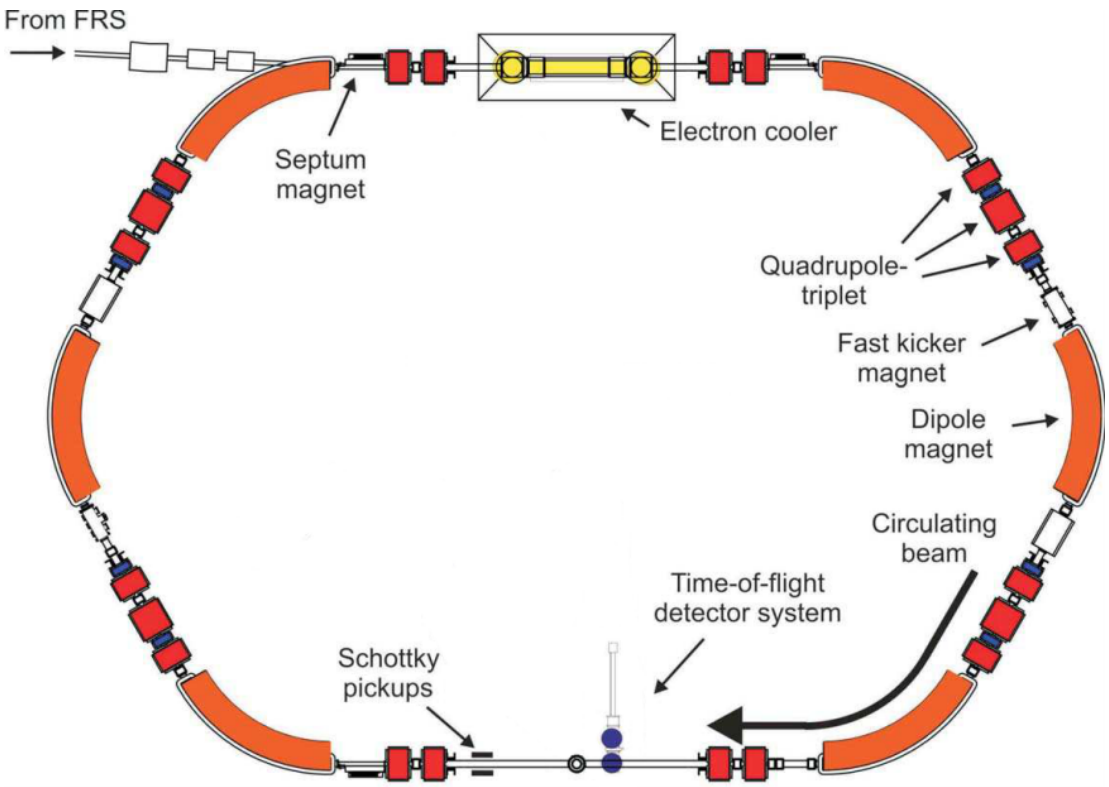

Figure 1.12: Schematic view of the experimental storage ring (ESR) [Franzke, 1987] at GSI. The main components are labeled. Mass measurements of circulating ions are performed with Schottky noise pickups (Schottky mass spectrometry) or with a time-of-flight detector (isochronous mass spectrometry).

of the storage ring originate not only from the recoil energies, but also from its magnetic rigidity $B\rho$ and momentum acceptance. In some nuclear decays, the mass-to-charge ratio m/q of the stored ions can change significantly, which results in the kick-off of the produced ion in the next dispersive section. This was used for the identification of daughter nuclei with a position-sensitive detector placed in a movable socket behind a dipole magnet [Jung et al., 1992, Bosch et al., 1996]. A few experiments were proposed to study α-decays [Patyk et al., 2008, Musumarra et al., 2009, Nociforo et al., 2012] and beta-delayed neutron emission [Evdokimov et al., 2012] in the storage ring. However, detailed systematic investigations on retrapping efficiencies for these cases still have to be conducted.

Gas-filled stopping cell

A novel approach for storage and retrapping of decay recoils, which is pursued in the context of this thesis, is to utilize a gas-filled stopping cell [Wada, 2013]. The idea is to retrap ions not by electric or magnetic fields but by dense buffer gas.

This technique can be implemented in the following way. The mother nuclei are injected into the cell and thermalized in collisions with the buffer gas atoms. They undergo decay and produce daughter nuclei that are also thermalized in the buffer gas. α-decay recoils can be stopped within ~ 50 μg/cm^2 of gas. For conventional stopping cells filled with about 100 mbar of helium at room temperature, this areal density transforms into a few centimeters of stopping range. Therefore, the retrapping of daughter nuclei produced in the decays presented in Table 1.1 with full retrapping efficiency is technically feasible. A successful example was demonstrated in [Plaß et al., 2013a], where the nuclide ^{211}Po was produced by α-decay of the projectile fragment ^{215}Rn in the helium buffer gas during the extraction out of the stopping cell. Thermalization of fission recoils with energies of up to 1 MeV/u is more challenging and requires an order of magnitude higher areal density.

Depending on the cleanliness of the buffer gas, the nuclei can be thermalized in an ionic state or as neutral atoms. Having the isotopes of interest stopped in an ionic state allows their fast extraction out of the stopping cell after the storage. The high density of the buffer gas is also required in order to ensure a low diffusion rate of the thermalized ions. The diffusion rate limits the maximum storage time that ions can be contained in the buffer gas before they are neutralized on the walls of the stopping cell. From these requirements, it is evident that a cryogenic stopping cell [Ranjan et al., 2011, Reiter, 2015, Ranjan et al., 2015] would be an ideal device for the task. Details on the design and characteristics of the cryogenic stopping cell are given in Subsection 2.2.1.

As mentioned above, a gas-filled stopping cell can provide full retrapping efficiency and is thus a possible universal tool for all types of decays. It is also relatively simple from a technical point of view, assuming that requirements to the cleanliness of the buffer gas are met. However, one of the major disadvantages of this technique is that it is not mass-selective. The incoming sample of ions has to be purified down to

the mother nuclei of interest prior to the injection into the stopping cell for the in-trap decay study. Otherwise, the presence of other nuclides may result in a harmful background hindering an unambiguous measurement. An example of utilizing the stopping cell for in-trap decay studies was proposed in [Miyatake et al., 2018]. It was suggested to solve the problem of beam purification by using two sequential sets consisting of a stopping cell and a multiple-reflection time-of-flight mass spectrometer [Wollnik and Przewloka, 1990, Plaß et al., 2013b]. The first pair of devices would perform the preliminary purification of the ion beam provided from the production target, whereas the second pair would be used for the in-trap decay studies of the purified and reaccelerated sample of the mother nuclei.

An alternative solution to this problem has been used within the frames of this thesis [Mardor et al., 2017, Miskun et al., 2019]. The preliminary purification of the ion beam has been performed by the fragment separator [Geissel et al., 1992a]. Required level of beam purification in the FRS can be reached due to the high energies of heavy-ion primary beams (up to 1 GeV/u for ^{238}U), which are worldwide unique for the GSI accelerator facility. A novel method for the measurement of half-lives and decay branching ratios of exotic nuclei utilizing the cryogenic stopping cell for ion storage and the FRS for the beam purification is described in detail in Chapter 5.

1.4.2 Direct mass measurement techniques

Nowadays, high-accuracy direct measurements of atomic nuclei are performed mainly with Penning traps, storage rings and multiple-reflection time-of-flight mass spectrometers. The measurement techniques utilizing these devices have different ranges of their application. They differ in precision, accuracy, time and number of detected ions required for mass determination.

Penning trap

There are three different measurement techniques, which were implemented in Penning traps for accurate mass determination. This is a short overview of the Penning trap measurement techniques:

1. **Time-of-flight ICR (TOF-ICR)** — the conventional technique, with which most of the high-accuracy mass measurements of exotic nuclei with Penning traps were done [Gräff et al., 1980, König et al., 1995, Eronen et al., 2016]. It uses the ion-cyclotron resonance (ICR). By applying the quadrupolar electric RF field with the frequency equal to the cyclotron frequency of ion motion ω_c, it is possible to excite ions and to completely convert their reduced cyclotron motion into the magnetron one. When ions are ejected from the trap, their radial energy is converted into the axial energy in the gradient of the magnetic field. The time-of-flight of the ions ejected out of the trap to the detector is measured for different frequencies of the quadrupolar electric field. At the resonant frequency,

ions have the highest axial energy, which results in the shortest time of flight. From the measured resonant frequency, the mass of the ion can be calculated. A boost in accuracy of the frequency determination can be reached by using a pulsed RF signal for excitation instead of the constant one. This technique is called the Ramsey's excitation [Bollen et al., 1992]. With TOF-ICR, the mass resolving power R ($R = m/\Delta m$) of $\sim$ 1-2 $\cdot 10^6$ can be reached in a few hundreds of milliseconds measurement time. However, due to the scanning nature of the technique, it is possible to measure only one ion species at a time and at least an order of a hundred of ions is required for a precise mass measurement.

2. **Fourier transform ICR (FT-ICR)** — a technique based on the measurement of a signal on pick-up electrodes, which is induced by the ion motion in the trap [Marshall et al., 1998]. The measured signal is Fourier transformed and the frequency spectrum is obtained. FT-ICR is a standard technique in analytical mass spectrometry and is currently under development for nuclear physics measurements. As this is a non-destructive technique, the mass measurement can be performed with only one ion giving access to the exotic nuclei with extremely low production rates. However, for the measurements of single ions, this technique is limited to a very narrow-band operation due to the high noise sensitivity.

3. **Phase-imaging ICR (PI-ICR)** — a powerful technique developed recently, which allows mass measurements with 40 times higher resolving power than TOF-ICR in a factor of 25 faster measurement times [Eliseev et al., 2013, Eliseev et al., 2014]. PI-ICR is based on the measurement of the total phase of the radial motion by projecting the ion motion in the trap onto a high-resolution position-sensitive detector. From the measured phase, the cyclotron frequency can be calculated. This non-scanning technique has enormous potential for the ultrahigh-accuracy mass measurements of exotic nuclei. Disadvantages of PI-ICR are that it is a narrow-band technique not capable of measuring multiple isobars at the same time and that the ions have to be extremely well prepared before the measurement, which typically requires a few hundreds of milliseconds.

Storage ring

In storage rings, the differential dependence of the revolution frequency f of stored ions on their velocity v and mass-to-charge ratio m/q is described by the following equation:

$$\frac{\Delta f}{f} = \frac{1}{\gamma_t^2}\frac{(\Delta m/q)}{(m/q)} + \left(1 - \frac{\gamma^2}{\gamma_t^2}\right)\frac{\Delta v}{v}, \tag{1.30}$$

where Δv is the velocity spread of ions and γ is the relativistic Lorentz factor. γ_t is the so-called transition point, an ion optical characteristic of the storage ring. In order to reach a high mass resolution, the second term of Eq. (1.30) must be as small as possible. This can be reached by two different ways corresponding to two different measurement techniques:

1. **Schottky mass spectrometry (SMS)** — by using a combination of stochastic [Nolden et al., 2000] and electron [Poth, 1990] cooling, the relative velocity spread $\Delta v/v$ is reduced down to the level of $\sim 10^{-7}$. The revolution frequency of the ions is measured by the beam noise pick-up with Schottky electrodes [Geissel et al., 1992b]. The non-destructive nature of this technique allows mass measurement with only one ion of interest trapped in the storage ring. The mass resolving power of up to $7 \cdot 10^5$ can be reached [Litvinov et al., 2005]. SMS is a broadband technique and can be used with multi-component ion beams. The main disadvantage of SMS is that the cooling process takes a few seconds, which results in a corresponding half-life limitation for investigated nuclei.

2. **Isochronous mass spectrometry (IMS)** — with IMS, the storage ring is operated at the transition point ($\gamma = \gamma_t$), such that the revolution frequency of ions does not depend on their velocity spread Δv [Hausmann et al., 2000]. This helps to spare the time required for the ion cooling. The revolution time is measured by a TOF detector [Trötscher et al., 1992]. Ions pass through a thin carbon foil at each turn. Electrons created in the foil are directed by a combination of electric and magnetic fields to a channel-plate detector. One full turn in the storage ring ESR takes about 500 ns for the ions with an energy of 400 MeV/u. The mass value of the circulating ions can be obtained after a few turns meaning that the measurement times down to tens of microseconds are achievable. Therefore, measurements with very short-lived exotic nuclei can be performed.

Multiple-reflection time-of-flight mass spectrometer (MR-TOF-MS)

In recent years, MR-TOF-MS are more and more often utilized for high-accuracy mass measurements of short-lived nuclei. The working principle of time-of-flight mass spectrometry is described in [Cameron and Eggers, 1948]. Short bunches of ions are injected into a field-free drift region with the same kinetic energy E_k given by an accelerating potential U. Ions with different mass-to-charge ratios m/q fly a certain distance l in different times t. Analytically, it can be expressed in the following way:

$$t = \frac{l}{v} = l \cdot \sqrt{\frac{m}{2E_\mathrm{k}}} = l \cdot \sqrt{\frac{m}{2Uq}}, \tag{1.31}$$

where v is the ion velocity. Lighter ions have a higher velocity for the same kinetic energy and, therefore, reach a detector positioned at the energy-time focus plane faster. The mass of the ion of interest (IOI) can be determined by measuring the TOF of the IOI and of the calibration ion, for which the mass is well known.

The main limitation of the mass resolving power R of the TOF technique is the limited path length l. To overcome this limitation, the multiple-reflection TOF technique [Wollnik and Przewloka, 1990] was developed. The ion path is extended by folding the ion trajectory in a relatively small volume with multiple reflections. The part of the mass spectrometer including the drift region and mirrors or reflectors is called the analyzer.

Another important limitation to the mass resolving power is the energy and angular distributions of ions before their injection into the analyzer. The MR-TOF technique requires well-prepared bunches of ions with minimal spatial, energy and angular spreads. The differences in starting position and initial energy of ions result in the broadening of the peaks in a TOF spectrum and worsen the resolution. Solutions to this problem are elaborated injection systems, where ions are cooled and bunched.

MR-TOF-MS is a very powerful and universal technique. It is broadband and non-scanning, so the multi-component ion beams can be investigated. A mass resolving power of 10^5 is achieved routinely in most MR-TOF-MS, however, it has been demonstrated that a mass resolving power of up to 10^6 can be reached within a measurement time of 40 ms [Will, 2019]. For precise measurement of the mass value of the IOI, only ~ 10 detected ions are needed [Ayet San Andrés et al., 2019]. This technique is, therefore, well suited for the high-accuracy measurements of short-lived nuclei with low production rates.

2 Experimental setup

This chapter describes the FRS Ion Catcher (FRS-IC) experiment [Plaß et al., 2013a]. It is an example of a hybrid system (see Subsection 1.2.3) and a very powerful experimental setup for the studies of exotic nuclei. The FRS-IC is a test facility for the Low-Energy Branch (LEB) of the Super-FRS [Geissel et al., 2003, Winfield et al., 2013] at FAIR. It is installed at the final focal plane of the fragment separator [Geissel et al., 1992a] at GSI and consists of three major parts: the gas-filled cryogenic stopping cell (CSC) [Ranjan et al., 2011, Reiter, 2015, Ranjan et al., 2015], the RFQ beamline [Reiter, 2015, Hornung, 2018] and the MR-TOF-MS [Plaß et al., 2008a, Dickel, 2010, Dickel et al., 2015b]. The exotic nuclei are produced, separated in-flight, and range bunched in the FRS, slowed down in degraders, thermalized in the CSC, extracted into the RFQ beamline and transported to the MR-TOF-MS. There, high-resolution mass measurements are performed. Due to this combination of fast and efficient production, separation and measurement techniques, the FRS Ion Catcher is well suited for the measurements of very exotic and short-lived nuclei. The details of experimental setup and conditions are discussed in the following sections.

2.1 Fragment separator

The FRS is a high-resolution magnetic spectrometer/separator [Geissel et al., 1992a]. It is located in the GSI Helmholtz Center for Heavy Ion Research (Fig. 2.1). At GSI, accelerated ion beams of the elements ranging from hydrogen to uranium are used for experimental investigations in many scientific fields and applications. The ions are produced, accelerated to energies of up to $\sim$ 11.4 MeV/u in the universal linear accelerator (UNILAC) [Angert and Schmelzer, 1969], transferred to the heavy-ion synchrotron (SIS-18) [Blasche and Franczak, 1992], further accelerated to energies of up to 1-1.5 GeV/u, and injected into the FRS. In the FRS, the relativistic ion beam bombards a production target producing exotic nuclei in projectile fragmentation and fission reactions. The secondary beam is then separated in-flight and delivered to different experiments (e.g. the ESR [Franzke, 1987, Franzke et al., 2008], R^3B experiment [Aumann, 2007], the FRS Ion Catcher, etc.).

A schematic view of the FRS and the FRS Ion Catcher is shown in Fig. 2.2. The FRS consists of two magnetic separation stages. Each stage has two dipole magnets for magnetic rigidity analysis and a set of quadrupole and sextupole magnets for focusing of the beam and ion optical corrections. At the central focal plane of the FRS, a vari-

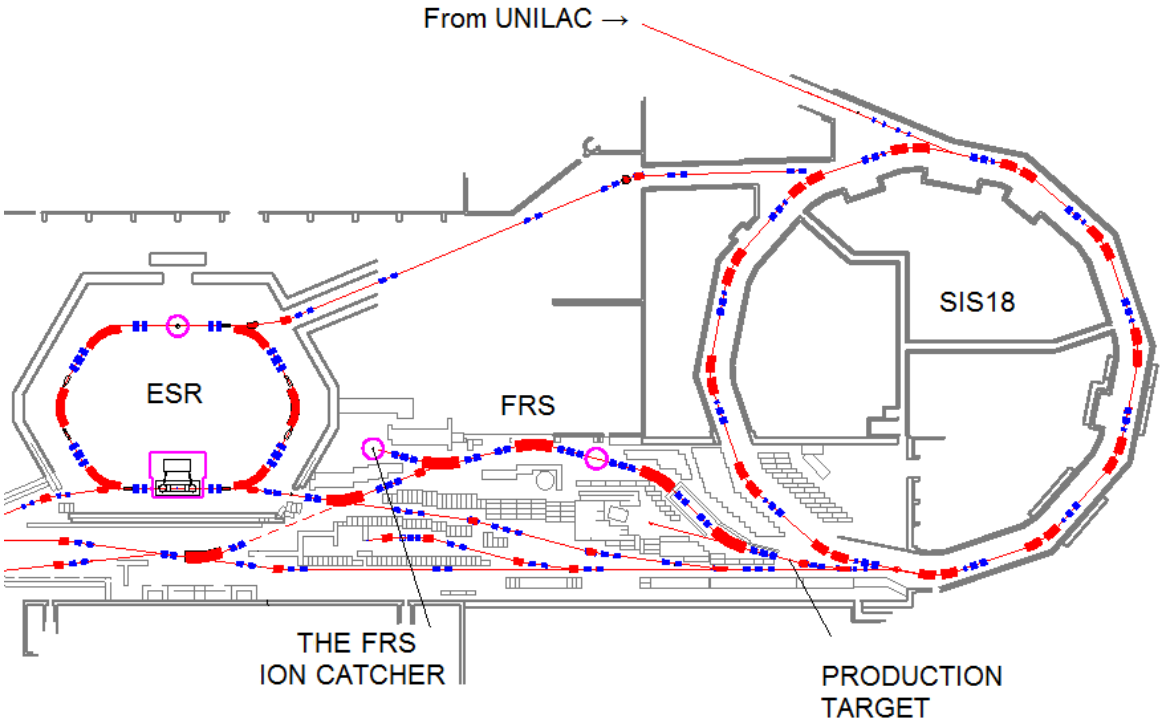

Figure 2.1: Schematic layout of the high-energy part of the GSI facility. It consists of the heavy-ion synchrotron SIS18, the fragment separator FRS and the experimental storage ring ESR. The FRS Ion Catcher is positioned at the final focal plane of the FRS.

able degrader system is installed. The in-flight separation is done with the so-called $B\rho - \Delta E - B\rho$ method (see Subsection 1.2.2). For selection of the secondary beam the horizontal x- and vertical y-slits are used. The degrader system consists of two wedges, two identical counter-rotating wedge-shaped discs, and a set of homogeneous slabs of different thickness, all made out of aluminum. The combination of these aluminum blocks allows a precise and flexible set up of the resulting degrader shape and thickness. The degrader can be set up for an achromatic mode, where maximum spatial isotopic separation is reached, or for a monoenergetic mode providing optimum energy bunching [Geissel et al., 1989]. For the experiments with the FRS Ion Catcher, the monoenergetic mode is favorable. The areal density of the buffer gas inside of the CSC is small compared to the range distribution of the incoming ions. Therefore, a compressed range distribution leads to a larger amount of ions being stopped and measured in the FRS-IC.

The FRS is equipped with a number of detectors for in-flight particle identification (PID) and intensity monitoring. The intensity of a primary beam is measured with a secondary electron transmission monitor (SEETRAM). In the central and in the final focal planes, plastic scintillator detectors (SCI) and time projection chambers (TPC) [Janik et al., 2011] are installed for the time-of-flight and magnetic rigidity measurements. Multiple sampling ionization chambers (MUSIC) [Pfützner et al.,

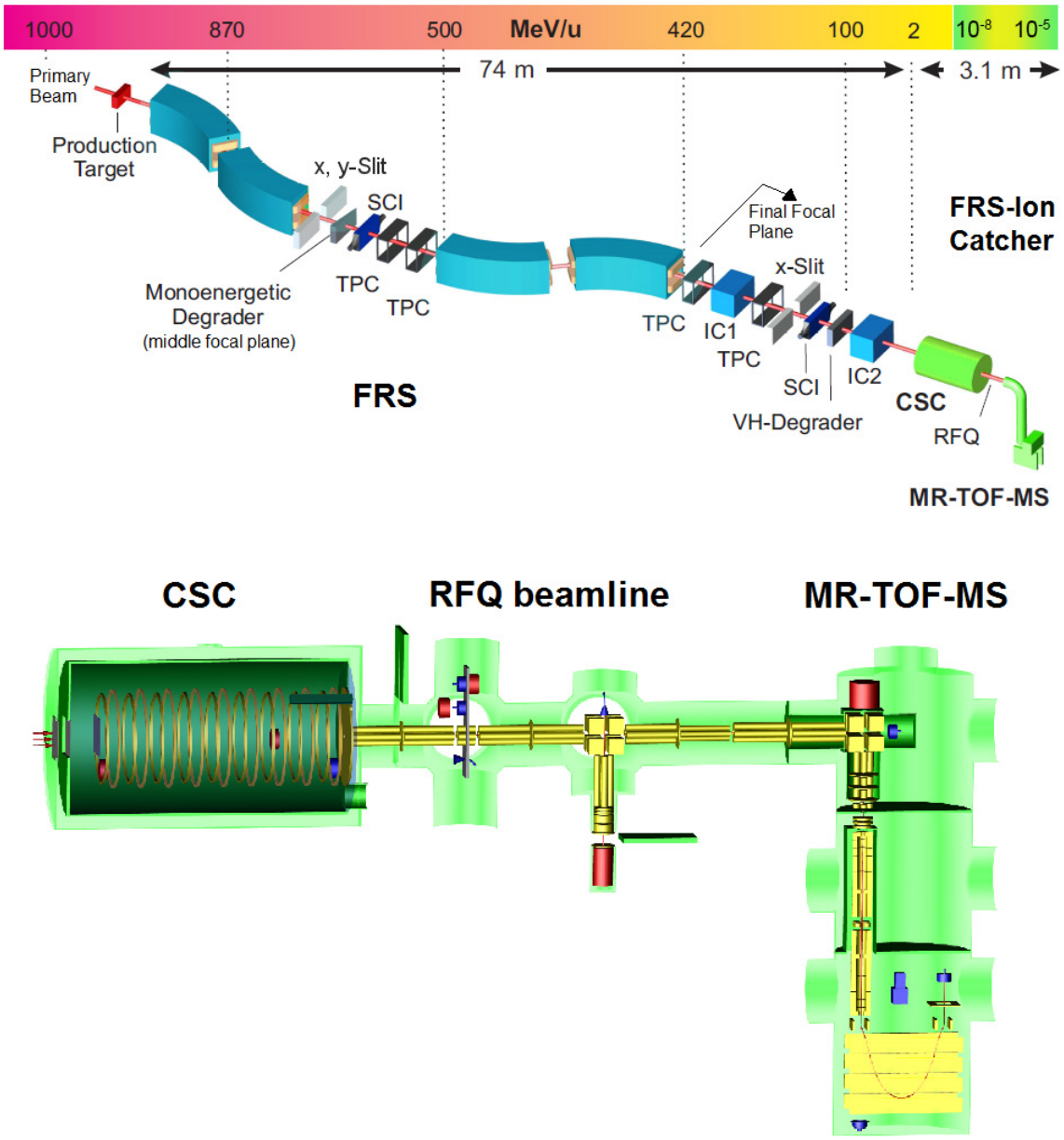

Figure 2.2: Schematic view of the fragment separator (FRS) and the FRS Ion Catcher. The color scale on top of the picture indicates the energy of the ion beam passing through the experimental setup. Particle identification detectors of the FRS are labeled. Exotic nuclei are produced at relativistic energies, separated in-flight, energy bunched in the FRS, and delivered to the FRS Ion Catcher. There, the ions are thermalized in the cryogenic stopping cell, extracted into the RFQ beamline and measured with the MR-TOF-MS.

1994, Stolz et al., 1999] are used for measurements of the energy deposition. All these detectors provide event-by-event identification of the transmitted ions.

In addition, a homogeneous degrader and a MUSIC are positioned directly in front of the stopping cell. They are used for adjusting the final energy of the ions in order to maximize the number of ions stopped in the CSC.

2.2 The FRS Ion Catcher

The FRS-IC was developed and successfully commissioned during a series of experiments with ion beams at GSI. It allows mass measurements of short-lived exotic nuclei with high accuracy and resolving power and can also be used for reactions and decays studies. Masses of the exotic nuclei can be determined at a resolving power of up to 10^6 in only ~ 50 ms after their production [Will, 2019]. High efficiency of the setup allows measurements of nuclei with sub-μbarn production cross sections in only a few hours of operation. In this section, the components of the FRS-IC are described in detail.

2.2.1 Cryogenic stopping cell

The cryogenic stopping cell incorporates a number of novel concepts and techniques [Purushothaman et al., 2013, Ranjan et al., 2015, Reiter, 2015]. It was the first gas-filled cell in the world designed for the stopping of relativistic ion beams produced at 1000 MeV/u, which was operated at high buffer gas densities at cryogenic temperatures and used an RF structure for ion extraction. A combination of its performance parameters makes it a state-of-the-art device with superior characteristics compared to similar devices. Technical details on instrumentation and operation parameters of the CSC are discussed in the following.

Challenges and solutions

In hybrid facilities (see Subsection 1.2.3), gas-filled stopping cells are used for the final slowing down and thermalization of ions. In order to make efficient use of a secondary beam, the stopping cell must have high total efficiency. The total efficiency can be described by

$$\epsilon_{\text{total}} = \epsilon_{\text{stop}} \times \epsilon_{\text{ext}}, \tag{2.1}$$

where ϵ_{stop} is the stopping efficiency and ϵ_{ext} is the extraction efficiency. The stopping efficiency is the fraction of the incoming beam, which is thermalized in the stopping cell. The extraction efficiency reflects losses during the extraction process.

Beams of exotic nuclei are produced in the fragment separator at GSI accelerator facility at relativistic energies of up to 1000 MeV/u. In order to efficiently convert them into low-energy beams, a stopping cell with a high areal density of buffer gas of more than a few mg/cm^2 is required (see Subsection 1.3.1). For the fast extraction of thermalized nuclei out of the high-density stopping cell, electric fields are used. This requires the nuclei to be stopped in an ionic state. In this case, the total efficiency (Eq. (2.1)) includes an additional component, the ion survival efficiency ϵ_{sur}, which reflects ion losses due to neutralization and chemical reactions in the buffer gas.

During the thermalization and extraction processes, ions do multiple collisions with the buffer gas atoms and undergo charge-exchange reactions. If a collision occurs with an atom, which has a lower ionization potential than the incoming ion, then the ion can capture an electron and be neutralized. In this regard, helium is an ideal buffer gas because of its high first ionization potential. In helium gas, isotopes of about $\sim$ 60 % of all chemical elements will be thermalized as doubly-charged ions. Isotopes of other elements will be extracted as triply- ($\sim$ 30 %) and singly-charged ($\sim$ 10 %) ions. The situation changes drastically if some contaminants are present in the system. In collisions with a contaminant molecule, which has a lower ionization potential, the ions of interest are neutralized and lost for the measurement. The cleanliness requirements are much more challenging for high-density stopping cells because there the ions undergo more collisions during their extraction and have a higher probability to be neutralized for the same purity of the buffer gas. For the stopping cell with an areal density of a few mg/cm^2, a buffer gas purity on the level of sub-ppb is required in order to prevent ion losses due to neutralization [Reiter, 2015].

To reach such a level of purity of the buffer gas, many important steps have to be taken. Cool-down of the stopping cell to the cryogenic temperatures helps in removing most of the contaminants out of the system. In this case, the stopping cell works as a big cryopump [Bentley, 1980], where contaminant molecules freeze-out on the walls of the device. As can be seen from Fig. 2.3, already at the temperatures of 70 K many unwanted impurities are reduced to partial pressures at the level of less than 10^{-8} mbar. However, the pumping speed of the cryopump is significantly reduced once a first monolayer is absorbed. Therefore, it is important to keep the amounts of residual gas in the system before cooling down as low as possible. For this purpose, before the cool-down procedure, the system has to be baked and pumped. Another source of contamination is the buffer gas itself. Helium of sub-ppb purity is not available commercially. It still contains different impurities, above all noble gases, in trace amounts. These contaminants also have to be removed or strongly suppressed.

The efficient and fast extraction of ions out of the high-density stopping cell is another challenge. First of all, the technical design of the device has to allow the use of strong extraction electric fields. This, in turn, requires a very fine RF structure for the efficient extraction of ions, as it is indicated by Eq. (1.19). In addition, the extraction efficiency of the stopping cell can be also limited by space charge effects. During the thermalization, one incoming ion produces multiple helium ion-electron pairs. Electrons, due to their high mobility, are removed with electric fields out of

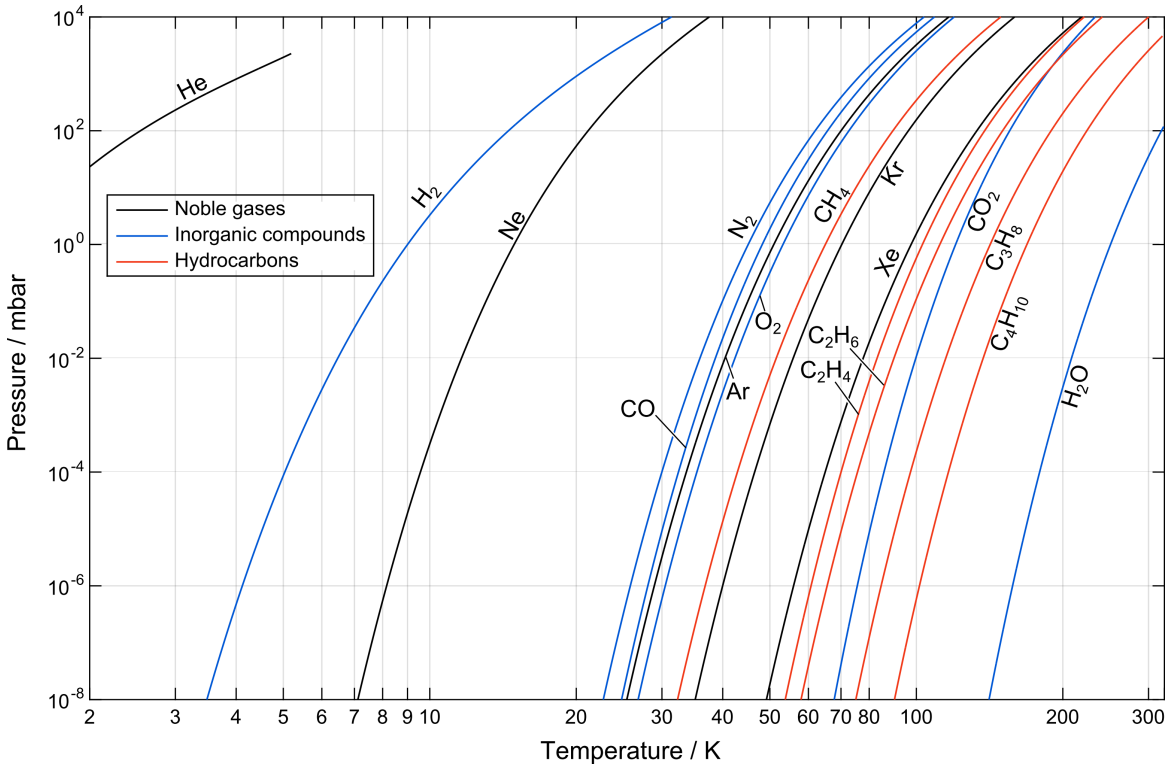

Figure 2.3: Vapor pressure of different gases at different temperatures [Bentley, 1980]. Picture modified from [Pohjalainen, 2018].

the stopping volume very fast, compared to the positive helium ions, which form at cryogenic temperatures He_3^+ clusters and have velocity similar to the one of the stopped ion of interest. At high rates of the incoming beam, this can lead to a build-up of a positive charge inside the stopping volume of the stopping cell. Significant space charge can distort the electric fields and cause additional ion losses. High strength of extraction electric field helps to faster remove the produced charge from the stopping volume and to reduce the space charge effects.

Based on these technical requirements, the cryogenic stopping cell for the FRS Ion Catcher was designed, built and commissioned [Ranjan et al., 2015, Reiter, 2015].

Technical design

Figure 2.4 shows a schematic view of the CSC. It is a double-chamber vacuum vessel. The outer chamber provides an insulating vacuum for the inner one, which is filled with helium gas at cryogenic temperatures of $\sim 70 - 80$ K. Both chambers have thin metal windows installed in the position of the incoming ion beam. The windows are made of stainless steel and have a thickness of 100 μm. Ions enter the stopping cell through the beam windows, lose their residual energy in multiple collisions with helium buffer gas atoms and stop inside the inner chamber.

As the next step, the stopped ions are transported towards the extraction nozzle by

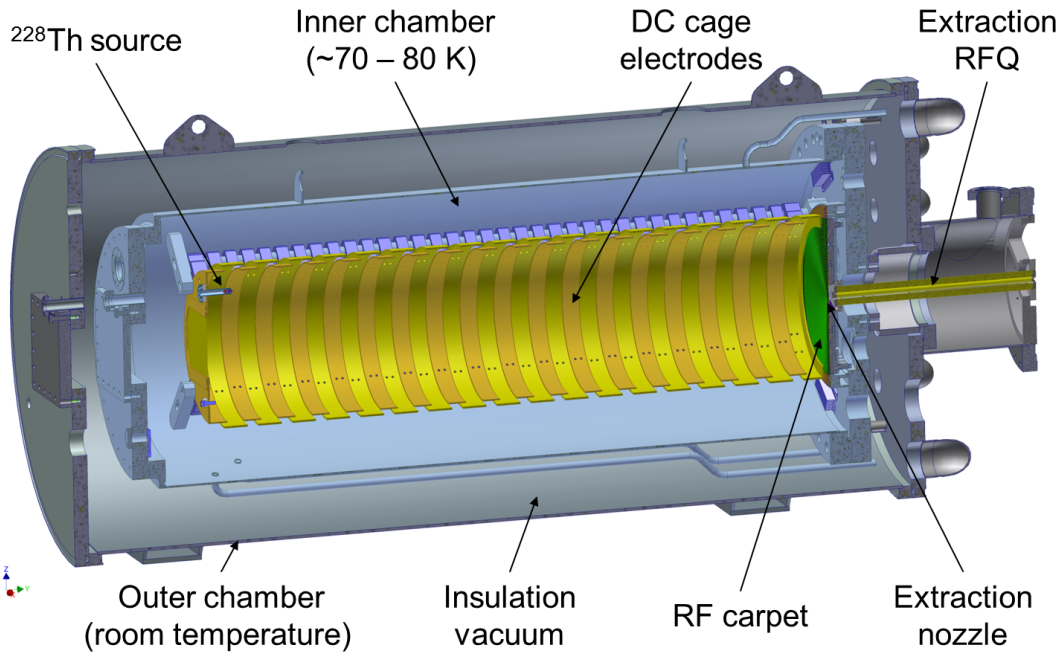

Figure 2.4: Schematic figure of the cryogenic stopping cell (CSC) in a sectional view. Ions are thermalized in the inner chamber of the CSC, guided by electric fields towards the extraction nozzle and extracted with a gas flow into the RFQ beamline.

electric fields. A DC field, which pushes the ions to the exit side of stopping cell (DC push field), is created by 36 overlapping concentric ring electrodes. These electrodes form a cage structure (DC cage) with a diameter of 25 cm and a length of 105 cm, defining the effective stopping volume of the device. At the exit side of the inner chamber, a PCB-based RF electrode structure called the radio-frequency carpet is installed. There, by a combination of RF and radial DC electric fields, the ions are guided towards the extraction nozzle. Once the ions reach the vicinity of the nozzle, they are extracted with the gas flow into the RFQ beamline.

In the inner chamber of the CSC, two ion sources are installed: a ^{228}Th recoil source and a discharge ion source. Ions produced by these sources are used for off-line investigations and tests. All steps of system operation from stopping and extracting of the ions to high-resolution mass measurements with the MR-TOF-MS can be tested. Installation and characterization of these sources were conducted in the frames of this thesis. The details are given in Sections 3.1 and 3.2.

One of the crucial components of the CSC is the RF carpet. It prevents the ions from hitting the chamber wall and being neutralized and focuses them radially. It has a diameter of 25 cm and consists of five conductive layers separated by insulating material (Rogers RO4003/RO4350). A schematic drawing of the RF carpet is shown in Fig. 2.5. The outer layer has 500 concentric ring electrodes, which have a height of 30 μm and a width of 100 μm. The distance between the neighboring rings is 150 μm. The electrode density is 4 electrodes per mm. To the electrodes, two types of voltages

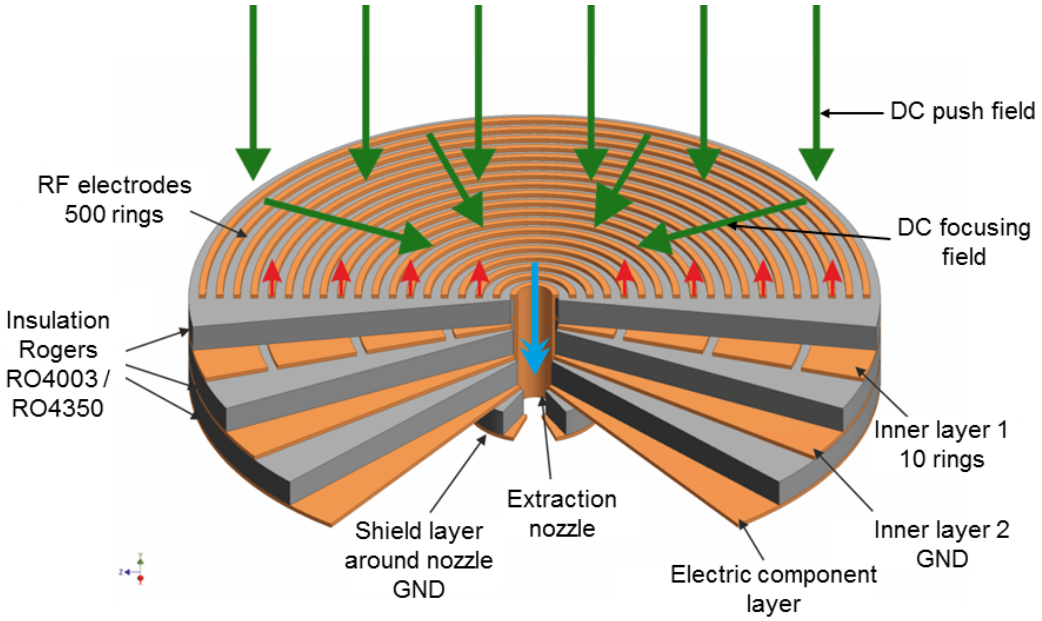

Figure 2.5: Schematic drawing of the RF carpet [Reiter, 2015]. All layers are shown in a sectional view. Conductive elements are shown in orange; insulation material – in gray. Green arrows indicate the DC electric fields; red arrows – RF electric field; blue arrow – the direction of the gas flow.

are applied: (i) RF voltages, shifted by 180° between neighboring electrodes; and (ii) DC voltages. The RF voltages create an effective repelling field, which counteracts the DC push field and prevents the ions from hitting the electrodes. The ions are kept at a distance of ~ 100 μm above the RF carpet surface. The DC voltages applied to the ring electrodes create an additional DC field to guide the ions in the direction of the extraction nozzle (DC focusing field).

The second conductive layer of the RF carpet is called inner layer 1. It is segmented into 10 ring electrodes and used for the reduction of field penetration effects. Such effects may lead to the formation of potential pockets and disturbances of the ion motion along the RF carpet. The inner layer 1 provides fine control of the DC field in front of the outer layer and allows the RF carpet to be operated at any offset potentials.

The third layer (inner layer 2) is grounded and used for electric shielding of the fourth layer, where the electric components are mounted. The last, fifth layer shields the ion pathway behind the RF carpet. In the center of the RF carpet, the extraction nozzle is positioned. It has a cylindrical shape and a diameter of 0.6 mm. The total thickness of the RF carpet is 1315 μm.

In order to reach high ion survival efficiency of the CSC, high cleanliness of the system has to be ensured. As it was mentioned before, the stopping cell is operated at cryogenic temperatures of $\sim 70-80$ K, but this is only one of the required technological steps. To reduce the amounts of residual gas inside the CSC, the inner chamber is first

baked at a temperature of about 400 K and constantly pumped by a turbomolecular pump for a few days. For baking, a special PTFE-coated copper wire is used, which is wound around the walls of the inner chamber. After the baking, the inner chamber is separated from a pump, and the cooling is started.

To reach cryogenic temperatures, a custom-made cooling system is used [Ranjan et al., 2015]. The cooling system is mounted in a dedicated valve box and consists of a cold head and a cryofan. The coolant (helium gas at pressures of up to 10 bars) is cooled down by the cold head and circulated in a closed circuit by the cryofan. The lines of the cooling circuit are connected via cryogenic feedthroughs to two cooling channels wound around the inner chamber of the CSC. The valve box provides an insulating vacuum for the cooling circuit and also has an incorporated dewar filled with liquid nitrogen LN_2. At the beginning of the cooling-down procedure, the helium gas can be precooled in the internal dewar, which significantly reduces the time required for reaching cryogenic temperatures. A typical time of the cooldown is about 24 hours. After a few days of cooling, temperatures reach as low as 60 K for the inner chamber walls and 75 K for the helium buffer gas.

The helium buffer gas is supplied into the inner chamber through a separate gas line. In order to remove the contaminants contained in the buffer gas, a MicroTorr helium purification getter is installed in the gas line. In addition, before entering the CSC, the helium gas passes through a heat exchanger coupled to the cooling circuit. The heat exchanger has a temperature of 55 K and, therefore, acts like a cold trap purifying the buffer gas even further. It also precools the He gas, which helps to decrease the heat input into the cryogenic environment. In order to reduce the amounts of noble gases contained in the buffer gas, in the inner chamber of the CSC, a small container filled with activated charcoal is installed. The activated charcoal has a huge surface area of about 1000 m^2/g and can be used as a very efficient adsorption material at cryogenic temperatures. In combination, all mentioned steps result in a high cleanliness of the CSC, which is ideal for ion survival.

Performance parameters

Performance characteristics of the CSC were investigated experimentally with ion beams at GSI. In the beam time in 2014, total efficiencies ϵ_{total} of up to ~ 22 % were measured [Reiter, 2015]. The total efficiency was calculated from the ratio of the measured number of extracted and detected ions to the number of ions entering the CSC. The number of incoming ions was determined accurately by the particle identification detectors of the FRS. The stopping efficiency ϵ_{stop} was calculated from the measured range distribution of ions and known areal density of the buffer gas. Maximum ϵ_{stop} of ~ 27 % was reached. The combined survival and extraction efficiency $\epsilon_{\text{sur+ext}} = \epsilon_{\text{sur}} \times \epsilon_{\text{ext}}$ can be deduced from Eq. (2.1). For the ions of different elements produced by in-flight fragmentation of ^{238}U at 1 GeV/u, $\epsilon_{\text{sur+ext}}$ of more than ~ 60 % was reached [Plaß et al., 2019]. The obtained efficiencies values are unprecedented for the thermalization of fragments produced at relativistic energies with the gas-filled stopping cells.

Within the frames of this thesis, a few improvements and upgrades have been implemented in the system in order to further increase the efficiency. The CSC can now be operated with areal densities of the buffer gas almost factor of two higher than in the past. The safe long-term operation of the device with areal densities of up to $\sim$ 10 mg/cm^2 (150 mbar of helium gas at 75 K) was demonstrated (see Section 3.3 for details). The increase in the buffer gas areal density leads to the corresponding increase in the stopping efficiency. The cleanliness of the device has also been improved. Therefore, the higher total efficiency of the CSC is expected and has to be justified in the FAIR Phase-0 experiments.

A mean extraction time (i.e. the time required for ion extraction from the center of the CSC) of $\sim$ 25 ms was demonstrated [Purushothaman et al., 2013, Reiter, 2015]. It was also shown that the extraction time is constant for different values of the buffer gas areal density, as for the higher densities the higher DC electric fields can be applied. The fast extraction time gives access to very short-lived exotic nuclei. This feature of the FRS Ion Catcher was used in the past years to perform first direct mass measurements of short-lived nuclei in the region of the nuclide chart below ^{208}Pb [Ayet San Andrés et al., 2019].

The rate capability of the CSC was investigated experimentally and in simulations performed with SIMION [Manura and Dahl, 2006] software. The results demonstrated that the CSC can be operated with rates of incoming ions of up to 10^4 ions/s without efficiency losses [Reiter et al., 2016]. Complementary studies have been conducted as a part of this doctoral thesis in a beam time in 2016 and are discussed in detail in Section 4.1.

2.2.2 RFQ beamline

Behind the cryogenic stopping cell, the low-energy RFQ beamline is installed. A design and operation capabilities of the RFQ beamline are based on several novel concepts [Plaß et al., 2007, Petrick et al., 2008, Petrick, 2008, Reiter, 2015, Haettner et al., 2018]. It is a compact, multi-purpose ion transport system allowing for cooling, bunching and mass separation of ions. The RFQ beamline is also used as a differential pumping stage separating the high-density CSC and the MR-TOF-MS, which requires low pressures of less than 10^{-6} mbar for operation. In addition, different tools for beam diagnostics and transport optimization are implemented into the beamline.

The rods of RFQs are built from resistive carbon-filled PEEK material [Takamine et al., 2005, Simon, 2008]. They have a diameter of 11 mm and are positioned in a radial distance of 10 mm away from each other. A combination of RF and DC voltages is applied to the rods in order to constrain the ions radially and transport them in a longitudinal direction.

Figure 2.6 shows a schematic drawing of the RFQ beamline. The extraction RFQ is followed by the diagnostics unit 1 (DU1) and the diagnostics unit 2 (DU2) [Hornung

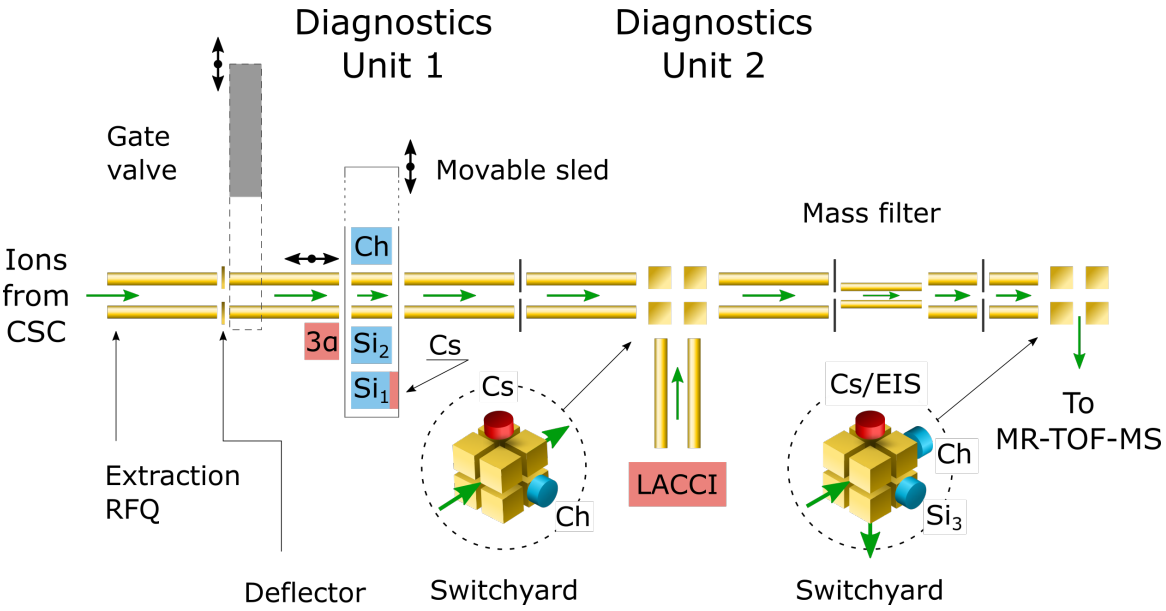

Figure 2.6: Schematic drawing of the RFQ beamline. The main components are labeled. Ions are extracted out of the CSC into the RFQ beamline and transported to the MR-TOF-MS. Green arrows indicate the DC electric fields; black arrows – possible directions for mechanical movement. Channeltron (Ch) and (Si) detectors, as well as a laser ablation carbon cluster ion source (LACCI), a three-line alpha source (3α), thermal alkaline sources (Cs), and an electron impact ion source (EIS) are shown schematically.

et al., 2018]. Directly behind the extraction RFQ, a dipolar deflector is positioned. It can be used for defining the time structure of the extracted beam or for reducing the count rate if the ions come at too high rates.

In the DU1, a movable sled is installed. The sled is moved in direction perpendicular to the beamline by in-vacuum motors and a gear system. On the sled, apart from an RFQ segment, a channeltron detector (Photonis 5901 Magnum Electron Multiplier) and two silicon surface barrier detectors (Ortec Ultra BU-016-150-100 bakeable) are installed. At a distance of 5 mm in front of each silicon detector, aluminum foils are installed. These foils have a thickness of 50 μg/cm^2 and are operated at the high negative potential for the collection of radioactive nuclei [Reiter, 2015]. In less than a minute, the detectors can be moved into the beamline for ion counting or alpha-spectroscopy measurements. Next to the RFQ beamline, a three-line alpha source (a mixture of alpha-decaying ^{239}Pu, ^{241}Am, and ^{244}Cm isotopes) is installed in such way that the detectors can be moved in front of it for commissioning and calibration. In combination with the extraction RFQ operated as a mass filter [Miskun, 2015, Miskun et al., 2015], the detectors provide a broad range of possible applications, such as investigations of extracted beam composition, charge state identification and improvement of the beam quality for the following mass measurement with the MR-TOF-MS. Operated in the mass-filtering mode, the extraction RFQ can reach mass resolving power of up to $\sim$ 150. More details on the performance of the mass filter and its contribution to the selectivity of the setup are given in Subsection 3.4.1.

If the detector sled is moved out of the beamline completely, it is possible to retract the RFQ segment in the direction of the MR-TOF-MS and separate the CSC from the downstream system by a gate valve [Reiter, 2011]. This gives the advantage of independent maintenance of one part of the system without the need of breaking the vacuum in another. In particular, quick checks in the vented beamline can be done while the stopping cell is kept at cryogenic temperatures and constantly pumped.

The DU2 consists of an RFQ switchyard [Greiner, 2013b, Plaß et al., 2015], a dedicated mass filter and a laser ablation carbon cluster ion source (LACCI) [Gröf, 2017, Hornung, 2018]. The switchyard is a novel device, which consists of 8 cubic electrodes. It effectively acts like six perpendicular radio-frequency quadrupoles and can be used for transporting ion beams, bending them by 90 degrees, splitting and merging the beams coming from different directions. It allows feeding of calibrants ions into the beam of ions extracted out of the CSC for their simultaneous measurement in the MR-TOF-MS. An identical switchyard is also installed at the end of the RFQ beamline on the top of the MR-TOF-MS. On the RFQ switchyards, additional channeltron and silicon detectors are mounted for the ion transport optimization.

Calibrants required for the mass measurements and transmission optimization are produced in the RFQ beamline with various sources. Thermal alkaline sources are mounted on the RFQ switchyards and on the movable sled of the DU1. Ions produced by these sources are also used for the commissioning of the RFQ beamline and the MR-TOF-MS independently of the operation of the CSC. LACCI produces ions of carbon clusters containing different isotopes of carbon and, therefore, provides isobaric calibrants for high-accuracy mass measurements over a very broad mass range. Targets made from other materials (e.g. gold, silver, copper, etc.) can be also used for the production of calibrants. The calibrants ions are produced with the same repetition rate as the MR-TOF-MS ($50 - 100$ Hz) and with controllable rates, which are stable over a couple of days. The dedicated mass filter is used in order to remove the ions of unwanted masses, to reduce the background and to increase the cleanliness of measured spectra. In addition, on the second RFQ switchyard, an electron impact ion source is installed. By operating the electron impact source with different gases (e.g. SF_6, Xe or C_3F_8), ions covering a broad mass range can be produced [Ebert, 2016]. These ions then are also used as the calibrants for high-accuracy mass measurements.

The DU2 provides an additional differential pumping stage further separating pressures in the CSC and in the MR-TOF-MS. In addition, the vacuum system has been upgraded within the frames of this thesis. This has lead to an increase of a factor of five in the pumping speed of the prevacuum lines. These two improvements - the additional differential pumping stage and the vacuum system upgrade - resulted in a higher possible areal density of the buffer gas inside the CSC (see Section 3.3 for details).

2.2.3 Multiple-reflection time-of-flight mass spectrometer

The RFQ beamline is followed by the MR-TOF-MS. This is a universal and very powerful tool for ultra-high-resolution measurements of exotic nuclei [Ayet San Andrés et al., 2019], which can also be used as an isobar [Plaß et al., 2008a] or even an isomer [Dickel et al., 2015a] separator. The MR-TOF-MS is extensively described in [Dickel, 2010, Dickel et al., 2015b, Plaß et al., 2015, Yavor et al., 2015]. It is a broad-band, fast, and non-scanning mass spectrometer yielding very high resolving power (up to 10^6 [Will, 2019]) and sensitive to single ions. As part of the FRS Ion Catcher, the MR-TOF-MS was successfully used for the particle identification in the FRS as a mass tagger [Reiter, 2015] and for direct mass measurements [Hornung, 2018]. It is a very effective tool for the new isotopes and isomers search.

Figure 2.7 shows a schematic drawing of the MR-TOF-MS. From the RFQ switchyard ions are transported to a triple-stage injection trap system [Jesch, 2008], where they are accumulated, cooled and bunched. Then, the ions are injected as a bunch into the time-of-flight analyzer, where they fly a controllable amount of turns. The analyzer consists of a field-free drift tube and two reflecting electrostatic mirrors. In the center of the analyzer, the mass-range selector (MRS) is installed. This is a quadrupolar deflector, which can be pulsed in order to deflect the unwanted ions and purify the measured spectra. With the MRS, the ion selection down to window size of 1 u/e can be achieved. Once the ions are ejected from the analyzer, they pass through a time-focus shift reflector [Yavor et al., 2015, Dickel et al., 2017] and reach the movable sled. On the sled, an isochronous secondary electron multiplier (SEM) (ETP MagneTOF DM 167 from SGE Analytical Science Pty Ltd.), a silicon surface barrier detector (Ortec Ultra BU-016-150-100 bakeable), and a Bradbury-Nielson ion gate (BNG) [Bradbury and Nielsen, 1936] are mounted. An additional silicon detector is positioned behind the BNG. The BNG is a fast electrical switch, which can be set to deflect the unwanted ions to the gate detectors and to transmit only the ions of interest. The movable sled allows fast switchover between the different detectors.

The MR-TOF-MS can be operated in three different modes:

1. **Time-focus shift (TFS) mode** — the ions fly through the analyzer just once, no reflections are done. The time-of-flight spectrum is measured by the MagneTOF detector and converted to the mass spectrum later. An analog signal on the detector is digitized with the Fast ComTec MC6SA Time-to-Digital Converter (TDC). A broadband mass spectrum with a mass-to-charge window of $\sim$ 70 u/e and the mass resolving power of up to 4000 is measured [Dickel et al., 2015b].

2. **High-resolution mass measurement mode** — the ions make multiple turns in the analyzer, which results in a better time-of-flight separation. The time-of-flight spectrum is measured by the MagneTOF detector and converted to the mass spectrum later. An analog signal on the detector is digitized with the TDC. The mass resolving power of up to 10^6 can be reached [Will, 2019].

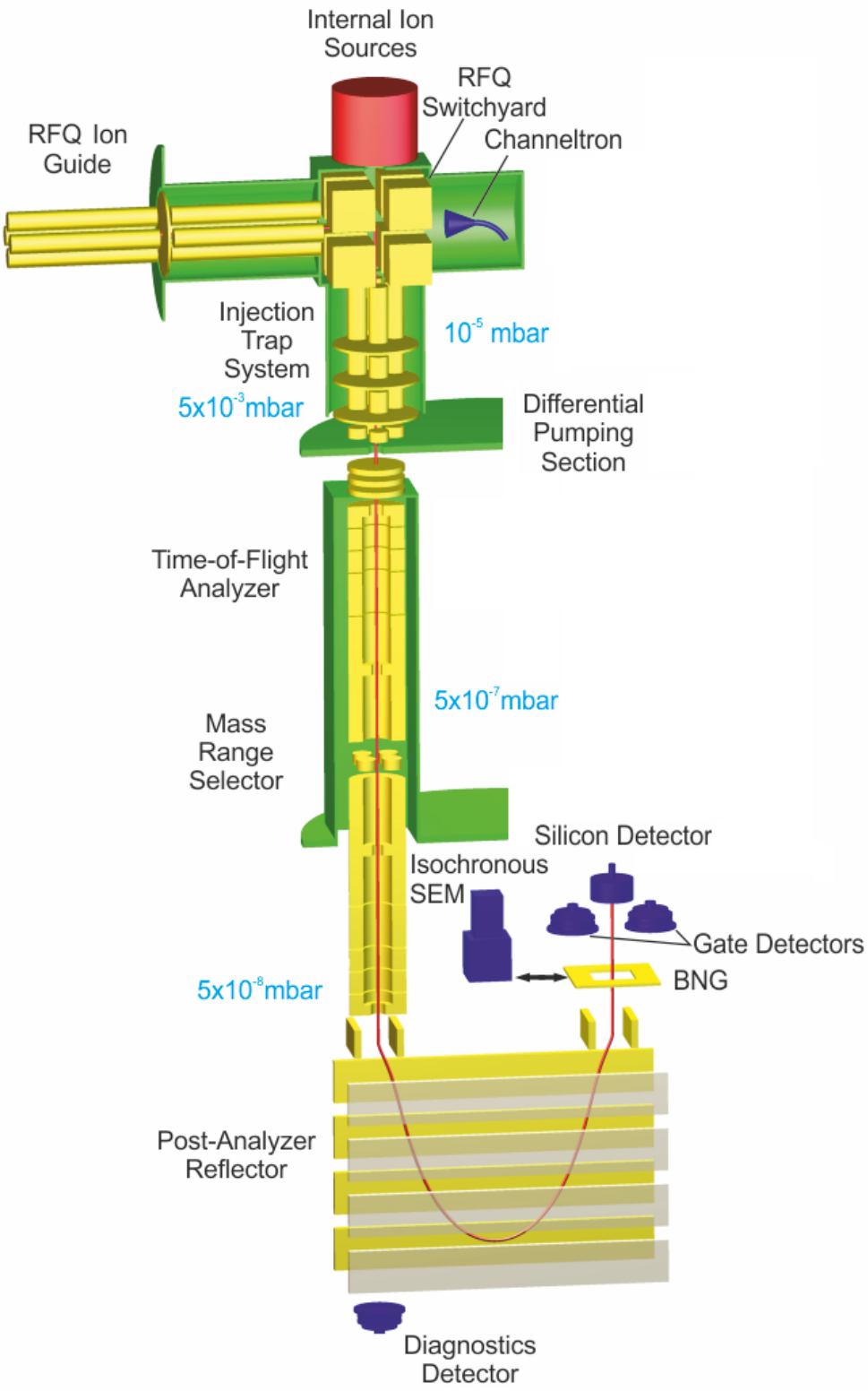

Figure 2.7: Schematic drawing of the multiple-reflection time-of-flight mass spectrometer (MR-TOF-MS). The main components of the system are shown and labeled. Ions are accumulated, cooled and bunched in the trap system, separated after multiple turns in the analyzer and reflected towards the detectors.

3. **Isobar/isomer separation mode** — the ions make multiple turns in the analyzer, which results in a better time-of-flight separation. The ions of interest are transmitted by the BNG, whereas other ions are deflected. Isobarically and isomerically clean beams can be produced [Dickel et al., 2015a].

2.3 Data analysis procedure

The data measured with the MR-TOF-MS are analyzed with an elaborated analysis procedure. The challenge of the analysis lies in the fact that it is necessary not only to perform accurate and robust determination of the mass and abundance of each measured ion species but also to be able to treat low-statistics cases and overlapping distributions of different ion species, which sometimes have abundances that are different by orders of magnitude. Details of the data analysis procedure are described in [Ebert, 2016, Jesch, 2016, Ayet San Andrés, 2018, Hornung, 2018, Ayet San Andrés et al., 2019]. In this section, only the main steps are presented.

For the data analysis, two software packages are used: the mass acquisition software MAc [Bergmann, 2020] and the software for statistical computing and graphics *R* [*R* Core Team, 2018]. The analysis procedure is shown schematically in Fig. 2.8. It consists of the following steps:

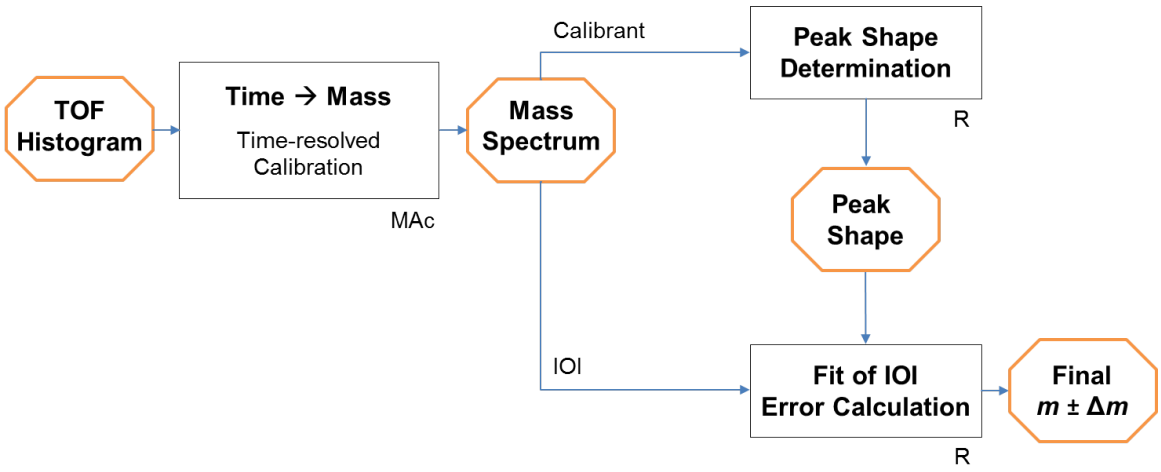

Figure 2.8: A schematic view of the main steps of the analysis procedure performed with the data measured by the MR-TOF-MS. Picture modified from [Ayet San Andrés, 2018].

1. A TOF spectrum of calibrant ions and the IOI is recorded with the MAc software. For this, the digitized signals from the MagneTOF detector are accumulated over a certain number of measurement cycles and displayed in the software as TOF histograms. A typical number of accumulation is 50 cycles, which, at a repetition rate of the MR-TOF-MS of 50 Hz, corresponds to 1 spectrum per second.

2. The TOF spectrum is converted into a mass-to-charge spectrum. Required calibration parameters are deduced from the calibrant ions. At this step, also the so-called time-resolved calibration (TRC) can be performed. TRC allows to correct drifts of the peak positions in time. Such drifts are caused by voltage fluctuations of power supplies or by contraction and expansion of the mass analyzer due to the temperature change.

3. The resulting mass spectrum is exported from MAc as a list mode data. To convert the histogram into list mode, each measured event is randomized uniformly within its bin. The exported unbinned data are used in the *R* software for further analysis.

4. In the *R* software, the peak shape determination is performed. A Hyper-EMG function [Purushothaman et al., 2017a] is fitted to the most abundant calibrant peak measured simultaneously with the IOI. The Hyper-EMG (exponentially modified Gaussian) is a Gaussian function convoluted with one or several exponential functions. The peak shape parameters and their uncertainties are determined by a least square (LS) minimization using the Levenberg-Marquardt iteration algorithm [Moré, 1978]. The results are validated with a number of statistical indicators. Accurate knowledge of the peak shape parameters is of great advantage in cases where the peak of the IOI overlaps with another ion peak. Once the peak shape parameters are obtained, the calibrant peak is fitted with the Hyper-EMG function, where only the centroid parameter is free, using a weighted maximum likelihood estimation (wMLE). For the weighting function of the wMLE, the natural logarithm of the determined Hyper-EMG function is used. The obtained centroid, or the mass-to-charge value, of the calibrant is used to scale the peak shape parameters for the fitting of the IOI and to calculate the peak shape error.

5. The peak of the IOI is fitted with the scaled Hyper-EMG function using the wMLE. The abundance of the peak and its centroid, i.e. the mass-to-charge of the IOI, are determined. The total mass uncertainty including multiple contributions of different errors (e.g. the statistical error, the peak shape error, the calibrant error, the TRC error, etc.) is calculated. For details on different contributions to the total uncertainty, see [Ayet San Andrés et al., 2019].

2.4 Experimental conditions and operating parameters during the GSI beam time of 2016

As it was mentioned before, the FRS Ion Catcher was successfully commissioned during the series of experiments with ion beams at GSI in 2011-2016. Apart from the characterization of the setup, it was also possible to perform first mass measurements of the exotic nuclei [Dickel et al., 2015a, Ayet San Andrés et al., 2019] and obtain physics results. In this thesis, the results of selected measurements performed during

the beam time of 2016 will be discussed.

In the beam time of 2016, two measurement campaigns with different primary beams of different energies and intensities were done. In the first measurement block, a 300 MeV/u ^{238}U beam was focused on a beryllium target with an areal density of 0.27 g/cm^2. The intensity of the primary beam was up to $2.5 \cdot 10^8$ ions/spill with a spill length of 1 s. Neutron-deficient exotic nuclei were produced by projectile fragmentation reaction. In the second block, the exotic nuclei were produced in the fragmentation of a ^{124}Xe primary beam at an energy of 600 MeV/u on a 1.622 g/cm^2 Be target. The intensity of the ^{124}Xe primary beam was up to $1 \cdot 10^9$ ions/spill with a shorter spill length of 0.5 s.

Due to the low energies of the primary beams, not all of the FRS beamline components described in Section 2.1 could be used. In the central focal plane, the horizontal x- and vertical y-slits were installed, followed by the scintillator (SCI) and the variable degrader system. For the degrader, only two counter-rotating wedge-shaped aluminum discs were used in order to minimize the amount of matter in the way of the beam. In the final focal plane the following sets of the beamline components and PID detectors were used: a) for ^{238}U primary beam: TPC – gas degrader [Purushothaman et al., 2017b] – TPC – x-slits – SCI – homogeneous degrader – MUSIC; b) for ^{124}Xe primary beam: TPC – GEM-TPC [Garcia et al., 2017] / MUSIC – TPC – MUSIC – x-slits – SCI – homogeneous degrader – MUSIC.

The FRS Ion Catcher was operated in a configuration shown in Fig. 2.9. The RFQ beamline extension described in Subsection 2.2.2 was implemented to the system later in 2018. The operating parameters of the FRS Ion Catcher are given in Table 2.1. This set of parameters is a default setting, which was used in the measurements described in this thesis, if not stated otherwise. The isolation-dissociation-isolation technique (see Subsection 3.4.1) was used for the measurements of ions produced in the FRS.

During the beam time of 2016, there was a problem with the RF carpet operation. One of the DC voltage connections of the RF carpet was broken, which resulted in slower ion transport along the RF carpet surface. The time of ion extraction out of the CSC was, therefore, increased. Measurements of the extraction time showed that after the ions reached the RF carpet surface they were stored there for an additional time ranging from 0 to 170 ms. The rate of the extracted ions was uniformly distributed within this time range. The resulting increase and uncertainty of the extraction time were not crucial for the measurements discussed in this work. Corresponding corrections and uncertainties were taken into account and are discussed in the following chapters.

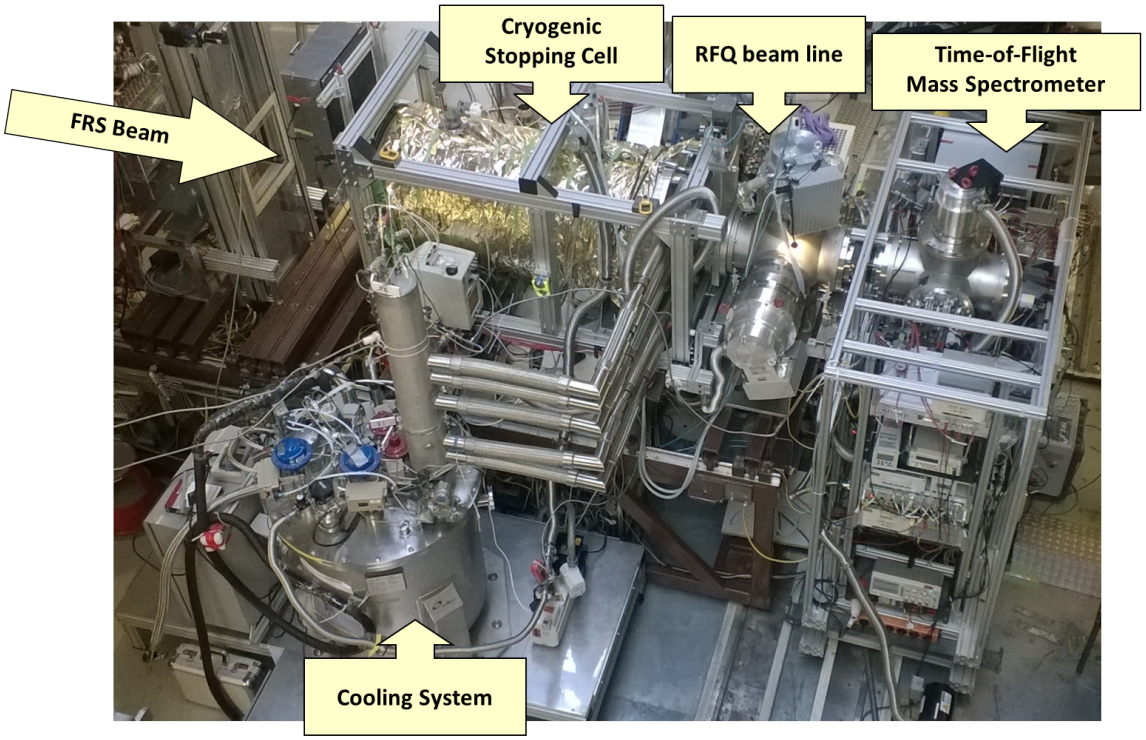

Figure 2.9: Photograph of the FRS Ion Catcher setup in the configuration used in the GSI beam times of 2014 and 2016. The main components of the setup are labeled.

	Parameters	**Value**
CSC	DC push field towards the RF carpet	17 V/cm
	DC focusing field along the RF carpet	5 V/cm
	Frequency of the RF carpet	5.93 MHz
	Voltage of the RF carpet	100 $V_{peak-peak}$
	Pressure of the helium buffer gas	$65 - 75$ mbar
	Temperature of the helium buffer gas	80 K
	Areal density of the helium buffer gas	$4.2 - 4.6$ mg/cm^2
RFQ Beamline	Pressure in the RFQs of the DU1	$1 \cdot 10^{-2}$ mbar
MR-TOF-MS	Repetition rate	50 Hz
	Kinetic energy of ions	1300 eV
	Number of turns	up to 560

Table 2.1: Default operating parameters of the FRS-IC during the GSI beam time of 2016.

3 New experimental concepts and improvements

Within the context of this doctoral thesis, several technical upgrades have been implemented in the FRS Ion Catcher setup in order to improve its performance characteristics and its reliability of operation, and to introduce new functional features. New internal ion sources have been installed and characterized. The vacuum system has been upgraded, which, in combination with the extended RFQ beamline [Hornung et al., 2018], results in improved differential pumping. The maximum areal density of the CSC has been increased to 10 mg/cm^2. New techniques for enhancing the selectivity of the ion transport based on ion mobility and by dissociation of molecular contaminants have been developed. The results of the first measurements with the improved system are shown and discussed in this chapter.

3.1 ^{228}Th recoil source

In the frames of this work, a new ^{228}Th radioactive ion source [Alfonso et al., 2015] has been installed in the CSC and characterized. The ^{228}Th source is mounted on the entrance side of the stopping region. ^{228}Th undergoes alpha decay and produces a chain of isotopes of different elements. The decay chain of ^{228}Th is shown in Fig. 3.1 [Greiner, 2017]. The decay products leave the source and either stop in the buffer gas or, in case if there is no buffer gas present, impinge on the inner part of the DC cage ring electrodes. During the CSC operation, the recoils are produced by the decays in the source itself and by the decays of long-lived decay products accumulated on the DC cage electrodes. The decay products are stopped in the buffer gas and can be extracted with electric fields. However, only the recoils that were produced in alpha decay are extracted out of the CSC. The extraction of less-energetic beta recoils was not observed, possibly due to the cryogenic temperatures of operation. It is important to note that ion extraction out of the ^{228}Th source can be switched off electrically without harming the CSC operation. If an electric potential smaller than the potential of the first DC cage electrode is applied to the source, then the recoils stopped in the buffer gas are dragged back towards the source by the electric field. The extraction of the decay recoils produced by the long-lived nuclides on the electrodes can not be switched off. This results in small amounts of the nuclides ^{220}Rn, ^{216}Po, ^{212}Pb, ^{208}Pb, and ^{208}Tl being constantly extracted out of the CSC regardless of the electric potential of the source.

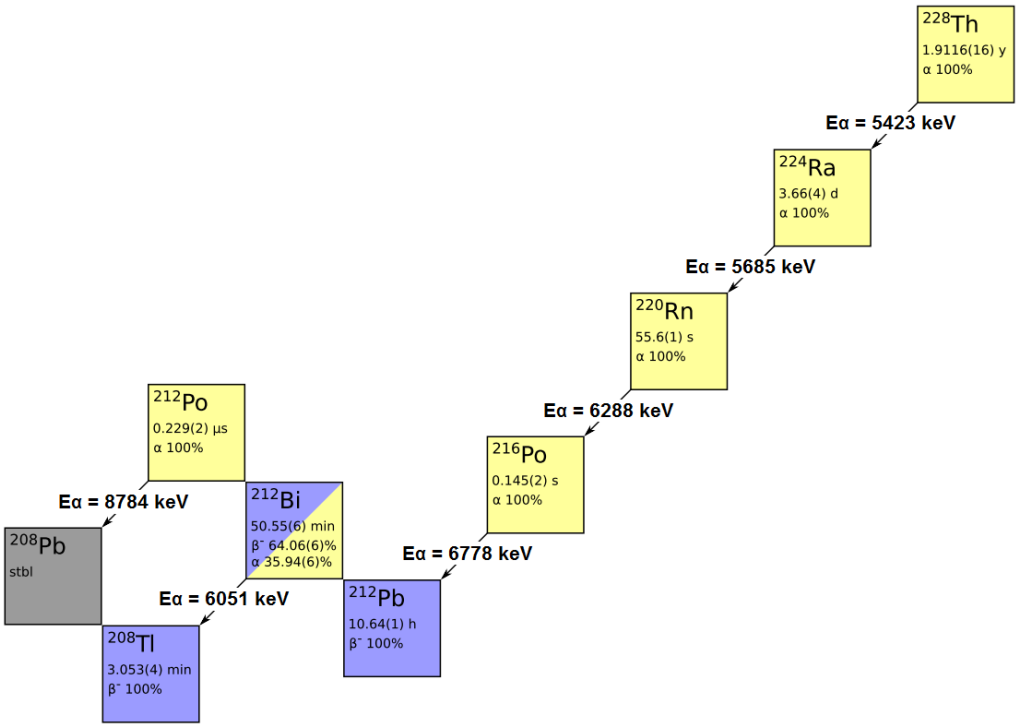

Figure 3.1: Decay scheme of ^{228}Th. Short-lived alpha-decaying products of the ^{228}Th decay chain allow commissioning and optimization of the system using alpha spectroscopy. Alpha-decaying nuclei are colored yellow; beta-decaying nuclei – blue; stable nuclei – gray. Energies of dominant alpha lines are indicated. Picture modified from [Greiner, 2017].

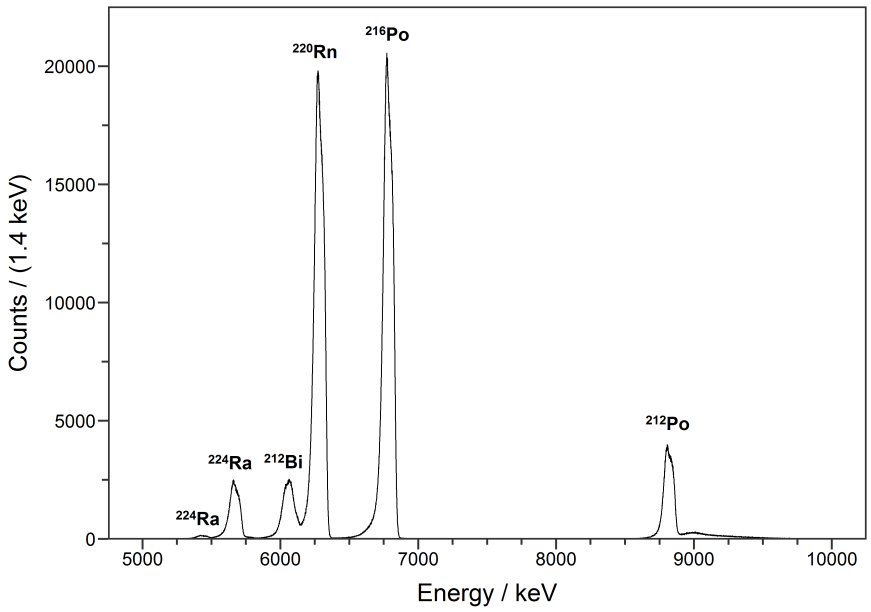

Figure 3.2: Measured alpha decay spectrum of ions produced by the ^{228}Th recoil source. The measurement was done with a silicon surface barrier detector installed in the RFQ beamline.

The ^{228}Th recoil source is mainly used for the commissioning and optimization of ion transport through the system. Short-lived alpha-decaying products allow measurements of extraction and transmission efficiencies by alpha spectroscopy with silicon detectors. For these purposes, multiple silicon surface barrier detectors are installed in different parts of the beamline. In Figure 3.2, a measured alpha decay spectrum of extracted ions produced by the ^{228}Th source is presented. The measurement was done by the silicon detector positioned in the RFQ beamline behind the extraction RFQ. The ions were implanted on a thin aluminum foil in front of the detector. The energies of the emitted alpha particles were measured. All alpha decays of ^{228}Th products were identified. The relative abundances of the peaks corresponding to ^{224}Ra and ^{212}Bi decays are lower than the ones of ^{220}Rn and ^{216}Po because of their long half-lives. The ^{212}Po peak has also smaller abundance, because this isotope is not extracted out of the CSC due to the short half-life (0.229 μs) and is populated only by the β-decay of relatively long-lived ^{212}Bi implanted on the foil in front of the detector. The tail-like structure of the ^{212}Po alpha decay peak occurs due to the fast alpha decay following the β-decay of ^{212}Bi, which results in an additional energy distribution. Similar measurements with the silicon detectors in the downstream beamline allow step-by-step optimization of the ion transport and are necessary in order to achieve maximum transmission efficiency.

One of the most important features of the ^{228}Th source is its half-life ($T_{1/2} = 1.91$ years). Previously, ^{223}Ra recoil sources were used for system commissioning and optimization [Ranjan et al., 2011]. ^{223}Ra has a half-life of $T_{1/2} = 11.4$ days. Maximum activities of these sources were limited by the production mechanism and reached a few kBq only. After two months of operation (approximately, 5-6 half-lives), the activity of the source was too small for fast and accurate off-line investigations. Therefore, every two months a new source had to be installed in the stopping cell. The time required for the source exchange was about 10 working days. By switching over to the 3.7 kBq ^{228}Th source, effectively two months of work per year were spared.

Besides commissioning and optimization of the ion transport with the silicon detectors, the ions produced by the ^{228}Th source can be used for other purposes:

- As the source can be electrically switched off, it is possible to pulse it and to measure accurately the time required for the extraction of ions out of the CSC [Purushothaman et al., 2013].

- Radium and lead isotopes are mostly extracted as doubly-charged ions because of their low second ionization potential (see Section 4.2). As the ion motion in electric fields is defined by the mass-to-charge ratio, the products of ^{228}Th can be used for beamline optimization for two different mass-to-charge ratio regions – around 110 u/e and 220 u/e. All extracted ions can be also used as calibrants for mass measurements with the MR-TOF-MS.

- Among the extracted products of ^{228}Th, there are two isobars – ^{208}Pb and ^{208}Tl. They have a mass difference of 5 MeV. To resolve these isobars a mass resolving power of 40,000 is needed. They can be thus used to tune the MR-TOF-MS for high resolution. Figure 3.3 shows the measured mass spectrum, where ^{208}Pb and ^{208}Tl isotopes are resolved and identified with 256 isochronous turns in the MR-TOF-MS, corresponding to a mass resolving power of $\sim 200,000$.

- In addition, the abundance ratio of the peaks of ^{208}Pb and ^{208}Tl indicates the cleanliness of the buffer gas. The second ionization potential of lead is very close to the ionization potential of N_2 (see Section 4.2). Therefore, the charge state of lead ions extracted out of the CSC is very sensitive to the amount of contaminants in the helium buffer gas. From the decay branching ratios of ^{212}Bi, ^{208}Pb should be populated in the amounts approximately twice as high as ^{208}Tl. By measuring the abundance ratio of singly-charged ^{208}Pb and ^{208}Tl (^{208}Tl is extracted only as singly-charged ions), it is possible to deduce the ratio of singly- and doubly-charged ^{208}Pb ions. An increased fraction of singly-charged lead ions indicates a higher contamination of the CSC.

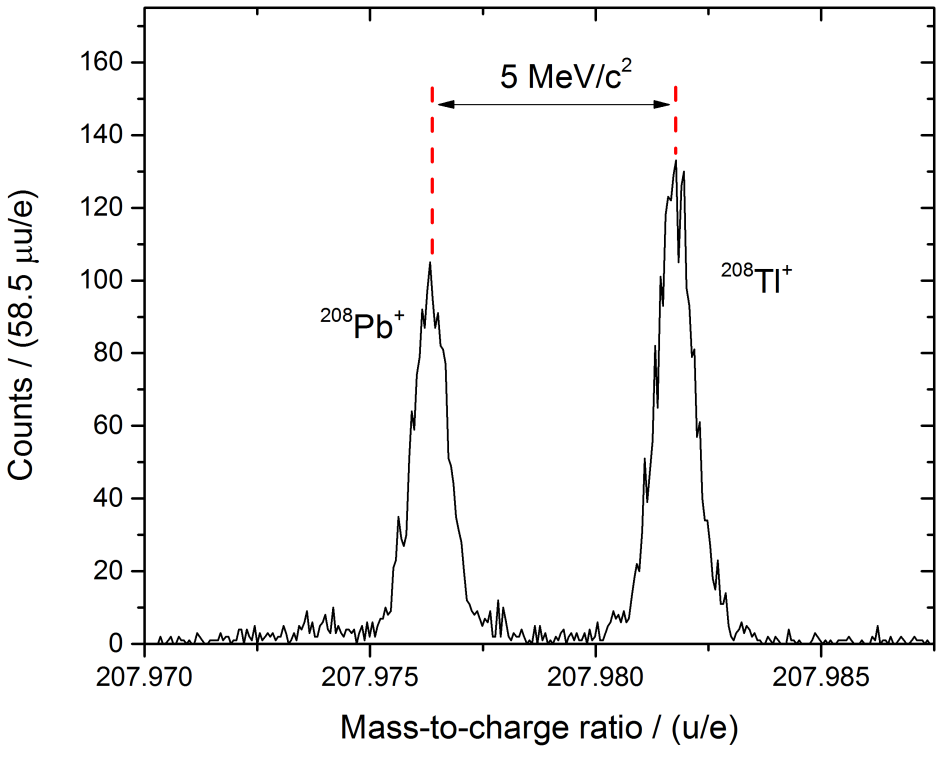

Figure 3.3: Measured mass spectrum of two isobaric nuclei ^{208}Po and ^{208}Tl produced by ^{228}Th source. The mass difference of the isobars corresponds to 5 MeV. The measurement was done with 256 isochronous turns in the MR-TOF-MS at a mass resolving power of $\sim 200,000$.

3.2 Discharge source

Another internal ion source installed in the CSC is the discharge source. It was designed in [Greiner, 2013a] and has been characterized and used for cleanliness investigations of the CSC in the frames of this work. The discharge source is mounted on one of the DC cage rings at a distance of about 30 cm away from the RF carpet. The construction of the source is shown in Fig. 3.4. It consists of a holding structure made out of insulating PEEK (polyetheretherketone) material and two metal electrodes – a needle and a plate. The tip of the needle electrode is positioned ~ 0.5 mm away from the plate electrode. This configuration and positioning is chosen in order to maximize the electric field between the electrodes. When a voltage difference of a few hundreds of volts is applied to the electrodes, an electric discharge is ignited. The discharge ionizes atoms of the buffer gas and of the contaminants contained in the buffer gas. The produced ions can then be extracted out of the CSC with electric fields and measured by the downstream detectors. The amount of ionization can be regulated by changing the voltage difference between the electrodes.

Figure 3.5 shows the mass spectrum of the ions produced by the discharge source and extracted out of the CSC. The measurement was done by doing a scan with the extraction RFQ operated as a mass filter [Miskun, 2015] and detecting the ions with the channeltron detector installed in the RFQ beamline behind the extraction RFQ. The mass filter was operated with a resolving power of ~ 10. Only the ions in the set mass window were transmitted and detected. The window was moved over the broad mass range resulting in the plotted spectrum. The broad peak in the high mass region at around 200 u/e corresponds to the unresolved products of ^{223}Ra radioactive source. The abundant peaks at lower masses are the ionized contaminants.

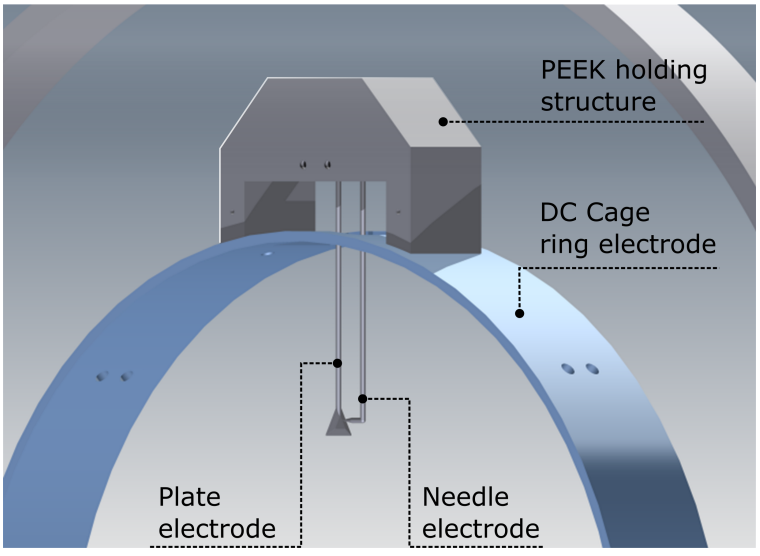

Figure 3.4: CAD drawing of the discharge source mounted on the DC cage ring. The source consists of the PEEK holding structure and two metal electrodes – a needle and a plate. The ignited discharge ionizes the buffer gas and the contaminants atoms. Picture modified from [Rink, 2017].

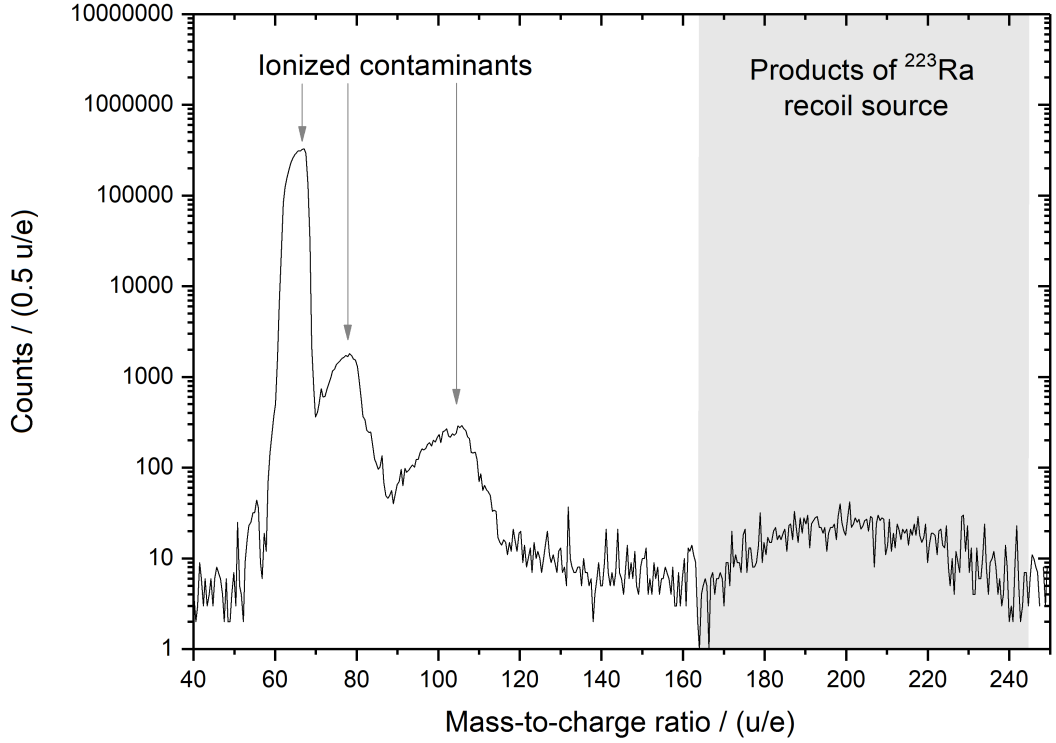

Figure 3.5: Measured mass spectrum of the ions produced by the discharge source plotted in logarithmic scale [Miskun, 2015]. The measurement was done with the extraction RFQ operated as a mass filter with the resolving power of ~ 10 and the channeltron detector. Peaks on the left side of the spectrum are the ionized contaminants contained in the helium buffer gas; the broad peak on the right side corresponds to unresolved products of ^{223}Ra source. Total measurement time was 7 minutes.

As shown in Figure 3.5, the discharge source can be used for investigations of the buffer gas cleanliness, one of the most crucial characteristics of the CSC. It produces a huge, but controllable ionization. Therefore, it also allows studies of the stopping cell operation under space charge effects. Besides, the ions produced by the discharge source cover a large mass range and can be used for mass-dependent transport investigations. However, the polyatomic ions are not ideal for a pilot beam because of possible fragmentation in the RFQ beamline.

The application of the discharge source was demonstrated during the beam time in 2016. The mass spectra of ions produced in the CSC were investigated. In one measurement, the ionization was induced by the ^{124}Xe primary beam passing through the CSC. In another measurement, the buffer gas and its contaminants were ionized by the discharge source. The mass spectra measured with the MR-TOF-MS are shown in Fig. 3.6. The measurements were done with the TFS mode of the MR-TOF-MS [Dickel et al., 2015b], as the goal was not to identify each measured mass line, but rather to compare the ionization patterns. As can be seen from the results, the

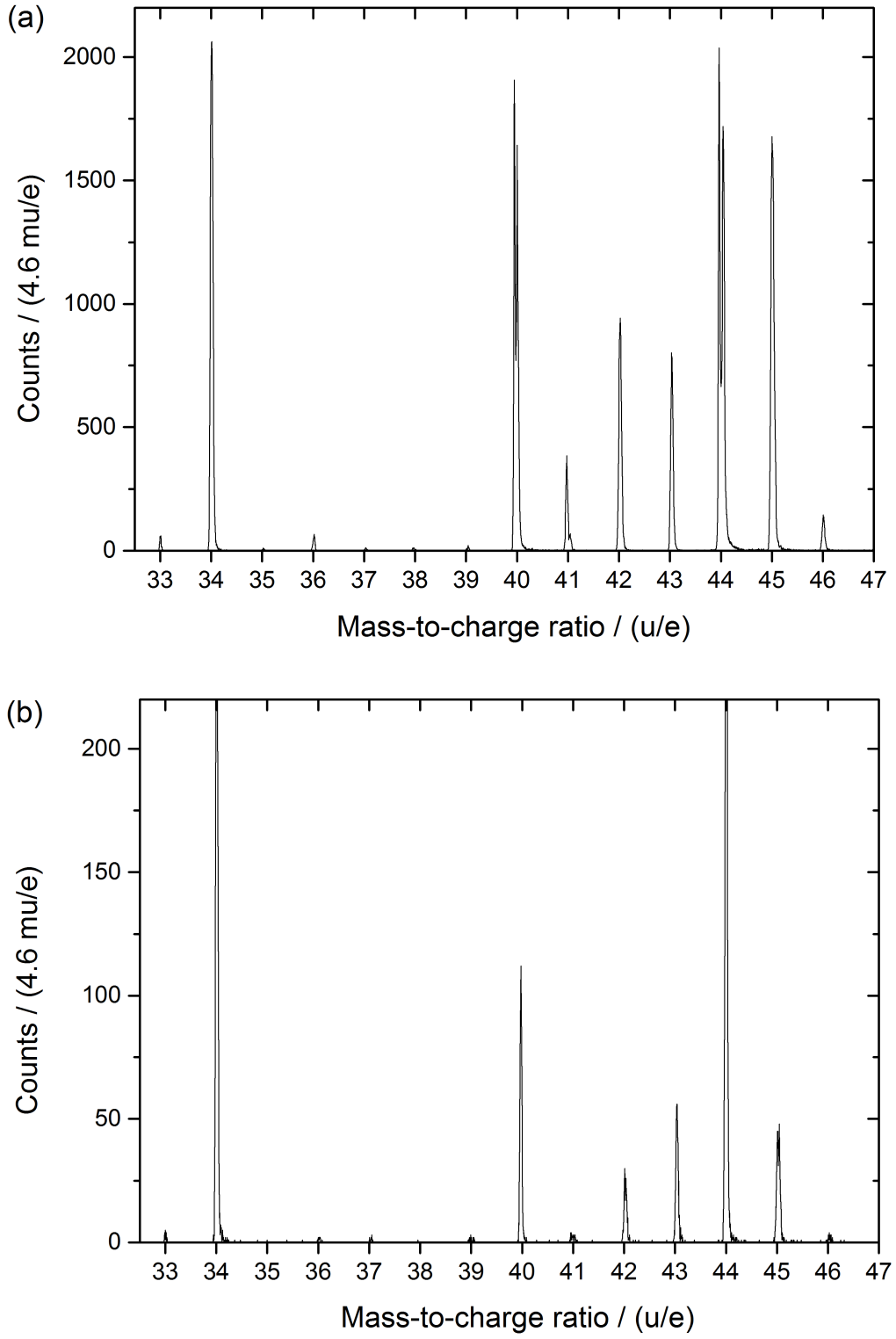

Figure 3.6: Measured mass spectra of ions extracted from the CSC produced as the result of ionization a) by ^{124}Xe primary beam passing through the CSC; b) by the discharge source inside the CSC. Ionization patterns in both cases are similar. The measurement was done with the MR-TOF-MS in TFS mode (no reflections in the analyzer) at a mass resolving power of ~ 1000, which does not enable unambiguous particle identification.

ionization patterns produced by the discharge source and by the primary beam hitting the CSC look very similar. The relative abundances of the peaks are not absolutely the same, as the measurement times, the ion rates, and the corresponding dead-time effects of the data acquisition system were different. Nevertheless, the ions of the same masses are produced in both cases. This fact is of great importance, as it gives a possibility to use the discharge source for the preparation of the system for the measurement of the ion of interest under beam-like conditions. The ion transport can be set up such that the transmission efficiency for the ion of interest is optimal but all harmful contaminants are strongly suppressed or removed from the spectrum. This experiment preparation can be done off-line, which also leads to more efficient use of expensive and limited beam time.

3.3 High-density operation of the CSC

As it was already mentioned in the paragraph "Challenges and solutions" of Subsection 2.2.1, the total efficiency of stopping cells is given by the product of the stopping efficiency and the ion survival and extraction efficiency. Advances in the cleanliness of the CSC resulted in an ion survival and extraction efficiency value of 50-100 % [Reiter, 2015]. The stopping efficiency, on the other hand, is a bottleneck to the better performance of the setup. Exotic nuclei produced at relativistic energies of 1 GeV/u have a very broad range distribution at the final focal plane. Therefore, a higher density of the buffer gas inside the CSC is required in order to maximize the stopping efficiency.

However, a high-density operation of the CSC is a very challenging task. The buffer gas density is limited by the allowable pressures in the downstream beamline. One technical limitation comes from the pressure range of the operation of the turbomolecular pumps. If the gas pressure in the RFQ beamline or in the prevacuum lines is too high, the turbomolecular pumps loose pumping efficiency, overheat and switch off. Another limitation is the gas pressure in the analyzer of the MR-TOF-MS. High pressures in the analyzer may cause ion transmission losses in the MR-TOF-MS.

In Figure 3.7, the improvement of the differential pumping of the CSC over time is shown. Measured values of the gas pressure in the RFQ beamline for different areal densities of the helium buffer gas in the CSC are plotted. During the measurements, no electric fields were applied inside of the CSC. In 2012, the RFQ beamline was pumped by two Agilent Turbo-V 1001 Navigator turbomolecular pumps with an overall pumping speed of $\sim$ 1800 l/s for helium. In 2014, the vacuum system was upgraded with two Oerlikon Leybold TURBOVAC MAG 1700 turbomolecular pumps, which together with one Agilent Turbo-V 1001 Navigator provided $\sim$ 3900 l/s pumping speed. As can be seen from the plot, this upgrade significantly improved the differential pumping of the system. Higher areal densities of the buffer gas inside the CSC for the same pressures in the RFQ beamline became available.

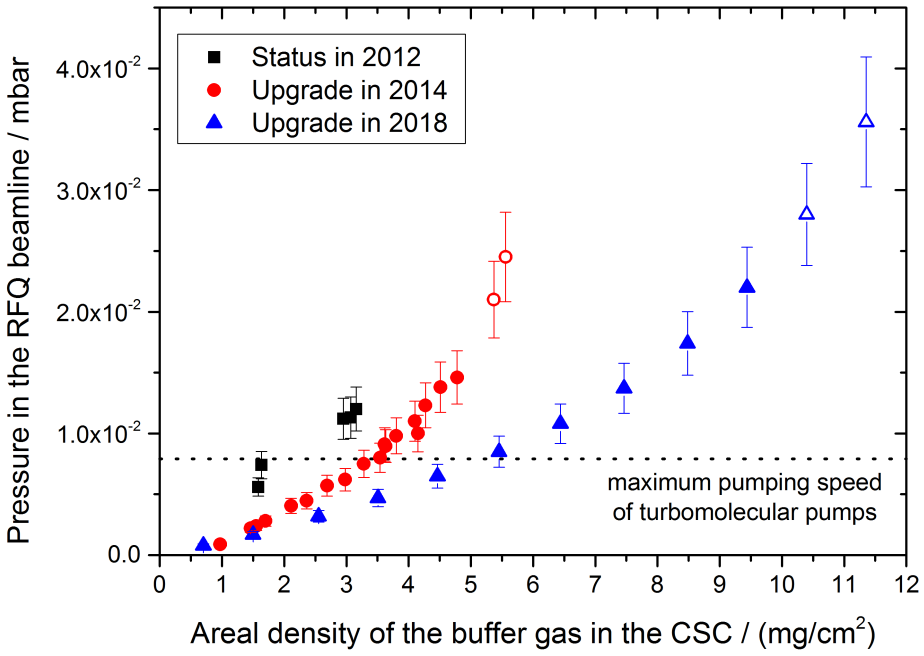

Figure 3.7: Improvement of the differential pumping of the CSC over the years. Pressure in the RFQ beamline was measured for different areal densities of the helium buffer gas inside the CSC. The slope changes at a pressure of $\sim 8 \cdot 10^{-3}$ mbar due to the reduced efficiency of the turbomolecular pumps and when the pressure in the prevacuum lines is too high for their normal operation (measurement points depicted in open symbols). After the last upgrade, safe and long-term operation of the system with areal densities of up to 10 mg/cm^2 was demonstrated.

At 3.5 mg/cm^2, the slope of characteristic curve changes due to the reduced efficiency of the turbomolecular pumps for the pressures above $\sim 8 \cdot 10^{-3}$ mbar. The last two points were measured on the edge of system performance, with the prevacuum pressure too high for long-term operation of the turbomolecular pumps. The areal density of 3.5 mg/cm^2 was chosen to be standard for long-term operation and the densities of up to 6.2 mg/cm^2 could be used for short-term measurements [Reiter, 2015]. In 2018, the system was upgraded further. A third Oerlikon Leybold TURBOVAC MAG 1700 pump was installed instead of the Agilent Turbo-V 1001 Navigator, and a new multi-stage dry vacuum pump (EBARA EV-S100) was installed in the prevacuum line. The total pumping speed of all turbomolecular pumps resulted in $\sim$ 4500 l/s, whereas the pumping speed of the prevacuum lines was increased by almost a factor of five (from 130 m^3/h to 600 m^3/h). In addition, the RFQ beamline was extended by the second diagnostics unit (DU2) [Hornung, 2018], which introduced an additional differential pumping stage between the CSC and the MR-TOF-MS. This helped to further separate the high-density environment of the CSC and the low-pressure region of the MR-TOF-MS analyzer. Thus, even higher pressures of the buffer gas inside the CSC became possible. The stopping volume of the CSC was shortened by two DC cage rings in order to allow for higher DC push fields. This reduced the areal

density by ~ 6 %. The characteristic curve for the measurements done in 2018 has the same shape as in 2014. First, the slope changes at a pressure in the RFQ beamline of $\sim 8 \cdot 10^{-3}$ mbar. Second, the slope changes again when the pressure in the prevacuum lines is too high for the proper operation of the turbomolecular pumps. The safe long-term system operation with areal densities of up to $\sim$ 10 mg/cm^2 (150 mbar of helium gas at 75 K) was demonstrated. This is an unprecedented areal density value, which is at least a factor of five higher than for any other cryogenic stopping cell with RF structure used for the thermalization of relativistic ions in the world. It is important to mention that even for 10 mg/cm^2 of helium gas inside the CSC, the pressure in the analyzer of the MR-TOF-MS was below the level of $5 \cdot 10^{-8}$ mbar.

Apart from the limitations given by the differential pumping, the densities of the buffer gas can be limited by the RF carpet performance. As indicated by Eq. (1.19), the effective repelling field of the RF carpet is inversely proportional to the areal density of the buffer gas. Therefore, it was crucial to investigate the extraction efficiency of the CSC at high areal densities. Such tests were done with the ions produced by the ^{228}Th source. For different values of the helium buffer gas areal density inside the CSC, the RF voltage was scanned, and the count rate of ^{228}Th products was measured by the silicon detector in the DU1. For the count rate measurement, the peak corresponding to the ^{216}Po alpha decay was used. Ions of ^{220}Rn also contributed to the measured count rate, because the measurement time was long enough for them to decay into ^{216}Po and undergo another alpha decay. To minimize the influence of this effect, the same measurement time was used for all measurement points. After each measurement, the ion transmission to the silicon detector was blocked for a few minutes in order to clean the detector from most of the accumulated ^{220}Rn and ^{216}Po nuclei. The DC push field was scaled for each value of the areal density such that the mean extraction time was kept the same ($\sim$ 55 ms). These field strengths were a factor of two lower than the ones that are typically used because of a temporal technical problem.

The results of these investigations are shown in Fig. 3.8. The relative extraction efficiency of the CSC is plotted as a function of the RF carpet voltage for four different areal density values. All data points were normalized to the highest measured count rate, corresponding to the measurement at an areal density of 3.5 mg/cm^2 and 62 $V_{peak-peak}$ applied to the RF carpet. At low voltages, the effective RF repelling field is not strong enough to compensate the DC push field. Therefore, the ions are lost on the electrodes of the RF carpet. With increasing RF voltage, the effective repelling field becomes stronger, and, at a certain value, the onset of ion extraction appears. Once the full extraction efficiency is reached, it stays on a plateau for all higher RF voltages. The high amplitudes of the RF voltage were reached by stacking two amplifiers. The obtained results show that, even for an areal density of 9.6 mg/cm^2, the maximum extraction efficiency is reached for heavy ions with $m/q \sim 220$ u/e and a DC push field corresponding to a mean extraction time of $\sim$ 55 ms. From the thermal limitations, maximum RF voltages of $\sim$ 180 $V_{peak-peak}$ could be applied to the RF carpet. It is evident that this operation regime is already close to the technical limits of the device. In order to reach the maximum extraction efficiency for ions of lower masses at the same areal density of the buffer gas, the DC push field has to be lowered

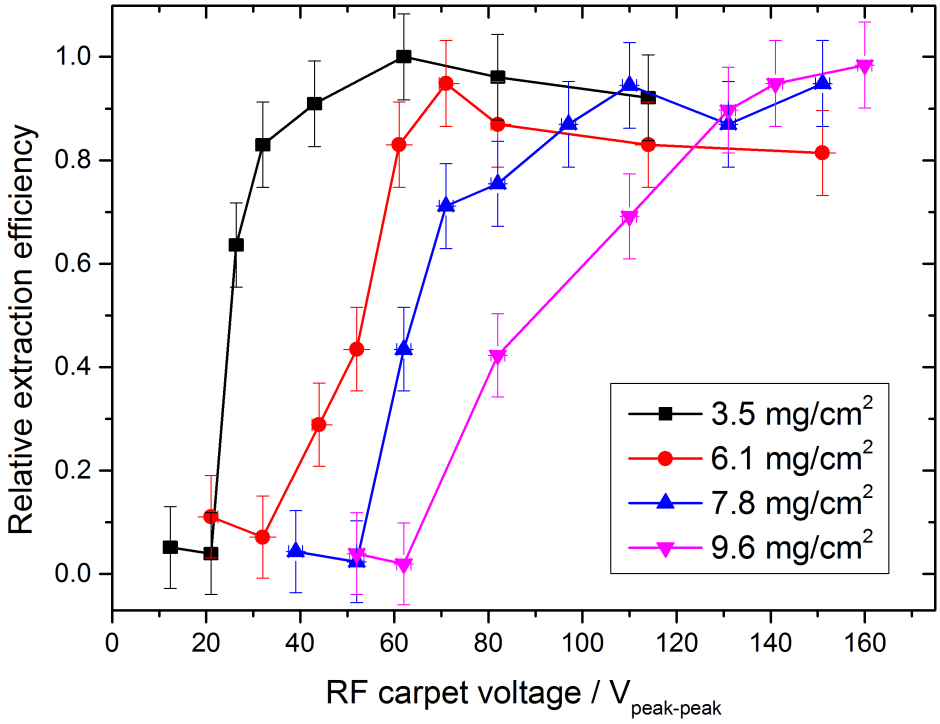

Figure 3.8: Measured relative extraction efficiency of the CSC as a function of the RF carpet voltage for different values of the buffer gas areal density. The measurement was done with a silicon surface barrier detector installed in the RFQ beamline. For the determination of the efficiency, the measured count rates of the $^{216}Po^{+}$ and $^{220}Rn^{+}$ ions were used. Normalization of all data points is done to the highest measured count rate corresponding to the measurement at an areal density of 3.7 mg/cm^2 and 62 $V_{peak-peak}$ applied to the RF carpet. Even for an areal density of $\sim$ 10 mg/cm^2, the maximum extraction efficiency is reached.

further. In the same way, faster extraction at these conditions is only possible with heavier ions. The interplay of these parameters is defined by Eq. (1.19).

The shortest possible extraction time of ions out of the high-density CSC was determined by measuring the maximum possible DC push field strength. The strength of the DC push field is limited by the electrical discharges occurring inside the inner chamber of the CSC. It is very important to mention that the areal density values used for the CSC operation correspond to the rising part of the Paschen curve [Paschen, 1889]. The Paschen curve represents the dependency of a breakdown voltage between two electrodes positioned in gas on the product of the distance between the electrodes and the density of the gas. At higher values of the density-distance product, the breakdown voltage is almost proportional to the pressure of the buffer gas, as the temperature and the distance between the closest electrodes are kept the same. This gives an important advantage because, for the higher densities of the buffer gas inside the CSC, a higher DC push fields can be applied. As it was shown in previous investigations, this effect results in a constant extraction time, which is not dependent on

the areal density of the buffer gas [Reiter, 2015]. For the high-density operation of the CSC, the maximum possible DC push field strengths were measured. At a helium areal density of 10 mg/cm^2, DC push fields of $\sim$ 50 V/cm could be applied. From ion mobility calculations, this field strength corresponds to a mean extraction time of $\sim$ 30 ms for most singly- or doubly-charged atomic ions [Viehland, 2012], which is in good agreement with previous results [Purushothaman et al., 2013, Reiter, 2015].

3.4 Enhanced selectivity of ion transport

In the implementation of the CSC, many different technological steps were taken to provide high cleanliness of the buffer gas. Yet, some contaminants are still present in the system. Some are desorbed from the surface of the inner chamber when the ion beam passes through, some are introduced with the helium buffer gas itself. Mostly, the latter are the noble gases, which do not harm ion survival. During the slow-down and extraction processes, incoming ions do multiple collisions with atoms of the buffer gas and ionize them. Contaminant atoms contained in the buffer gas can be also ionized in charge-exchange reactions and extracted out of the CSC together with the ions of interest. At cryogenic temperatures, the ionized contaminants can form adducts with mass-to-charge ratios over a very broad range. Some of them might have a mass-to-charge ratio very similar to the one of the IOI and might spoil high-accuracy mass measurement. Therefore, special techniques had to be developed in order to remove the contaminants selectively. They are described in the following subsections.

3.4.1 Isolation-dissociation-isolation method

One of the very effective tools for removal of molecular contaminants is collision-induced dissociation (CID) [McLuckey, 1992, Schury et al., 2006]. During the CID process, the molecules are excited in multiple collisions with the buffer gas atoms. This excitation can lead to their break-up into two or more lighter fragments. At the FRS-IC, CID can be performed in the gas-filled RFQs of the DU1, which are operated at $1 \cdot 10^{-2}$ mbar of helium. Under normal conditions, the ions are transported through the RFQ beamline with a kinetic energy of a few electronvolts. In order to increase the collisional energy transfer and to enhance the dissociation of contaminant molecules, the kinetic energy of the ions can be increased to a few tens of electronvolts by applying a higher DC gradient along the RFQ rods or a higher DC voltage step between the RFQ segments. This can be efficiently used to remove the unwanted molecular contaminants from the mass-to-charge range of interest. However, heavier molecules can be also fragmented, and their fragments might overlap with the IOI. In this way, the molecular contamination in the mass range of interest is changed, but not removed.

To solve this problem, isolation of the mass-to-charge range of interest can be done prior to the dissociation. In this case, there are no heavier molecules, which can possibly result in new contamination. Lighter fragments that are produced by CID can be removed from the spectrum with another isolation step. The consecutive steps of isolation, dissociation, and isolation for the removal of molecular contaminants are referred to as the isolation-dissociation-isolation (IDI) method [Greiner, 2017, Greiner et al., 2019]. The concept of this method is shown schematically in Fig. 3.9.

At the FRS Ion Catcher, the first isolation step is performed with the extraction RFQ operated as a mass filter [Miskun et al., 2015]. The normalized transmission efficiency of the mass filter plotted as a function of its resolving power is shown in Fig. 3.10. With increasing mass resolving power, the transmission efficiency drops. Despite the high buffer gas pressure of operation and low mechanical accuracy of the extraction RFQ, resolving powers of up to 150 can be reached. Depending on the experimental goals and conditions, the optimal combination of mass resolving power and transmission efficiency can be chosen. For the IDI method, the mass filter is operated with a resolving power of about 10, which allows isolation of the mass-to-charge region of interest without significant transmission losses.

The second isolation step is done by the first RFQ of the MR-TOF-MS. The RFQ is operated at an increased RF voltage amplitude, resulting in instability of motion for all ions with a mass-to-charge ratio lower than a certain value (the low-mass cut-off). This threshold corresponds to the Mathieu stability parameter q_u of 0.908 (see Subsection 1.3.3). The RF voltage amplitude is set such that the IOI are transported by the RFQ, but lighter molecules produced by CID are filtered out.

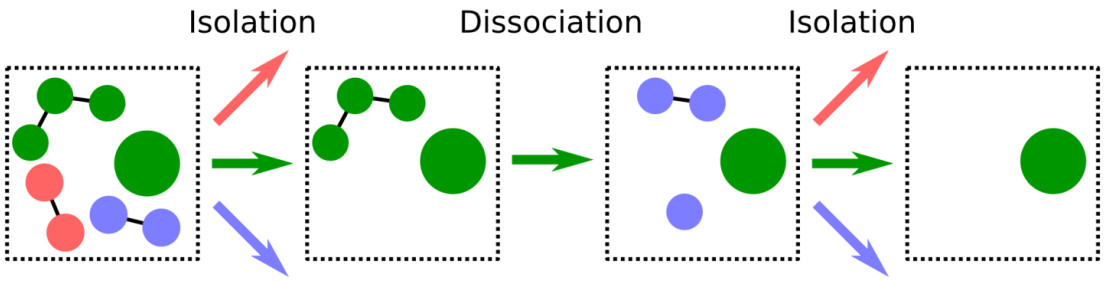

Figure 3.9: Molecular contamination removal by the IDI (isolation-dissociation-isolation) method [Greiner et al., 2019]. Colors indicate the mass-to-charge ratio of ions: green – mass-to-charge ratio of the ion of interest; blue – lower mass-to-charge ratio; red – higher mass-to-charge ratio. During the first isolation step, ions of lower and higher mass-to-charge ratios are removed. Remaining molecular contaminants are fragmented by dissociation. During the second isolation step, produced in dissociation fragments are removed.

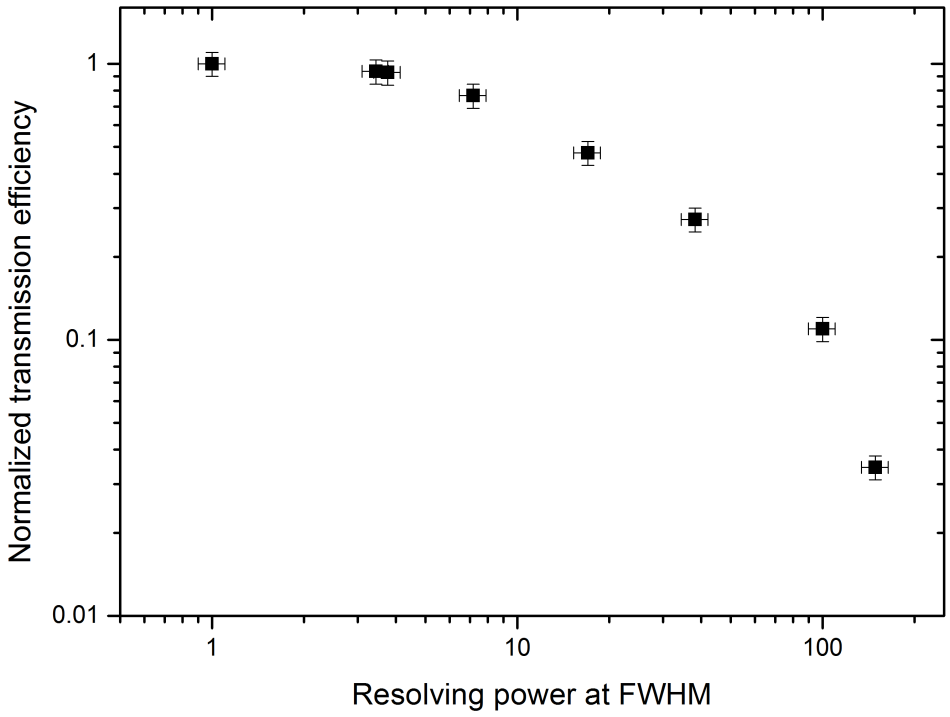

Figure 3.10: Normalized measured transmission efficiency of the extraction RFQ operated as a mass filter plotted as a function of its resolving power [Miskun et al., 2015]. The measurement was done for a buffer gas areal density in the CSC of 4 mg/cm^2 and a residual gas pressure of $8.4 \cdot 10^{-3}$ mbar in the RFQ beamline.

The IDI method was implemented and first tested with the internal ^{228}Th recoil source. Results of these investigations are shown in Fig. 3.11. In the high mass-to-charge region (190-240 u/e), singly-charged decay products of ^{228}Th are extracted together with molecular contaminant ions and measured with the MR-TOF-MS in TFS mode. The top panel of Fig. 3.11 shows the mass spectrum of extracted ions. The contaminant ions are generated from the surface of the ^{228}Th source and are not observed when the source is switched off. To remove the molecular contamination, CID was done in the RFQ beamline by introducing a 60 V step between the RFQs of the diagnostics unit. The resulting mass spectrum is shown in the middle panel of Fig. 3.11. As can be seen from the spectrum, the mass lines around 230 u/e disappeared, but new mass lines in the lower mass-to-charge region were introduced. The break-up of heavy molecules by CID resulted in the production of lighter fragments, some of which appeared in the region of the IOI. Therefore, as discussed above, it is not sufficient to use only CID to remove the molecular contamination. However, by introducing isolation steps before and after CID, it was possible to obtain a contaminant-free mass spectrum of the ^{228}Th products (the bottom panel of Fig. 3.11). For the first isolation step, the mass filter was operated with $U/V = 0.12$ (mass resolving power $m/\Delta m \sim 10$), where U is the DC and V is the AC amplitude of the quadrupolar field.

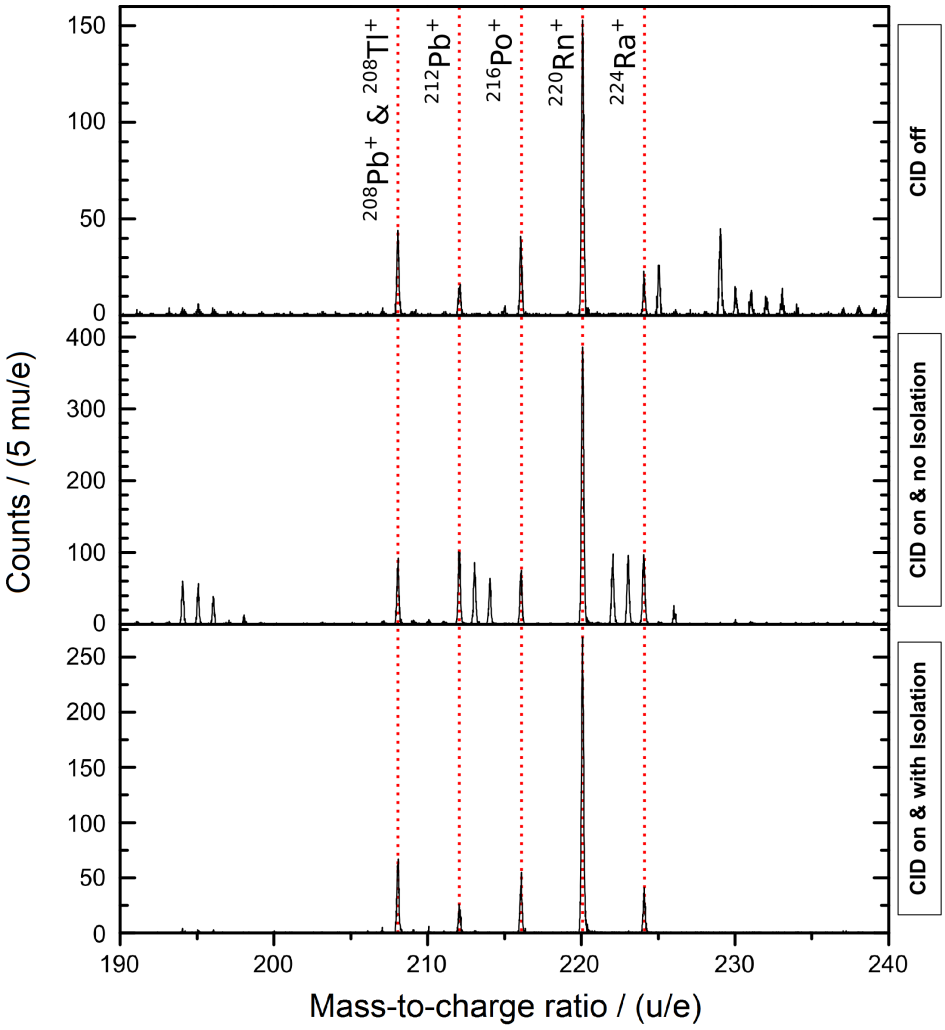

Figure 3.11: Mass spectra of the ions produced by the ^{228}Th recoil source measured with the MR-TOF-MS in TFS mode [Greiner et al., 2019]. Apart from the singly-charged products of ^{228}Th, molecular contaminants are extracted and detected. Top panel: the IDI method is not applied. Middle panel: CID is applied; heavy contaminant molecules break up introducing lighter fragments to the spectrum. Bottom panel: the IDI method is applied; all molecular contaminants are removed from the spectrum.

Once proven to be a very powerful technique for the contamination suppression, the IDI method was also used in experiments with relativistic ions. An example is shown in Fig. 3.12. ^{124}Xe primary beam with an energy of 600 MeV/u was slowed down and thermalized in the CSC. $^{124}Xe^+$ ions were extracted together with ionized adducts and measured in the MR-TOF-MS. The top panel of Fig. 3.12 shows the measured time-of-flight spectrum for no IDI applied. The spectrum is dominated by adducts of krypton, which is contained in the helium buffer gas in trace amounts. One of these adducts, $^{80}Kr^{12}C^{16}O_2{}^+$, has only a mass-to-charge difference of 300 keV/(c^2e) to $^{124}Xe^+$. To fully separate the IOI and the contaminant adduct (baseline separation), a mass resolving power of more than one million is necessary. In this measurement, the MR-TOF-MS was operated with a resolving power of $\sim 150,000$. When applying IDI,

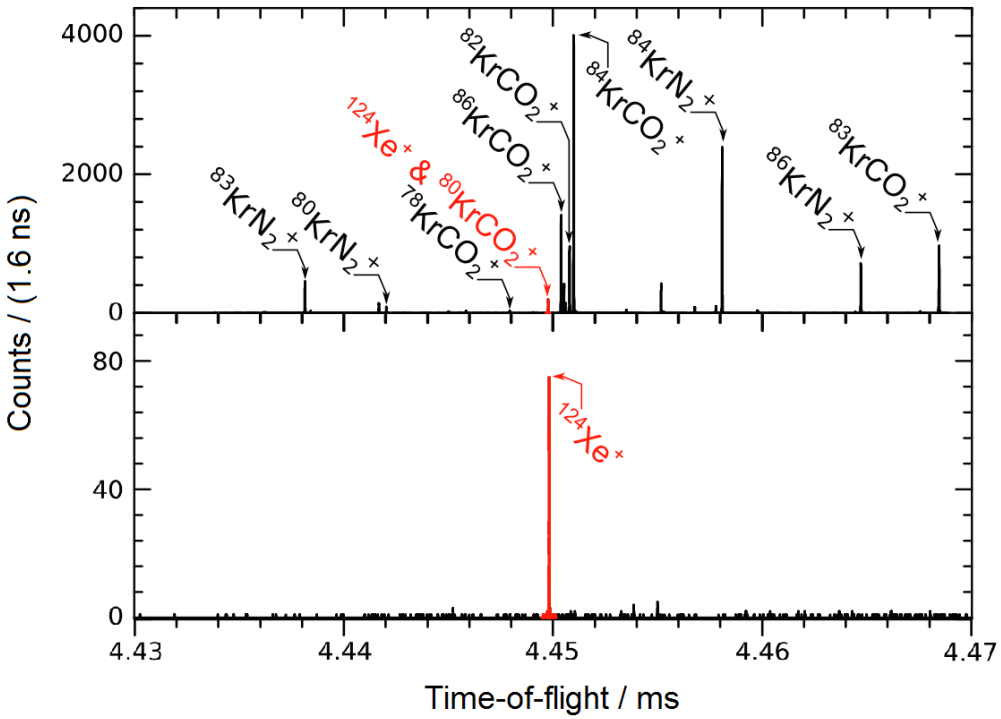

Figure 3.12: Time-of-flight spectra of the ions extracted out of the CSC during the experiment with ^{124}Xe primary beam measured with the MR-TOF-MS [Greiner et al., 2019]. Resolving power is $\sim 150,000$. Ions from different mass numbers appear in the time-of-flight spectrum, because they do different number of turns in the MR-TOF-MS. Top panel: IDI is not applied; the spectrum is dominated by the molecular contaminants; $^{124}Xe^+$ (red) is not resolved in the spectrum because of the abundant overlapping peak of $^{80}Kr^{12}C^{16}O_2{}^+$. Bottom panel: IDI is applied; the measurement time is four times longer; the molecular contaminants are suppressed by more than four orders of magnitude.

most of the molecular contaminants were removed from the spectrum, as can be seen in the bottom panel of Fig. 3.12. The overlapping adduct were no longer present and $^{124}Xe^+$ ions could be clearly identified. The measurement time for this spectrum is four times longer than that for the spectrum in the top panel. For the most abundant contaminant peak, a suppression by more than four orders of magnitude is reached, whereas the transmission efficiency for the IOI was measured to be unchanged.

The IDI method is universal and can be adapted at other facilities, where the issue of molecular contamination exists. Isolation steps can be done with different techniques and equipment, e.g. dipole magnets [Moore et al., 2010] and RF mass filters [Haettner et al., 2018] for DC beams and a Bradbury-Nielsen gate [Brunner et al., 2012] for pulsed beams of ions. At the FRS-IC, IDI is currently used as a standard tool for the molecular background suppression. For future experiments, it is planned to improve this method by adding an additional CID step in the extension of the RFQ beamline [Hornung et al., 2018]. This will allow the ion transport with yet higher kinetic energies in order to increase the suppression of strongly-bound molecules.

3.4.2 Separation by ion mobility at the RF carpet

The effective repelling field E_{eff} of the RF carpet depends on different parameters, as described by Eq. (1.19). One of these parameters is the ion mass m. This makes the RF carpet operation mass-selective. For the ions with masses lower than the certain threshold value, which is defined by other parameters from the equation, the effective repelling field is not strong enough to compensate the DC push field. These ions are not repelled by the RF carpet and are lost on the electrodes. It is of great importance as it helps to prevent the extraction of low-mass ionization products (above all, He_3^+ trimers) out of the CSC. The effective repelling field also depends on the ion mobility K. A new selection technique utilizing this dependence for the suppression of molecular background in the mass region of the IOI has been developed at the FRS-IC. This technique is based on the separation of the IOI and the molecular contaminants by ion mobility with the RF carpet. The fact that the contaminant ions are filtered out already in the CSC is an important advantage of this technique because it helps to avoid space charge effects at the RF carpet and in the RFQ beamline.

Separation by ion mobility at the RF carpet works in the following way. Atomic positively-charged ions over a broad mass-to-charge range have a reduced mobility in helium gas of about 17.5 $\text{cm}^2/(\text{Vs})$ [Viehland, 2012]. Molecules and adducts have lower mobility value, due to their larger size. This means that, according to Eq. (1.19), for the same operating conditions, the molecular ions feel a weaker effective repelling field than the atomic ions. Thus, with the correct setting of the RF carpet operation, it is possible to find a regime, where the atomic ions are repelled and extracted out of the CSC, and the molecular ions are lost on the electrodes of the RF carpet.

From Equation (1.19), it is possible to deduce the dependence of the relative change in the effective repelling field of the RF carpet $\Delta E_{\text{eff}}/E_{\text{eff}}$ on relative changes in the mass and the mobility of the ion:

$$\frac{\Delta E_{\text{eff}}}{E_{\text{eff}}} = \frac{\Delta m}{m} + \frac{2\Delta K}{K}, \tag{3.1}$$

where K is defined by Eq. (1.14). As can be seen from this equation, the effective repelling field is more sensitive to the change in the ion mobility, which allows molecular suppression without losses for atomic ions of the same mass. Therefore, the separation by ion mobility at the RF carpet can be also used to remove strongly-bound molecules and adducts overlapping with the IOI that cannot be dissociated in the RFQ beamline in collisions with buffer gas atoms.

This method was investigated during the experiments at GSI in 2016. The ^{124}Xe primary beam passed through the CSC and produced ionization of the buffer gas and its contaminants. Extracted ionization products were measured with the MR-TOF-MS in TFS mode at a mass resolving power of ~ 1000. Results are shown in Fig. 3.13. In all measurements, the mass filter transmitted the mass-to-charge window from 70 u/e to 95 u/e. The rate of the incoming ion beam was $\sim 5,000$ ions/s. In Figure 3.13a, the measured mass-to-charge spectrum of ionization products is shown. IDI was not

applied, the RF carpet was operated at 5.92 MHz and 68 $V_{peak-peak}$. Most of the peaks in the spectrum correspond to the ionized stable isotopes of krypton, which was introduced to the CSC together with the helium buffer gas. It is important to note that because of the high rate the data acquisition of the MR-TOF-MS had strong dead-time effects and the relative abundances of the krypton isotopes do not correspond to the literature values completely. In addition, the measurement time for all spectra was different, therefore, in order to simplify visual comparison, measured counts in each spectrum were normalized to the same peak height of the ^{83}Kr isotope, the well-identified peak of the stable isotopes with least dead-time effect. As can be seen from the spectrum, one isotope of krypton, ^{80}Kr, overlaps with a close-lying high-abundant contaminant, which hinders its proper identification. Besides molecules at the mass-to-charge lines of 80 u/e and 81 u/e, there is no significant molecular background over a broad range of 25 u/e. This result demonstrates the good cleanliness of the CSC.

As the next step, IDI was applied to remove the contaminant molecules. The resulting mass spectrum is shown in Fig. 3.13b. The 81 u/e peak has disappeared, but the contaminant at mass-to-charge 80 u/e is still present in the spectrum. IDI was not enough to break it up and remove it from the spectrum. Then, the RF voltage of the RF carpet was lowered from 68 $V_{peak-peak}$ to 48 $V_{peak-peak}$, which brought no difference and resulted in an identical spectrum (Fig. 3.13c). Afterwards, the RF voltage was further decreased down to 42 $V_{peak-peak}$. The spectrum for this setting is shown in Fig. 3.13d. The molecular contaminant at the mass line 80 u/e was removed leaving the ^{80}Kr isotope peak. This threshold behavior corresponds to the RF carpet operation regime when the effective repelling field is strong enough to repel the atomic ions, but not the molecular ones with lower ion mobility. The transition from the full transmission of the molecular contaminant to its full suppression is rather sharp for a small change in the RF voltage. This indicates that the separation by ion mobility is a very well-defined suppression method.

Further decrease of the repelling RF voltage to 36 $V_{peak-peak}$ lead to the suppression of ^{78}Kr and ^{80}Kr isotopes peaks, as shown in Fig. 3.13e. This effect occurs due to the mass dependence of the effective repelling field of the RF carpet. The ions of lower masses feel a weaker effective repelling field. At this value of the RF voltage, the effective repelling field was not enough to compensate the DC push field for krypton isotopes of lower masses.

In Figure 3.14, the spectra for 68 $V_{peak-peak}$ and 42 $V_{peak-peak}$ of the RF carpet repelling voltage (Fig. 3.13b and Fig. 3.13d) are shown again in logarithmic scale without normalization. The logarithmic scale reveals also low-abundant molecular contaminants, which could not be seen in the linear scale. From these spectra, it can be clearly seen that the separation by ion mobility at the RF carpet works over a very broad mass-to-charge range. Both very abundant and low-abundant molecular contaminants are essentially completely removed from the spectrum. Therefore, this technique can be used as a standard and very powerful tool for the molecular background suppression already at the stage of ions extraction out of the CSC. In addition, neutralization of molecular ions at the RF carpet surface significantly reduces the space charge effects at the extraction nozzle and in the RFQ beamline.

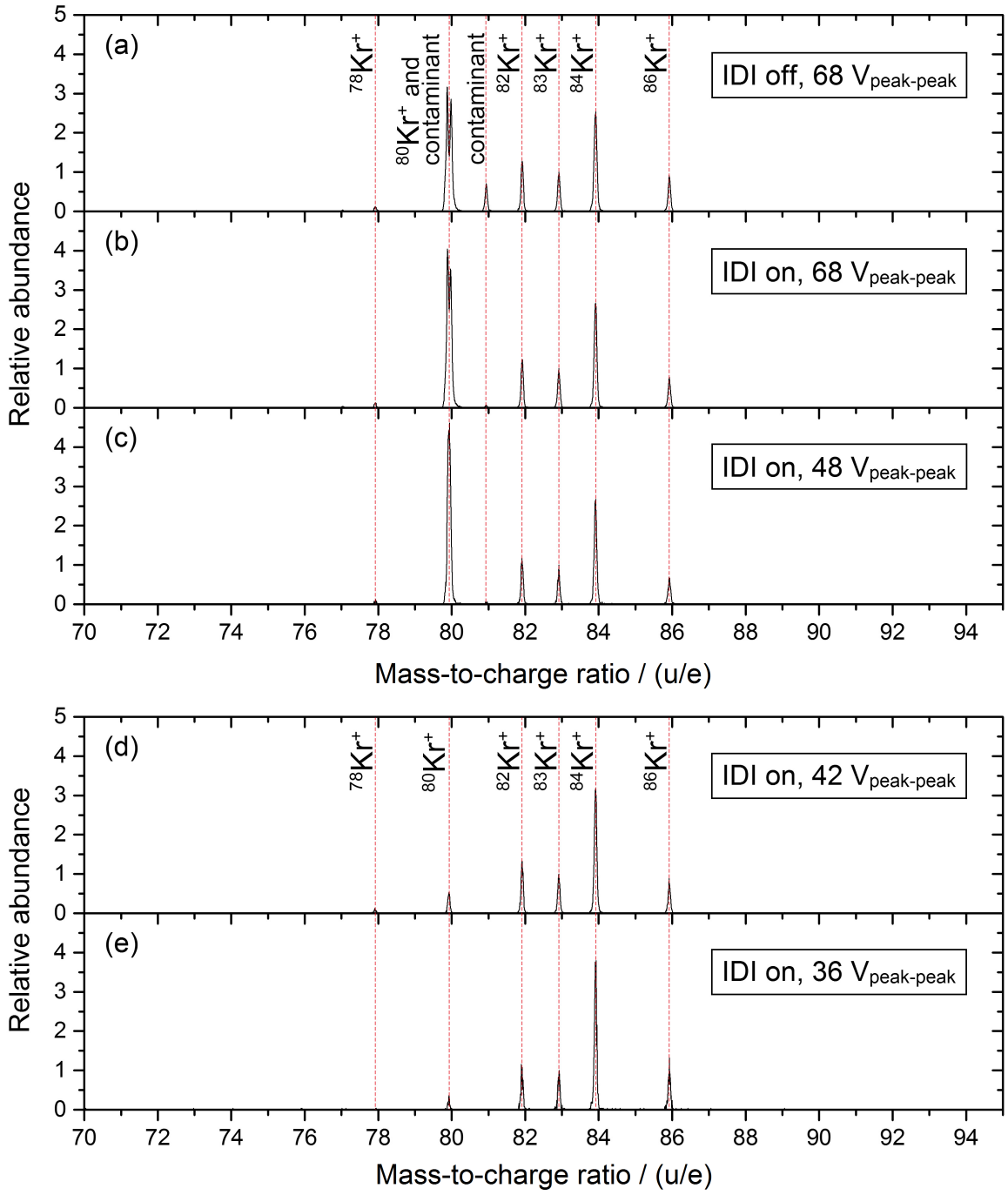

Figure 3.13: Mass spectra of ionization products extracted out of the CSC measured with the MR-TOF-MS in TFS mode at a mass resolving power of ~ 1000. Stable isotopes of krypton and molecular contaminants are present. All spectra are normalized to the same height of ^{83}Kr peak. a) IDI is not applied, RF carpet at 68 $V_{peak-peak}$, molecular contaminants at 80 u/e and 81 u/e; b) IDI is applied, RF carpet at 68 $V_{peak-peak}$, contaminant at 81 u/e disappeared, but molecule at 80 u/e was not removed; c) IDI is applied, RF carpet at 48 $V_{peak-peak}$, no changes despite 30 % lower RF repelling voltage; d) IDI is applied, RF carpet at 42 $V_{peak-peak}$, the molecule at 80 u/e is removed, ^{80}Kr can be clearly identified; e) IDI is applied, RF carpet at 36 $V_{peak-peak}$, ^{78}Kr and ^{80}Kr peaks are suppressed.

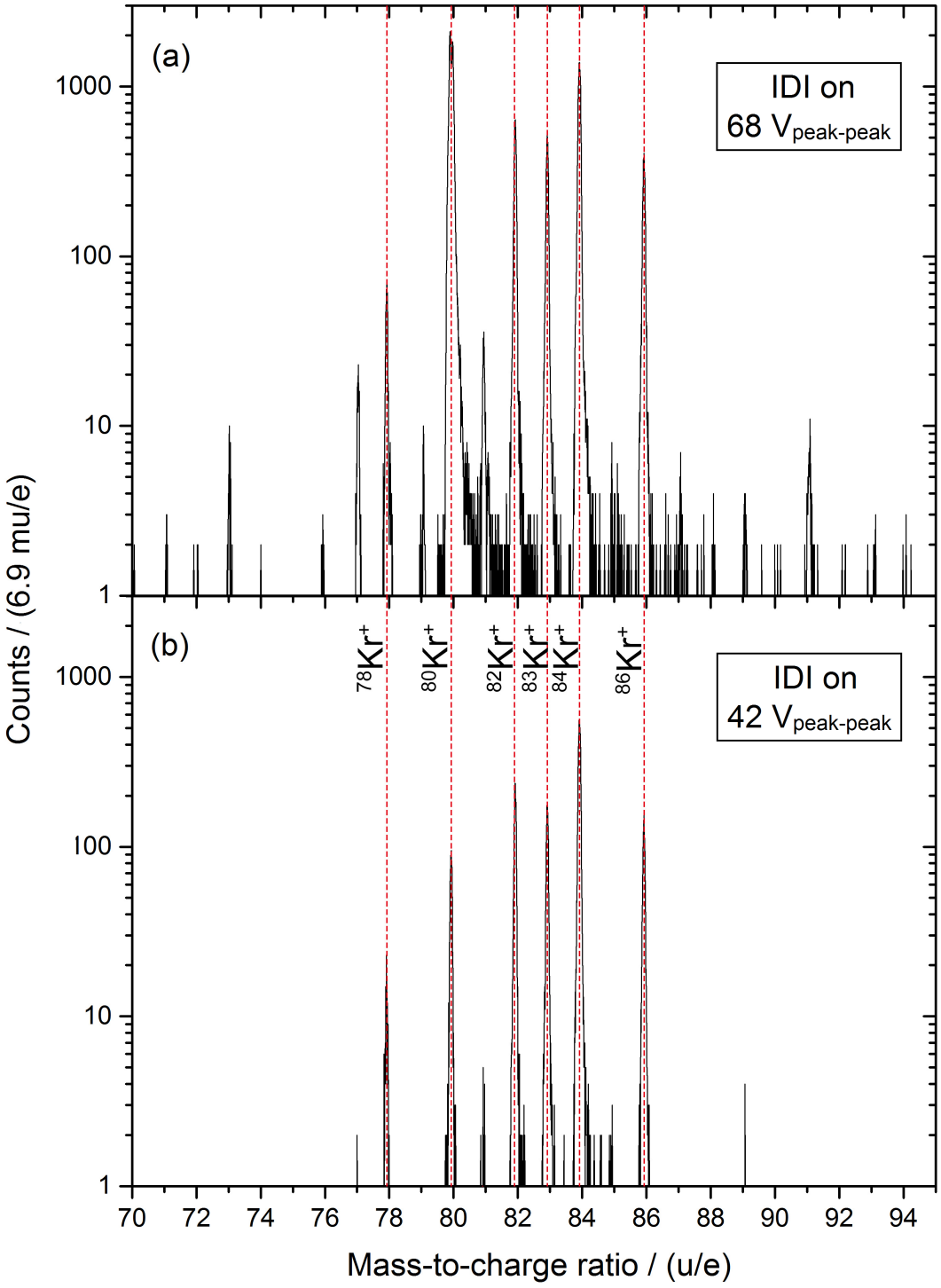

Figure 3.14: Measured mass spectra of ionization products extracted out of the CSC plotted in logarithmic scale. a) IDI is applied, RF carpet at 68 $V_{peak-peak}$ (spectrum from Fig. 3.13b); b) IDI is applied, RF carpet at 42 $V_{peak-peak}$ (spectrum from Fig. 3.13d). Separation by ion mobility at the RF carpet strongly suppresses the molecular background over a very broad mass-to-charge range.

4 Characterization of the system performance

An extended characterization of the CSC and the FRS Ion Catcher was done in [Reiter, 2015]. However, in the last years, complementary studies were conducted in order to complete the detailed understanding of the system and to build up profound experience for future experiments. In this chapter, the results of the latest characterization measurements are discussed.

4.1 RF carpet operation at high ionization rates

The rate capability of the cryogenic stopping cell was studied experimentally during the beam times at GSI in 2012 and 2014 [Reiter et al., 2016, Rink, 2017]. The measurements were done with two different fragments produced by projectile fragmentation of ^{238}U on a beryllium target at 1 GeV/u: ^{213}Fr and ^{221}Ac. Ions were separated in-flight in the FRS and stopped in the CSC of the FRS Ion Catcher. Short spills of 4 to 6 ms were used. The extracted ions were measured either by alpha spectroscopy with silicon detectors or by direct mass measurement with the MR-TOF-MS. The dependence of the extraction efficiency on the rate of the incoming ions was investigated.

To complement the experimental studies, simulations of thermalization and extraction of the ions were done [Heiße, 2015]. In the simulations, the ions of the nuclides ^{213}Fr and ^{221}Ac were used. The spatial distributions of the ions stopped in the CSC and of the ionization produced in the thermalization process were calculated with the MOCADI [Iwasa et al., 1997] and SRIM [Ziegler et al., 2010] simulation packages. The obtained distributions were used in the simulations of ions trajectories in SIMION [Manura and Dahl, 2006] software. There, a model with the actual geometry and experimental conditions of the stopping cell was created. In simulations of the ion motion, the DC electric fields created by the electrodes of the CSC, the space charge effects created by He_3^+ trimers (see paragraph "Challenges and solutions" of Subsection 2.2.1), and diffusion processes were considered. Examples of these simulations are shown in Fig. 4.1. The stopping volume of the CSC is shown in a sectional view. The ions enter the stopping cell from the left, ionize multiple helium atoms during the stopping process, are thermalized and transported towards the RF carpet with electric fields. In blue color, the equipotential lines of the electric fields are plotted. Black and red lines represent the trajectories of stopped ions and He_3^+ trimers

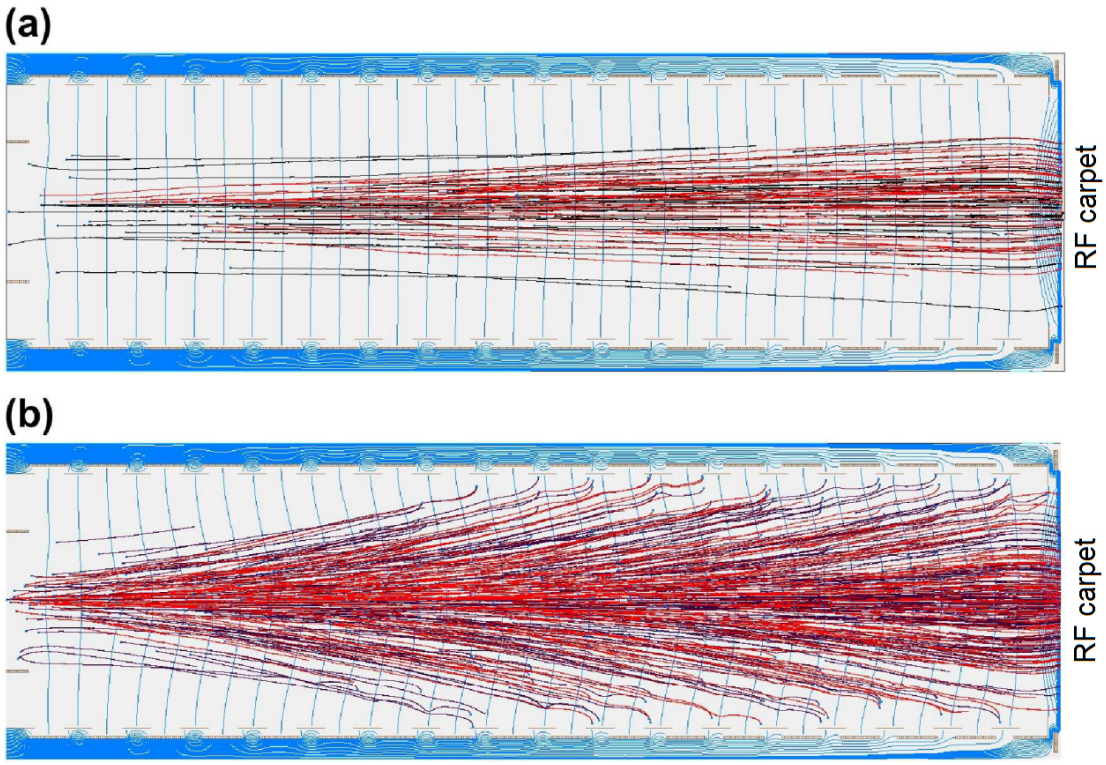

Figure 4.1: SIMION [Manura and Dahl, 2006] simulations of the CSC operation at different rates of the incoming ion beam [Reiter et al., 2016]. In the simulations, the ions of the nuclides ^{213}Fr and ^{221}Ac were used. Stopping volume of the CSC is shown in a sectional view. In blue color, the equipotential lines of electric fields are plotted; in black – trajectories of the stopped ions; in red – trajectories of the He_3^+ trimers. Ions enter the CSC from the left, are stopped and transported towards the RF carpet. a) beam rate of $\sim 10^4$ ions/s results in ionization rate of $\sim 10^{11}$ He_3^+/s, all ions are transported to the RF carpet; b) beam rate of $\sim 10^5$ ions/s results in ionization rate of $\sim 10^{12}$ He_3^+/s, part of the ions is deflected by the space charge and lost on the electrodes of the DC cage.

correspondingly. The upper part (a) of the figure shows the simulation, where the ion beam with a rate of $\sim 10^4$ ions/s hits the CSC and produces the ionization with a rate of $\sim 10^{11}$ He_3^+/s. The lower part (b) represents the case, where the incoming ion beam has a rate of $\sim 10^5$ ions/s, which results in the ionization rate of $\sim 10^{12}$ He_3^+/s. At lower ionization rates (a), the ion trajectories are not affected significantly by the space charge and all the stopped ions reach the RF carpet. In the case of a higher intensity of the incoming beam (b), a significant build-up of a positive charge leads to distortion of the electric fields and ion trajectories. The ions are deflected and partly lost on the electrodes of the DC cage. The repelling RF field of the RF carpet and the gas flow through the extraction nozzle were not included in the simulations. The ions that reached the RF carpet surface were considered to be extracted.

In the simulations, the space charge was produced by the DC beam, whereas in the performed experiments ion spills of 4-6 ms were used. Therefore, a correction factor

had to be determined from the simulations in order to be able to compare the obtained results quantitatively [Heiße, 2015]. The results of experimental measurements and simulations were proved to be in good agreement [Reiter et al., 2016, Rink, 2017].

However, in order to complete the detailed understanding and to fully validate the simulation model, it was crucial to perform the measurements with the DC beam injected into the CSC and to investigate the RF carpet operation at high intensities of the incoming beam. The extraction efficiency of the CSC ϵ_{ext} could be described as the function of the intensity of the incoming beam I and the repelling RF voltage of the RF carpet V_{RF}:

$$\epsilon_{\text{ext}} = f(I, V_{\text{RF}}). \tag{4.1}$$

The dependence of the RF carpet operation on the intensity of the incoming beam I was not studied in the previous measurements. Such investigations were conducted during the GSI beam time of 2016. The extraction efficiencies were determined for different rates of the ^{238}U primary beam. Uranium ions were thermalized in the CSC, extracted and measured with the MR-TOF-MS. As uranium is one of the most reactive elements, it tends to form molecules from residual contaminants contained in the buffer gas. The extraction efficiencies were calculated from the combined count rates of U^{2+}, UO^{2+}, UOH^{2+}, and UO_2^{2+} extracted out of the CSC, identified and measured with the MR-TOF-MS [Ayet San Andrés, 2018]. Measurements were done for three different values of the repelling RF voltage of the RF carpet. Experimental conditions were similar to the ones in measurement campaigns of 2012 and 2014. The CSC was operated with the helium areal density of 4.2 mg/cm^2 and a DC push field of $\sim$ 20 V/cm. The spill length of the ^{238}U primary beam was 1 s, in contrast to the very short spills of 4 to 6 ms used in previous measurements. In addition, in the beam time of 2016, there was a problem with the RF carpet operation, described in detail in Section 2.4. Due to this problem, ions spent a longer time at the RF carpet surface, which made the investigations of the RF carpet performance even more sensitive.

Figure 4.2 shows a compilation of the results of past investigations [Reiter et al., 2016] and the measurements performed in 2016. In 2016, three different values of the repelling RF voltage were used: 94 $V_{\text{peak-peak}}$, 40 $V_{\text{peak-peak}}$ and 28 $V_{\text{peak-peak}}$; which corresponded to 100 %, 100 % and 40 % transmission efficiency of the RF carpet respectively. Normalization of all data points measured with ^{238}U primary beam was done to the extraction efficiency corresponding to a beam intensity of $2.5 \cdot 10^3$ ions/s and 94 $V_{\text{peak-peak}}$ applied to the RF carpet. As it can be seen from the figure, the data points measured for the RF carpet operated at 40 $V_{\text{peak-peak}}$ agree within the error bars with the experimental and simulation results of the former rate capability studies. The measured points for the applied repelling voltage of 28 $V_{\text{peak-peak}}$ exhibit similar intensity dependence with the extraction efficiency reduced by a factor corresponding to the drop in the transmission efficiency of the RF carpet. The fact that these two data sets have the same slope of the efficiency decrease with the increasing beam rate indicates that the operation of the RF carpet is, therefore, not affected significantly by the presence of the space charge in the stopping volume of the CSC. The analytical expression for the extraction efficiency can be then rewritten as

$$\epsilon_{\text{ext}} = f(I) \cdot g(V_{\text{RF}}). \tag{4.2}$$

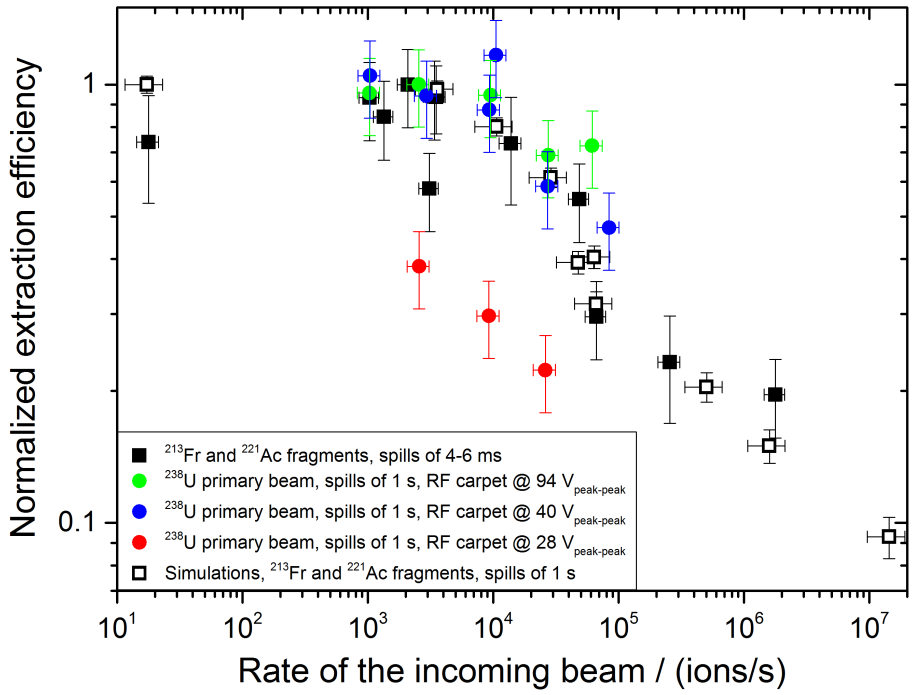

Figure 4.2: Extraction efficiencies of the ions stopped in the CSC for different rates of the incoming beam. Results of experimental measurements are represented in solid symbols; results of the simulations – in open symbols. Green – RF carpet is operated at 94 $V_{peak-peak}$; blue – RF carpet is operated at 40 $V_{peak-peak}$; red – RF carpet is operated at 28 $V_{peak-peak}$. Data series measured with ^{213}Fr and ^{221}Ac was normalized independently to a maximum extraction efficiency of unity. All data points measured with ^{238}U were normalized to the extraction efficiency corresponding to a beam intensity of $2.5 \cdot 10^3$ ions/s and 94 $V_{peak-peak}$ applied to the RF carpet.

The He_3^+ ions are not repelled and transported by the RF carpet, they hit the electrodes of the RF carpet and are neutralized. Therefore, the space charge in the vicinity of the RF carpet is smaller than in the stopping cell bulk and the main channel for ion losses are the losses on the DC cage electrodes, just as it was assumed in the simulations. The third data set measured for the RF carpet at 94 $V_{peak-peak}$ is another proof of this statement. There is no change in the extraction efficiency at high rates of the incoming beam even for repelling RF voltages that differ by more than a factor of two.

The good agreement between the experimental measurements with short and long spills is an additional verification for the chosen correction factor and for the simulation model in general. The new results not only provide additional confirmation to the rate capability studies but also complete the validation of the simulation model and justify its use for the CSC of the Super-FRS at FAIR [Dickel et al., 2016, Rink, 2017, Plaß et al., 2018].

4.2 Charge states of extracted ions

During the slowing-down process in the CSC, ions do multiple collisions with atoms of the buffer gas and undergo charge-exchange reactions. This process is explained in details in the paragraph "Challenges and solutions" of Subsection 2.2.1. If a collision occurs with a contaminant, which has a lower ionization potential than the ion of interest, then the ion can pick up an electron and be neutralized. Neutralized ions can not be extracted and guided with electric fields and are lost to the experiment. The charge state of the ion also affects the effective repelling field of the RF carpet, as can be seen from Eq. (1.19). Therefore, the ion survival and extraction efficiencies of the stopping cell are sensitive to the presence of contaminants. Levels of different impurities contained in the buffer gas were studied in [Reiter, 2015]. As a result, the assumption was made that charge-exchange processes in the CSC are governed by the ionization potential of N_2 molecules. N_2 is expected to be the most abundant ($\sim$ 100 ppb) contaminant with the first ionization potential lower than the one of helium (15.6 eV against 24.6 eV).

To validate this assumption, the charge states of extracted ions of 26 chemical elements were investigated. The measurements were conducted off-line with the internal sources and with ion beams during the beam times at GSI. The charge states were determined either by using the extraction RFQ as a mass filter in combination with a channeltron or silicon detector, or by high-resolution measurement with the MR-TOF-MS. The results are shown in Fig. 4.3 [Miskun et al., 2017]. For each chemical element, the predicted charge state (the upper half of the box) and the measured one (the lower half of the box) are presented in color code. As can be seen from the results, for 25 out of 26 investigated elements the predicted and measured charge states coincide, which indicates that the assumption of N_2 being the dominating contaminant in the helium buffer gas is correct. For the Sn isotopes, the ions were extracted in a lower charge state due to a non-optimal cleanliness of the CSC in that particular measurement. Nevertheless, the results demonstrate the general cleanliness of the CSC and the absence of such contaminants as O_2, H_2O, complex carbohydrates, etc. These contaminants have lower ionization potentials than N_2 and their presence would be indicated by lower charge states and even neutralization of thermalized ions of the investigated chemical elements.

However, further improvements on the cleanliness of the system and the buffer gas purification may lead to the survival of higher charge states of the stopped ions. According to Eq. (1.19), the effective repelling field of the RF carpet is proportional to the mass-to-charge ratio. Higher charge states of the ions can result in ion losses at the RF carpet and reduced extraction efficiency of the CSC. In this case, to compensate for the ion loss it would be necessary to decrease the areal density of the buffer gas or the strength of the DC push field. Therefore, for future operation, it is proposed to use trace gases in order to control the charge states of the thermalized ions [Dickel et al., 2016, Plaß et al., 2018].

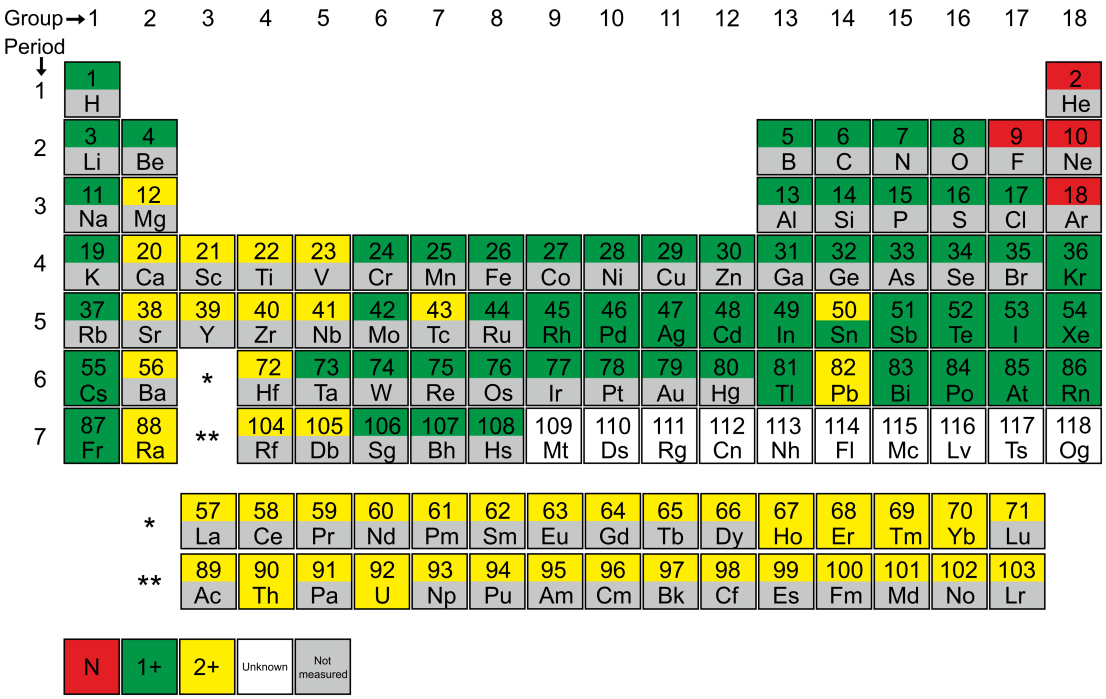

Figure 4.3: Periodic table of elements reflecting the charge states of ions extracted out of the CSC [Miskun et al., 2017]. For each element, the color of the upper half of the box indicates the predicted charge state; the color of the lower half – the charge state measured experimentally. The prediction was made based on the assumption of N_2 being the dominating contaminant in the helium buffer gas of the CSC. Charge states are plotted in the color code described at the bottom left of the figure. The values of ionization energies were taken from the NIST database [Kramida et al., 2019].

4.3 Homogeneity of the matter in the FRS

At hybrid facilities (see Subsection 1.2.3), the stopping efficiency of the gas-filled cell is the crucial parameter for the efficient use of a secondary beam. In order to stop all incoming ions, the areal density of the stopping cell has to be larger than the range distribution of the beam. This is a particular challenge for the ion beams produced at relativistic energies, as it was shown in Fig. 1.9. In this case, in order to minimize the range distribution of ions, the ion beam is energy bunched in the electromagnetic separator. To the standard deviation of the final range distribution σ_R, different effects are contributing. Among those are the collisional range straggling σ_{coll}, the charge-exchange range straggling σ_{chex} [Weick et al., 2002], and the thickness variation of the matter in the beamline $\sigma_{\delta x}$:

$$\sigma_R^2 = \sigma_{\text{coll}}^2 + \sigma_{\text{chex}}^2 + \sigma_{\delta x}^2, \tag{4.3}$$

One of the most probable sources for the thickness variation of the matter in the beamline of the FRS is the surface roughness of aluminum degraders. The homogeneity of the matter in the FRS, i.e. the thickness variations δx, was investigated with the FRS Ion Catcher during the experiments at GSI in 2016. ^{238}U primary beam at an energy of 300 MeV/u was used for the investigations. The beam spot of the primary beam at the final focal plane of the FRS had a diameter of 1 mm. Therefore, the contribution of the thickness variation to the range straggling $\sigma_{\delta x}$ was negligible. The relatively low energy of the primary beam also resulted in a relatively small collisional range straggling. σ_{coll} of the range distribution in aluminum estimated by ATIMA [Weick et al., 2018] calculations is $\sigma_{\text{ATIMA}} \sim 1.5$ mg/cm^2. Experimentally, the range distributions were measured with the FRS Ion Catcher. For this, the amount of matter in the beamline was changed by varying the thickness of a homogeneous aluminum degrader positioned in front of the CSC and the rate of stopped and extracted ions was measured. Similar to the measurement described in Section 4.1, the ions of U^{2+}, UO^{2+}, UOH^{2+}, and UO_2^{2+} were used in the investigations.

The schematic representation of all PID detectors, degraders, and other elements that were inserted in the beamline is shown in Fig. 4.4. Due to the low beam energy, only the necessary minimum of the PID detectors was used. Apart from the standard FRS equipment, the prototype of a gas degrader (GD) [Purushothaman et al., 2017b] was positioned at the final focal plane in front of the homogeneous aluminum degrader. The gas degrader is a stainless steel chamber filled with dry nitrogen gas at the set pressure. For its beam entrance and exit windows, 100 μm thick Kapton foils coated with a thin layer of carbon are used. Carbon coating is done to prevent beam-induced charging up and possible electrical discharges. The beam windows have dimensions of 200 mm $\times$ 100 mm and contribute 2 $\times$ 20 mg/cm^2 to the total areal density of the gas degrader. The areal density of the degrading nitrogen gas can be set from 0 to 160 mg/cm^2 with $\pm$0.2 % accuracy. The gas degrader has a smaller minimum thickness than the aluminum degraders and, therefore, can be used for slowing down of low-energy ion beams. It is proposed to be used at the Low-Energy Branch (LEB) of the Super-FRS at FAIR [Geissel et al., 2003, Winfield et al., 2013] and was first commissioned with the FRS Ion Catcher setup.

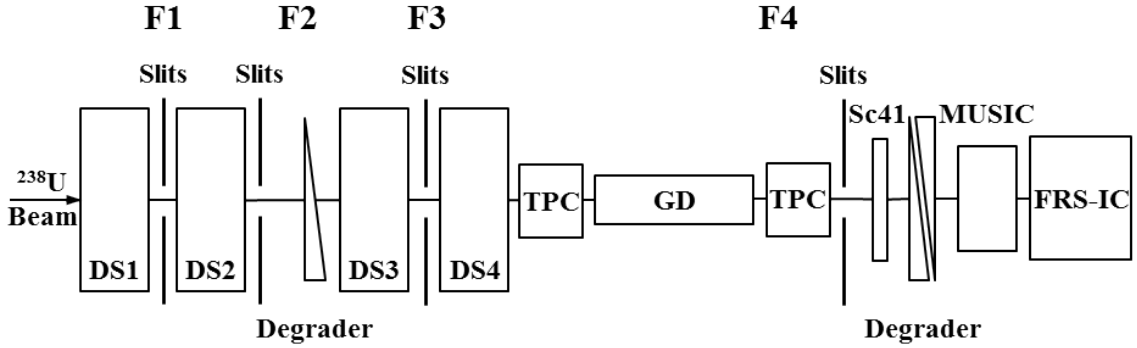

Figure 4.4: Schematic view of elements inserted in the beamline during the measurements of the homogeneity of matter in the FRS. See Section 2.4 for details. Dipole stages (DS1..DS4) and focal planes (F1..F4) of the FRS are labeled.

Results of the range distribution measurements are shown in Fig. 4.5. The range distributions were measured for three different beam positions at the final focal plane: on axis, 3.2 cm off axis, and 8.8 cm off axis along the horizontal axis perpendicular to the beam direction. For the beam positioned on axis, the measurements were done for two values of areal densities of dry nitrogen in the gas degrader – 85 mg/cm^2 and 129 mg/cm^2. All data points were normalized to the maximum measured ion rate within each individual data set. Measured rates for the beam positioned off axis were, in addition, normalized to the incoming beam intensity measured by the scintillator SC41. Error bars reflect the statistical uncertainties. For the measurements at the beam on-axis position, there was no data for normalization from the scintillator. Therefore, an additional uncertainty was added to the statistical uncertainties for both measurements at the beam on-axis position in order to compensate for the beam intensity fluctuations. The fluctuation of beam intensities was estimated from the logged extraction currents of the SIS18. The measured distributions were fitted with Gaussian functions. For the beam on-axis position and 85 mg/cm^2 areal density of the gas degrader, the scatter of the measured data points was too large to perform a free fit with the Gaussian. Therefore, for this data set, the standard deviation of the distribution σ was fixed to the weighted average of the standard deviations obtained from the other measurements. As the mean range of ions in all four data sets was not changed drastically, the range straggling contribution and the width of the range distributions should be practically the same. In Table 4.1, the obtained parameters of the range distributions are shown. The measured standard deviations σ_{meas} had to be corrected for the thickness of the CSC in order to obtain the real values σ_{corr} of the range distributions. For this, an FWHM of the CSC of 4.2 mg/cm^2 was subtracted from the results quadratically.

The results show that the weighted average of the measured standard deviations of the range distributions in aluminum ($\langle\sigma_{\mathrm{corr}}\rangle = 7.8 \pm 0.4$ mg/cm^2) is more than a factor of five larger than the theoretically predicted collisional range straggling ($\sigma_{\mathrm{ATIMA}} \sim 1.5$ mg/cm^2). Due to the small beam spot, the contribution of the thickness variation could also not be significant. This means that the range distribution of the ions for these experimental conditions is dominated by the charge-exchange straggling

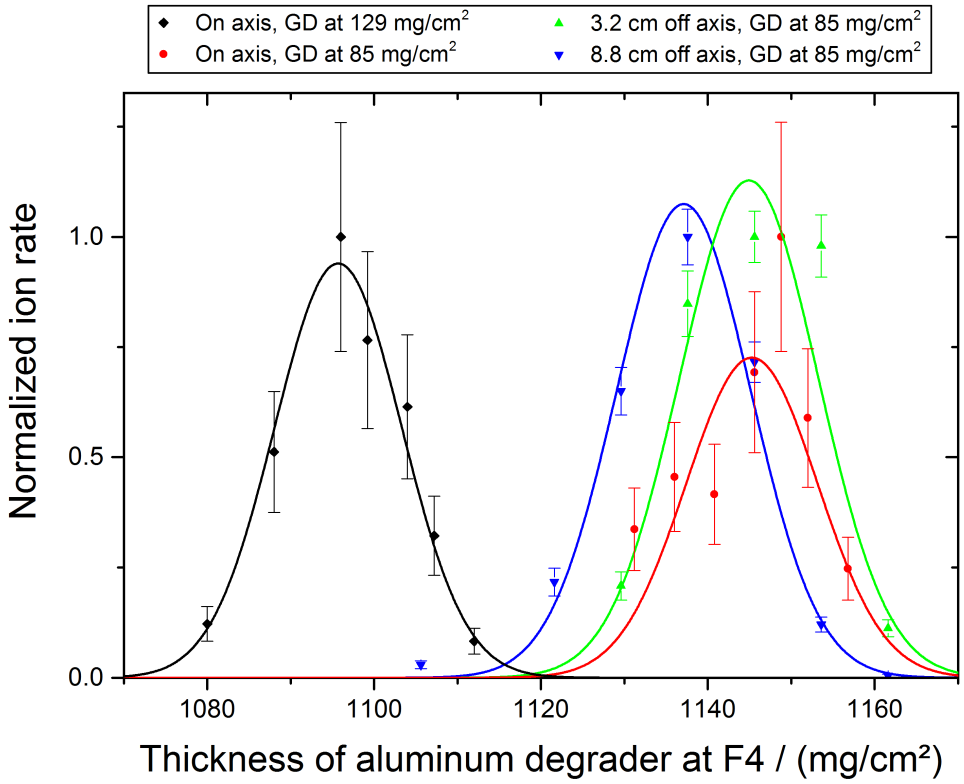

Figure 4.5: Range distributions of ^{238}U primary beam measured with the FRS Ion Catcher for different beam positions. Normalized rate of stopped and extracted ions is plotted for different values of homogeneous aluminum degrader thickness. Range distributions are fitted with Gaussian functions. Obtained peak parameters for all data sets are presented in Table 4.1.

[Weick et al., 2002]. The shift in the mean of the range distributions X_c for the beam position scan represents the homogeneity of the matter. The areal density of the gas degrader of 85 mg/cm^2 used in the position scan corresponded to 525 mbar pressure of the degrading nitrogen gas. Due to the difference to the atmospheric pressure, the Kapton windows of the gas degrader had a concave shape. This deformation of the beam windows resulted in different effective lengths of the degrader and, therefore, different amounts of degrading gas for beam on-axis and off-axis positions. However, only a small shift of $\sim$ 2 mg/cm^2 is expected from the curvature radius of the concave windows, whereas the measured shift is more than 8 mg/cm^2. This areal density corresponds to the thickness variation of $\sim 20 - 30$ μm of aluminum, which is a reasonable value for the surface roughness of the aluminum degrader [Weick, 2019].

The measured range distributions for two different areal density values of the degrading nitrogen gas validate the concept of the gas degrader. A change of 44 mg/cm^2 in the areal density of the gas degrader resulted in a corresponding change in the required thickness of the aluminum degrader within the estimated uncertainties.

The conditions chosen for this experiment are similar to the ones, which are going to be used at the Low-Energy Branch of the Super-FRS at FAIR. The obtained results

Data set	σ_{meas} / **(mg/cm^2)**	σ_{corr} / **(mg/cm^2)**	X_c / **(mg/cm^2)**
Beam on axis GD at 129 mg/cm^2	7.6±0.6	7.5±0.6	1095.7±1.1
Beam on axis GD at 85 mg/cm^2	7.9 (fixed σ)	7.8 (fixed σ)	1145.3±1.9
Beam 3.2 cm off axis GD at 85 mg/cm^2	8.3±1.0	8.2±1.0	1144.9±1.7
Beam 8.8 cm off axis GD at 85 mg/cm^2	8.0±0.6	7.9±0.6	1137.1±1.2

Table 4.1: Peak parameters of measured range distributions for different positions of the beam and different areal density values of the gas degrader (GD). For the data set corresponding to the beam on-axis position and GD at 85 mg/cm^2, the standard deviation value was fixed to the weighted average of the standard deviations obtained from the other data sets. The measured standard deviations σ_{meas} are corrected for the thickness of the CSC in order to obtain the real values of the standard deviations of the range distributions σ_{corr}.

indicate that a stopping cell with a higher areal density of buffer gas is required in order to achieve a stopping efficiency close to unity. This requirement will be met in the next-generation cryogenic stopping cell for the LEB of the Super-FRS, which will be operated at an areal density of $\sim$ 30 mg/cm^2 for heavy fragments thermalization and extraction [Dickel et al., 2016, Plaß et al., 2018, Amanbayev et al., 2018]. For the range distribution with a standard deviation of 8 mg/cm^2, this areal density corresponds to the stopping efficiency of $\sim$ 95 %.

5 A novel method for the measurement of half-lives and decay branching ratios of exotic nuclei

As discussed in Chapter 1, half-lives and decay branching ratios are important properties of exotic nuclei. They are crucial for the improvement and further development of nuclear structure models and understanding of astrophysical nucleosynthesis processes [Iliadis, 2015]. At the FRS Ion Catcher, a novel method for the measurement of half-lives and branching ratios has been developed [Miskun et al., 2019]. It allows simultaneous measurement of masses, Q-values, isomer excitation energies, half-lives and decay branching ratios of exotic nuclei. The method is based on using the cryogenic stopping cell of the FRS-IC as an ion trap for controllable storage of mother and daughter nuclides for a variable duration and their subsequent measurement with the multiple-reflection time-of-flight mass spectrometer. The novel method is independent and complementary to the existing measurement techniques. It combines the advantages of using a gas-filled cell for storage and retrapping of decay recoils and identifying them by direct mass measurement with the MR-TOF-MS (see Section 1.4). A detailed description of the method, first off-line and on-line results, as well as possible future applications, are discussed in this chapter.

5.1 Description of the concept

The developed method has been implemented in the FRS Ion Catcher at the FRS at GSI. It uses the combination of unique performance characteristics of the heavy-ion synchrotron SIS-18, the fragment separator, and the FRS-IC.

The concept of this method is shown schematically in Fig. 5.1. The pulsed primary beam is accelerated to relativistic energies of up to 1 GeV/u in the SIS-18 synchrotron and focused on the target for projectile fission or fragmentation. The fragments are separated in-flight, energy bunched and slowed down in the FRS and delivered to the FRS-IC. The ensemble of ions consisting mainly of the mother nuclide of interest is thermalized in the stopping cell and stored there for a controllable duration. The mother nuclei undergo decay, populating the daughter nuclides, which are also stopped

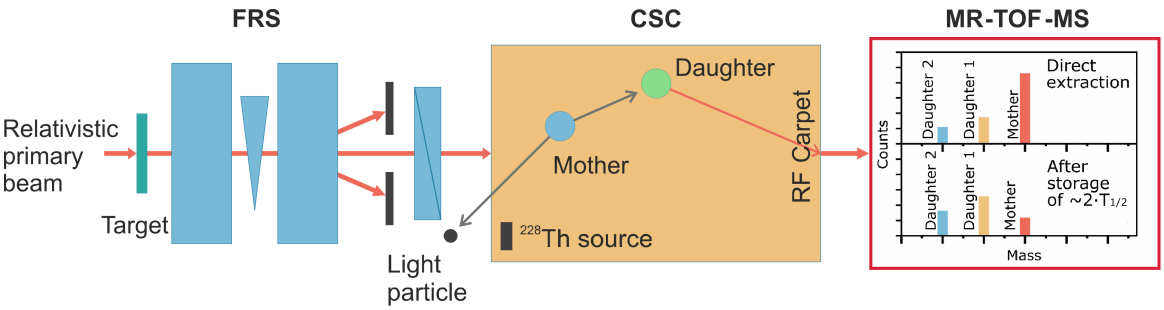

Figure 5.1: Scheme of the novel method for half-lives and decay branching ratios measurements with the FRS Ion Catcher. In blue color the degrading material is shown; in orange – the active stopping volume of the CSC. The internal ^{228}Th recoil source, which was used for the off-line measurements, is also shown. See text for details.

in the buffer gas of the CSC. It is the first time for a gas-filled stopping cell to be used as an ion trap for controllable storage of ions. After a certain storage time, all ions are simultaneously extracted towards the MR-TOF-MS. In the MR-TOF-MS, identification, counting and high-resolution mass measurement of mother and daughter nuclides are done. From the measured abundances, the half-life of the mother nuclide and its decay branching ratios can be deduced. In addition, masses and, therefore, Q-values and isomer excitation energies are measured with high accuracy. Only very general prior knowledge of nuclear properties of the nuclei to be investigated is required, as most of them are measured during the experiment. The measurements are done for different storage times in order to reduce systematic uncertainties.

The described method is only possible with the FRS and the FRS Ion Catcher setup at GSI. High energies of a primary beam (up to 1 GeV/u for ^{238}U) provided by the SIS-18 result in high energies of the fragments, which are necessary for the required clean separation of the fragments in the FRS. Otherwise, it would not be possible to obtain a pure sample of mother nuclei stopped in the CSC. The presence of other nuclides in the sample might spoil the measurement, as discussed in detail in the next subsection. In addition, the pulsed time structure of a primary beam, as provided by the synchrotron, is required for accurate control of the storage time. The ion ensemble is injected into the CSC as a short pulse, stored and extracted before the next ensemble arrives. At other in-flight radioactive ion beam facilities, where cyclotrons are used for ion acceleration, continuous primary beams of lower energies are produced. For example, at RIKEN the energy of a primary beam reaches 345 MeV/u. At this energy, the required clean separation is not possible. It was shown that different isotones cannot be separated [Kubo, 2003]. To implement there the method discussed in this work, additional instrumentation is needed for pulsing and purification of the fragment beam. As it was already discussed in Subsection 1.4.1, it was proposed in [Miyatake et al., 2018] to use a series of gas-filled stopping cells and MR-TOF-MSs as a possible solution.

5.1.1 Production of a pure sample of mother nuclei

One of the most important requirements of the method is to obtain a relatively pure sample of mother nuclei stopped in the CSC. The presence of other nuclei, which decay into the mother nuclide of interest or some of its daughters, will harm the abundance measurement and may make a deduction of half-lives and branching ratios impossible. An example of unwanted nuclides for β-delayed neutron emission measurement is shown in Fig. 5.2. The mother nuclide of interest (N, Z) marked green undergoes β-, βn- and $\beta 2n$-decays. All the isotopes highlighted with red color will contribute to the background, populating either the mother nuclide or its daughters. Their presence in the stopped ensemble of ions is critical for the measurement. The presence of daughter nuclides themselves (yellow) in the initial ensemble is also unwanted, however, it can be easily corrected for by measuring the background at a very short storage time and subtracting it from the results. Isotopes marked white will not contribute to the problematic background and, therefore, can be tolerated. In a similar way, unwanted isotopes can be identified for any type of decay.

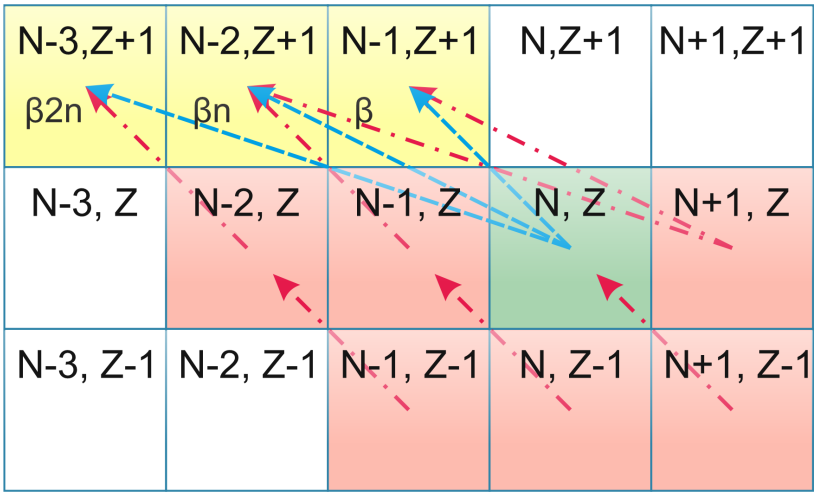

Figure 5.2: Visualization of nuclides that hinder the measurement of half-life and decay branching ratios for the case of β-delayed neutron emission. The mother nuclide of interest (N, Z) is in green. In yellow are the daughter nuclides that are produced in β-, βn- and $\beta 2n$-decays. In red are the nuclides that will contribute to the problematic background by populating the mother or the daughter nuclides. In white are the nuclides that will not affect the measurement and can be tolerated.

At the fragment separator at GSI, produced beams of exotic nuclei can be purified to the required level due to the high energy of the fragments. Obtaining a sample of ions containing mainly the mother nuclide of interest is possible by operating the FRS in an achromatic mode and using slits to remove the unwanted isotopes [Geissel et al., 1992a] (see Subsection 1.2.2). Another way is to operate the FRS in a monochromatic mode and use the differences in range distributions of different nuclides and the relatively small stopping thickness of the CSC [Hornung, 2018]. To demonstrate the latter approach, simulations were done with LISE++[Tarasov and Bazin, 2008] and MOCADI [Iwasa et al., 1997] software packages. ^{137}Sb was chosen as the mother nuclide of interest. In the simulations, fragments were produced using a ^{238}U primary beam with an energy of 800 MeV/u and intensity of $2 \cdot 10^9$ ions/s and a lead target with a thickness of 2,600 mg/cm^2. Yields of ^{137}Sb and all neighboring nuclides (according to Fig. 5.2) for different range in helium were calculated for the monochromatic operation mode of the FRS. Results of the simulations are plotted in Fig. 5.3. The number of stopped ions can be calculated by the definite integral of the range distribution of the nuclides over the thickness of the CSC. The shaded area represents the 10 mg/cm^2 thickness of the stopping cell. In order to obtain a clean sample of ^{137}Sb isotope, the CSC should cover a part of the range distribution between 1180 and 1190 mg/cm^2, as shown in Fig. 5.3. In practice, the first 1180 mg/cm^2 of helium are replaced by the equivalent amount of aluminum degrading material. In this setting, the most abundant harmful contaminant, which is also thermalized in the stopping cell, is the ^{137}Te isotope, a β-decay daughter nuclide of ^{137}Sb, with a relative abundance of 10^{-2}. This abundance can be measured at short storage times and subtracted from the results. ^{138}Te is stopped in amounts similar to ^{137}Sb, but does not harm the measurement, as it is one of the "white" isotopes from Fig. 5.2. From other "yellow" and "red" nuclides, ^{136}Sn and ^{137}Sn are stopped in the CSC with relative abundances at a level of 10^{-5}. All other nuclides are practically not present. From the results of the simulations, it was suggested to set a lower limit of 10^{-4} for the measurable branching ratios for such decays of neutron-rich isotopes. This limit will be different for different mother nuclides and decay channels, depending on the region of the chart of the nuclides and each particular case.

It is also important to mention that for investigations of γ-decaying nuclides there will always be non-zero contamination, because isomeric states will not be separated in the FRS. However, in this case, the ground state of the nuclide will be the "yellow" isotope from Fig. 5.2 and the results can be corrected for its initial amount measured at small storage times.

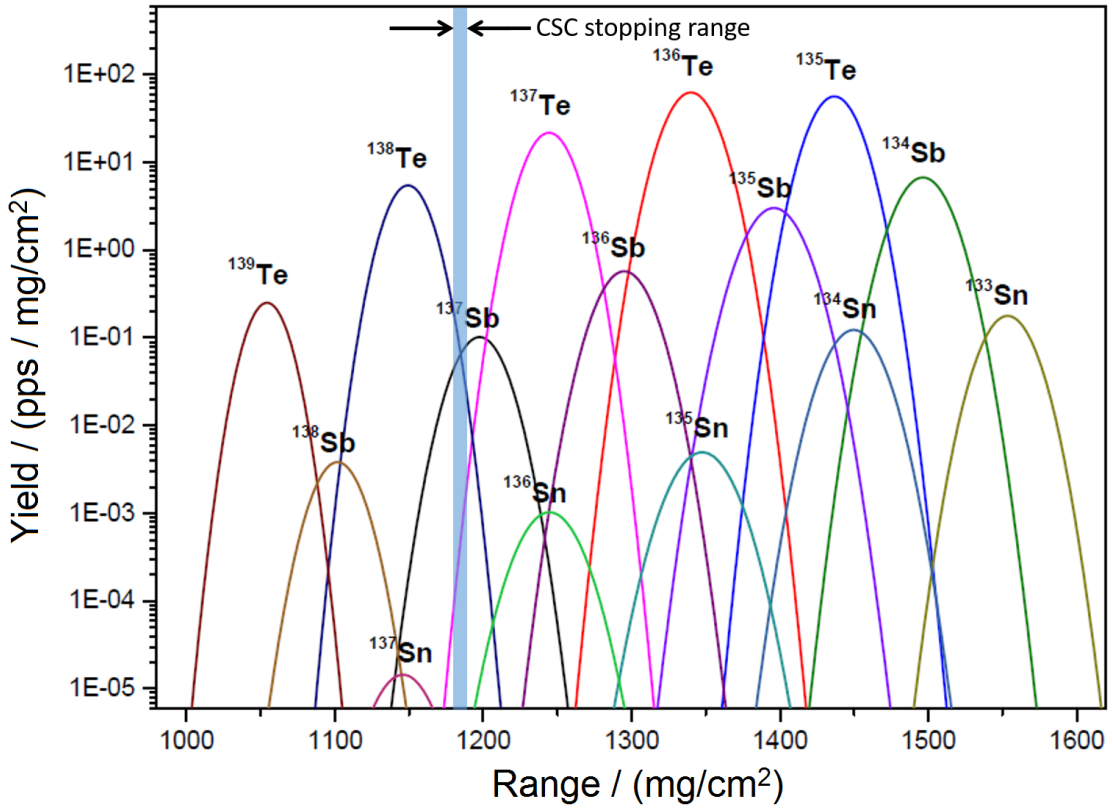

Figure 5.3: Calculated yields of ^{137}Sb and its neighboring nuclides (according to Fig. 5.2) per range in helium [Miskun et al., 2019]. Calculations were done with LISE++ software. Main simulation settings are: ^{238}U primary beam with an initial energy of 800 MeV/u and intensity of $2 \cdot 10^9$ ions/s, Pb target with a thickness of 2.6 g/cm^2, monochromatic operation mode of the FRS, monoenergetic degrader with a thickness of 7 g/cm^2 corresponding to d/R=0.54 of the range of the fragments in aluminum. The energy of the ^{137}Sb nuclei after the monoenergetic degrader is 420 MeV/u. The shaded area corresponds to the 10 mg/cm^2 thick CSC positioned for the optimum thermalization of the ^{137}Sb mother nuclei.

5.1.2 Retrapping of daughter nuclides

After the ion sample containing the mother nuclide of interest is stopped in the CSC, it is stored there for a controllable duration. The mother nuclides undergo decay and produce the daughter nuclides, which have to be thermalized or, in other words, recaptured in the helium buffer gas. Depending on the type of decay, decay products have different energies and, therefore, different stopping ranges (see Subsection 1.4.1). To estimate the stopping ranges of daughter nuclides in the CSC for different decay types, simulations were done with SRIM (Stopping and Range of Ions in Matter) software [Ziegler et al., 2010]. A helium gas density of 40 μg/cm^3, which corresponds to the typical areal density of the CSC of 4.2 mg/cm^2, was used in the simulations. In γ-decay, the daughter nuclide obtains kinetic energy of a few tens of electronvolts, which results in a stopping range distribution of a few tens of micrometers. In β-decay, the recoil has an order of magnitude higher kinetic energy and a range distribution of $0.05 - 0.2$ mm. In case of β-delayed or direct nucleon emission, the daughter nuclide has a kinetic energy of a few tens of kiloelectronvolts and a corresponding stopping range of $0.5 - 2.0$ mm. Finally, in α-decay, the recoils have the largest kinetic energies of $100 - 200$ keV and their range distribution reaches up to 10 mm.

The active stopping volume of the CSC has a diameter of 25 cm and a length of 105 cm, as described in Subsection 2.2.1. As long as decays occur in the bulk of the helium buffer gas, there is no risk of losing the produced daughter nuclides. However, the first off-line and on-line measurements with this method (Sections 5.2 and 5.3) were done by storing the ions at the surface of the RF carpet close to the extraction nozzle. In these studies, nuclides undergoing α- and γ-decays were investigated. The RF carpet has an electrode pitch of 0.25 mm, and the repelled ions are kept at the distance approximately equal to a half of the pitch size, that is ~ 0.125 mm [Ranjan et al., 2011]. Therefore, half of the daughter nuclides produced in α-decay at the RF carpet surface will be lost on the electrodes. The other half will recoil in the direction away from the RF carpet into the helium bulk, will be stopped, extracted and measured with the MR-TOF-MS. Corresponding corrections have to be introduced to the measured counts in order to compensate for the lost ions. In case of γ-decaying nuclides, such corrections are not needed, because the stopping range of the daughter nuclides is very small and no ions will hit the RF carpet surface and be lost for the measurement.

For β-decays and β-delayed or direct nucleon emission, the stopping range distributions of recoils are of the same order of magnitude as the distance to the RF carpet. In these cases, it is hard to accurately estimate the number of lost ions and to correct for it. To solve this problem, a dynamic storage of the ions inside the CSC can be done. This allows the storage of ions mostly in the bulk of the helium buffer gas, where the products of decays of all types are recaptured. This technique has been investigated in simulations and is discussed in detail in Section 5.4.

5.1.3 Measurement of masses and abundances

After the ions are extracted out of the CSC, they are transported to the MR-TOF-MS, where high-resolution mass measurements and isotope counting are done. Performance characteristics of the MR-TOF-MS are another essential pillar of the discussed method. The broadband and non-scanning measurement technique allows simultaneous measurement of the mother nuclide and all of its daughters. It makes the use of beam time more efficient and leads to a reduction of systematic errors, which might occur during sequential measurements. High resolution is needed to separate and identify all nuclei of interest. The short measurement time of a few milliseconds ensures that no additional uncertainty arises due to decays, which occur in the MR-TOF-MS instead of the CSC.

Accurate determination of masses and abundances is done with the elaborated analysis procedure [Ayet San Andrés et al., 2019] described in Section 2.3. As mentioned earlier, the procedure is capable of handling overlapping peaks, also of strongly different relative abundances, and very low-statistics peaks (down to ~ 10 counts), which is of great importance for the discussed method. Even very weak decay branches can thus be identified and measured.

5.1.4 Measurement of half-life and branching ratios

The storage time of ions can be varied from the CSC extraction time value (~ 50 ms) to the duration of up to 10 s, as demonstrated in Subsection 5.2.2. Within these storage times, half-lives of a very wide range of exotic nuclei and their isomers can be measured. Decay branching ratios are calculated as the ratios between the abundances of each particular daughter nuclide and the sum of abundances of all daughter nuclides.

The analysis of the obtained data is done in the following way [Miskun et al., 2019]. Measured counts of the mother ($P(t)$) and daughter ($R_i(t)$) nuclides are fitted to the well-known solutions of Bateman equations [Bateman, 1910]:

$$P(t) = A_p \cdot e^{-\lambda_P \cdot t}, \tag{5.1}$$

$$R_i(t) = y_{0i} \cdot e^{-\lambda_{Ri} \cdot t} + \frac{\lambda_P}{\lambda_{Ri} - \lambda_P} \cdot n_{ri} \cdot A_p \cdot \left(e^{-\lambda_P \cdot t} - e^{-\lambda_{Ri} \cdot t} \right), \tag{5.2}$$

where A_p is the initial amount of mother nuclei in the ion sample, λ_P and λ_{Ri} are the decay constants of the mother and daughter nuclides, y_{0i} is an initial background of the i'th daughter nuclide, and n_{ri} is the i'th decay branching ratio. Decay constants are related to the half-lives by $\lambda = \ln 2 / T_{1/2}$. The sum of n_{ri} is equal to unity.

For the cases when the half-lives of the daughter nuclides are much longer than the half-life of the mother nuclide and the storage times, it is possible to assume $\lambda_{Ri} \to 0$

and to simplify Eq. (5.2) to

$$R_i(t) = y_{0i} + n_{ri} \cdot A_p \cdot \left(1 - e^{-\lambda_P \cdot t}\right). \tag{5.3}$$

In order to reduce statistical and systematic uncertainties, all sets of data of the mother and daughter nuclides are fitted with one global fit. The fit uses Eq. (5.1) for the mother nuclide data and Eq. (5.2) or Eq. (5.3) for the daughter nuclides data, enforcing a shared parameter λ_P for all data sets. This gives an advantage of constant statistics for all storage time values, whereas if the mother nuclide decay is fitted separately, the statistics decreases with the storage time as less and less mother nuclide counts are detected. Apart from that, in the global fit, all branching ratios (n_{ri}), initial backgrounds (y_{0i}) and the initial amount of the mother nuclide (A_p) are constrained to be non-negative. The sum of all n_{ri} is constrained to be equal to 1.

The half-life and decay branching ratios can be also extracted from a single measurement at a fixed storage time in the case, if the initial backgrounds y_{0i} of the daughter nuclides are negligible or known, and if the half-lives of the daughter nuclides are relatively long ($\lambda_{Ri} \to 0$). For the case when $y_{0i} = 0$, the formula for half-life calculation can be derived by the division of Eq. (5.1) by sums of Eq. (5.3) for all daughter nuclides and subsequent algebraic manipulations:

$$T_{1/2} = \ln 2 \cdot t_s \cdot \left[\ln \frac{1+D}{D}\right]^{-1}, \tag{5.4}$$

where $D = P/R$ and t_s is the storage time. The decay branching ratios can be calculated by:

$$n_{ri} = \frac{R_i(t_s)}{\Sigma R_i(t_s)}. \tag{5.5}$$

The statistical uncertainties of the half-lives and branching ratios depend on the uncertainties of the measured counts, which are given by the MR-TOF-MS analysis procedure (see Section 2.3). They include statistical errors of the measured counts and the peak shape error of the fitting routine.

One of the possible contributions to the systematic uncertainties is a loss of ions due to charge-exchange reactions or molecule formation in the CSC. These processes, in principle, are element dependent and might drastically affect the measurement of branching ratios. However, it has been shown in previous investigations [Plaß et al., 2019] that the ion survival and extraction efficiency of the CSC is almost element independent. As a part of these studies, the efficiencies were compared for one of the least reactive chemical elements (Rn, noble gas) and one of the most reactive ones (Th). Results presented in this work (Subsection 5.2.2) also support the statement about the negligibility of the non-nuclear-decay losses.

As it was discussed in Section 4.2, isotopes of different chemical elements are extracted out of the CSC in different charge states. In cases of different charge states of the mother and daughter nuclides, both mass-to-charge regions have to be measured with the MR-TOF-MS. For newly-investigated chemical elements, the temporal behavior and the charge states distributions can be studied using stable or near-stable isotopes of these elements.

5.2 First off-line tests and proof of principle

The method was first tested and investigated in a series of off-line measurements [Miskun et al., 2019]. For these investigations, the ions from the internal ^{228}Th α-recoil source (see Section 3.1) were used. The storage of ions inside the CSC was reached by applying a high blocking potential to the extraction nozzle for an adjustable duration. In order to extract stored ions, the nozzle potential was pulsed low to its nominal voltage for a few milliseconds. The CSC was operated with 33 mbar of helium buffer gas at a temperature of 74 K, which corresponds to an areal density of 2.3 mg/cm^2. Results are discussed in the following sub-sections.

5.2.1 Transport time measurement

As the very first step of the method development, it was important to clarify that, after the storage in the CSC, the ions can be extracted and transported to the detector as a single bunch within a reasonably small time. If this would not be the case, it would mean that the ions are trapped either at the extraction nozzle or in the RFQ beamline, which would add additional uncertainty to the measurement.

For this test, the ^{228}Th source was pulsed, delivering a bunch of ions to the stopping volume of the CSC. The ions were thermalized, transported to the RF carpet, and accumulated at the extraction nozzle, which was on a high potential to block the ion extraction. The nozzle potential was then pulsed down to its nominal value, allowing extraction of ions into the RFQ beamline. Lowering of the nozzle potential triggered the time-to-digital converter (TDC) used for the data acquisition, and the number of ions arrived at the detector at different MR-TOF-MS cycles was measured. The MR-TOF-MS was operated at a repetition rate of 50 Hz. For the measurement, the ^{220}Rn$^+$ ions were used, because all the ions of this nuclide were extracted singly-charged, and its half-life (55.6 s) is long enough compared to the transport time in order to not take into account the ion losses due to the nuclear decay.

Results of this test are shown in Fig. 5.4. ^{220}Rn$^+$ ions were measured at each MR-TOF-MS cycle after the nozzle opening and normalized to their total amount. As can be seen from the plot, most of the ions from the original bunch (more than 90 %) arrive at the detector at the very first MR-TOF-MS cycle of 20 ms. A smaller fraction of a few percents misses the first cycle and makes it to the detector during the second one. However, only $\sim$ 0.3 % of ions are scattered and arrive at the detector in later cycles. From this, it is possible to conclude that, for the nuclides with half-lives of hundred milliseconds and larger, the transport time will not bring any significant contribution to the systematic uncertainties.

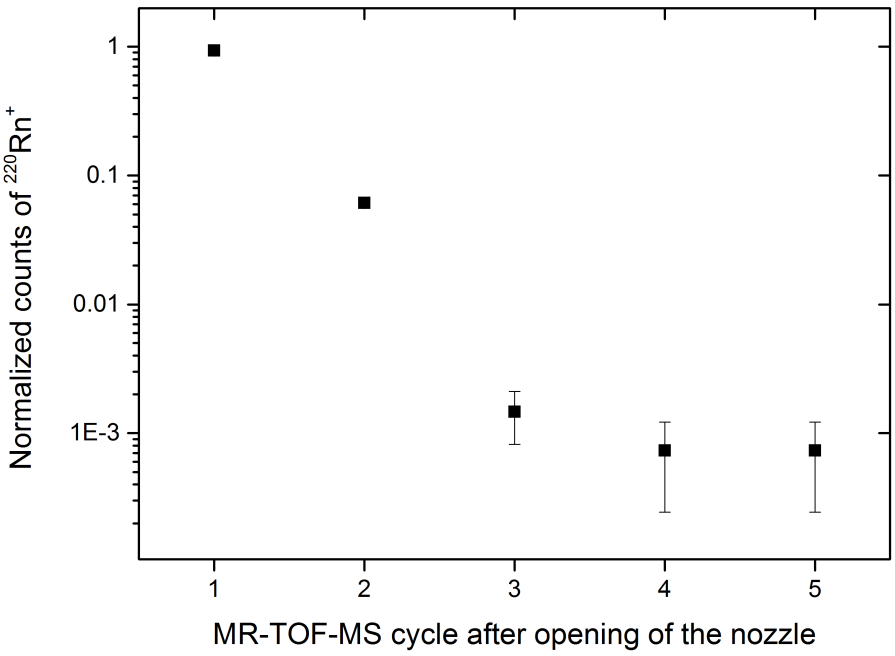

Figure 5.4: Measured counts of the $^{220}Rn^{+}$ ions at different MR-TOF-MS cycles after releasing the ion bunch from the extraction nozzle of the CSC. The MR-TOF-MS was operated at a repetition rate of 50 Hz. Normalization is done to the total amount of measured $^{220}Rn^{+}$ ions. Most of the ions arrive at the detector as a single bunch during the first MR-TOF-MS cycle of 20 ms.

5.2.2 Ion storage in the CSC

One of the most important steps in the development of the discussed method was to demonstrate that the ion storage inside the CSC is possible without significant non-decay losses occurring, for example, due to the neutralization of ions in collisions with contaminant atoms or electrodes of the CSC. For this, stable and relatively long-lived products of the ^{228}Th source were used. A bunch of ions was released from the pulsed source, transported to the RF carpet, focused at the extraction nozzle, and stored there for a certain time. Afterwards, the ions were extracted out of the CSC and measured with the MR-TOF-MS. The measurement was repeated for different storage times.

In these investigations, the MR-TOF-MS was operated in TFS mode. The singly-charged ions of the nuclides ^{208}Pb (stable), ^{208}Tl ($T_{1/2}$ = 3.053 min), and ^{220}Rn ($T_{1/2}$ = 55.6 s) were measured. The storage times varied from 0.2 to 9 s. Due to the low resolving power, the ions of the nuclides ^{208}Pb and ^{208}Tl were not resolved in measured mass spectra. These nuclides were treated as a single ion species because their

expected temporal behavior on the scale of investigated storage times is practically the same.

Results are shown in Fig. 5.5. The solid curves represent the expected temporal behavior of the data: an exponential decay curve with a fixed $T_{1/2}$ of 55.6 s for the ^{220}Rn isotope and a constant line for the combination of the nuclides ^{208}Pb and ^{208}Tl. For both data sets, measured data points are in good agreement with the expected behavior.

The non-nuclear-decay losses were estimated by implementing an additional exponential decay component to the fitted functions. The half-lives of the nuclear decays were fixed to the literature values, and the half-lives of the non-nuclear decays were obtained from the fit results. The values obtained for the non-nuclear-decay half-lives are in the order of a few hundreds of seconds, which proves that such losses are negligible for the storage times of up to 10 s used in this work.

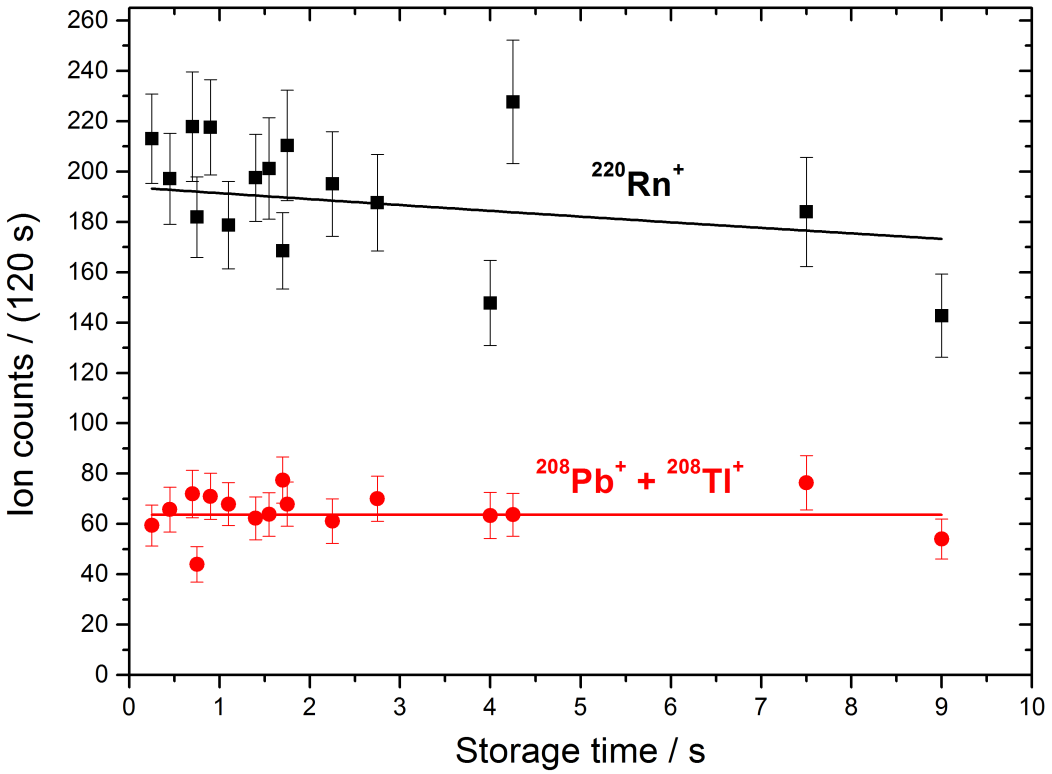

Figure 5.5: Measured ion counts of the nuclide ^{220}Rn and the sum of the nuclides ^{208}Pb and ^{208}Tl as the function of the CSC storage time. Solid curves represent fitted expected temporal behavior: ^{220}Rn$^+$ counts are fitted with an exponential decay curve with a fixed half-life of 55.6 s; the summed counts of ^{208}Pb$^+$ and ^{208}Tl$^+$ are fitted with a constant line. Results indicate negligible non-nuclear-decay losses for the investigated range of storage times.

These results also demonstrate the good cleanliness of the CSC. Assuming that collisions of the ions are dominated by the polarization of the buffer gas [Dehmelt, 1967], the ion collision rate with the helium atoms for the given experimental conditions can be estimated to be $\sim$ 3 GHz. The half-life of the non-nuclear losses of a few hundreds of seconds corresponds to the rate of collisions with the contaminant ions, in which the ions are lost, of a few millihertz. This indicates that the relative amount of harmful impurities with a low ionization potential in the buffer gas must be lower than 10^{-11}, which is in good agreement with previous measurements of the CSC cleanliness [Ranjan et al., 2015].

5.2.3 Measurement of half-life of ^{216}Po

To test the method for the measurement of half-lives, the nuclide ^{216}Po was used. ^{216}Po is produced by the internal ^{228}Th source. It undergoes α-decay to ^{212}Pb and has the literature half-life of (145 ± 2) ms. Alpha decay to ^{212}Pb is the only decay channel of ^{216}Po, which has a positive Q-value. A mass spectrum of the nuclides ^{216}Po and ^{212}Pb measured with the MR-TOF-MS in TFS mode is shown in Fig. 5.6. The red curve represents the overall fit to both peaks obtained using the analysis procedure described in Section 2.3. Small amounts of molecular contaminants produced by ionization can be also seen in the spectrum. The contaminants were not included in the fitting procedure. Similar spectra were measured for different storage times in the CSC and were analyzed in order to extract the abundances of measured nuclides.

The idea of the measurement was to store the ion bunches produced by the pulsed ^{228}Th source in the CSC for different durations, to demonstrate simultaneous decay of the mother nuclide ^{216}Po and corresponding growth of the daughter nuclide ^{212}Pb, and to measure the half-life of ^{216}Po. Storage times of up to 1 s were used. Here, the storage time is defined as the time difference between the temporal midpoint of the ion bunch emitted from the ^{228}Th source and the pulsing down of the extraction nozzle to allow ion extraction. ^{212}Pb has a half-life of 10.64 h, which is relatively long compared to the investigated storage times. Therefore, for the global fit of the data, Eq. (5.3) was used instead of Eq. (5.2) (see Subsection 5.1.4).

To the measured counts, certain corrections had to be applied. First, as discussed in Subsection 5.1.2, for alpha decays that occurred at the RF carpet, the efficiency of the recapturing of recoils is only 50 %. Therefore, ^{212}Pb counts had to be corrected accordingly for the fraction of the storage time that ions spent at the RF carpet surface. This time was calculated by subtracting the time that ions needed to reach the RF carpet (defined from ion mobility) from the storage time used in the measurement. The second correction originated from the problems with the RF carpet operation and the increased extraction time uncertainty discussed in Section 2.4. For storage times bellow 200 ms, a certain fraction of the ions was not extracted in the correct measurement cycle and was effectively stored in the CSC for an additional second. This lead to a decreased amount of ^{216}Po counts and increased amount of ^{212}Pb counts. In addition, dead-time effects in the DAQ had to be taken into account, as the off-line

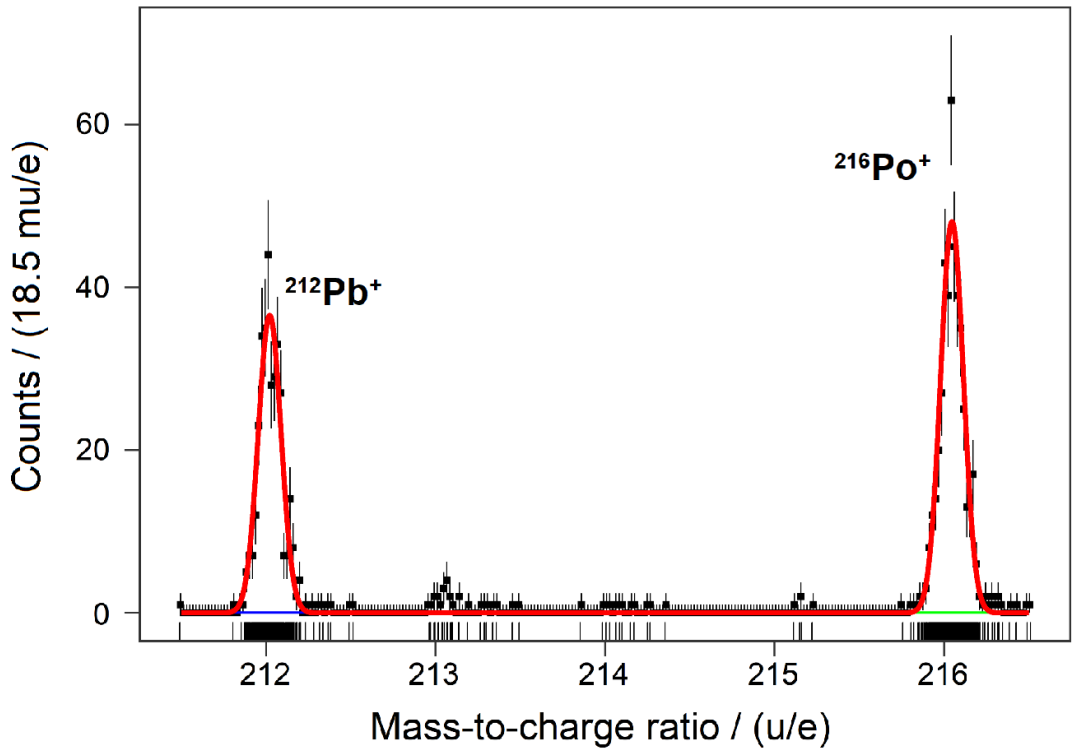

Figure 5.6: Mass spectrum of the nuclides ^{216}Po and ^{212}Pb measured with the MR-TOF-MS in TFS mode. The nuclei were produced by the ^{228}Th recoil source installed inside the CSC. The red curve represents the overall fit of both peaks. Molecular contaminants of smaller abundances are not included in the fitting procedure. The un-binned data are shown below the baseline of the spectrum.

source was generating a significant amount of ions that were extracted and detected in one MR-TOF-MS cycle. All mentioned corrections were estimated and applied to the measured data together with the corresponding uncertainties.

Results of the measurement are shown in Fig. 5.7. ^{216}Po and ^{212}Pb counts are plotted normalized to their sum. Data points were fitted with the global fit using Eq. (5.1) and Eq. (5.3). It can be clearly seen that the trends of the two data sets correspond to the decay of the mother nuclide and the growth of the daughter nuclide. From the global fit, a half-life value for ^{216}Po of (145 ± 11) ms is obtained, which agrees well with the literature value of (145 ± 2) ms [Audi et al., 2017].

In order to estimate the uncertainty improvement brought by the global fit, normalized ^{216}Po data points were also fitted to Eq. (5.1) independently. The half-life value obtained from the fit results is (158 ± 15) ms. It is consistent with the value obtained from the global fit, but has a larger uncertainty. An independent fitting was also done to the non-normalized counts of ^{216}Po. This gave a consistent result with a similar uncertainty. The advantage of using the global fit, which improves the statistics by taking into account both, mother and daughter nuclides, is evident.

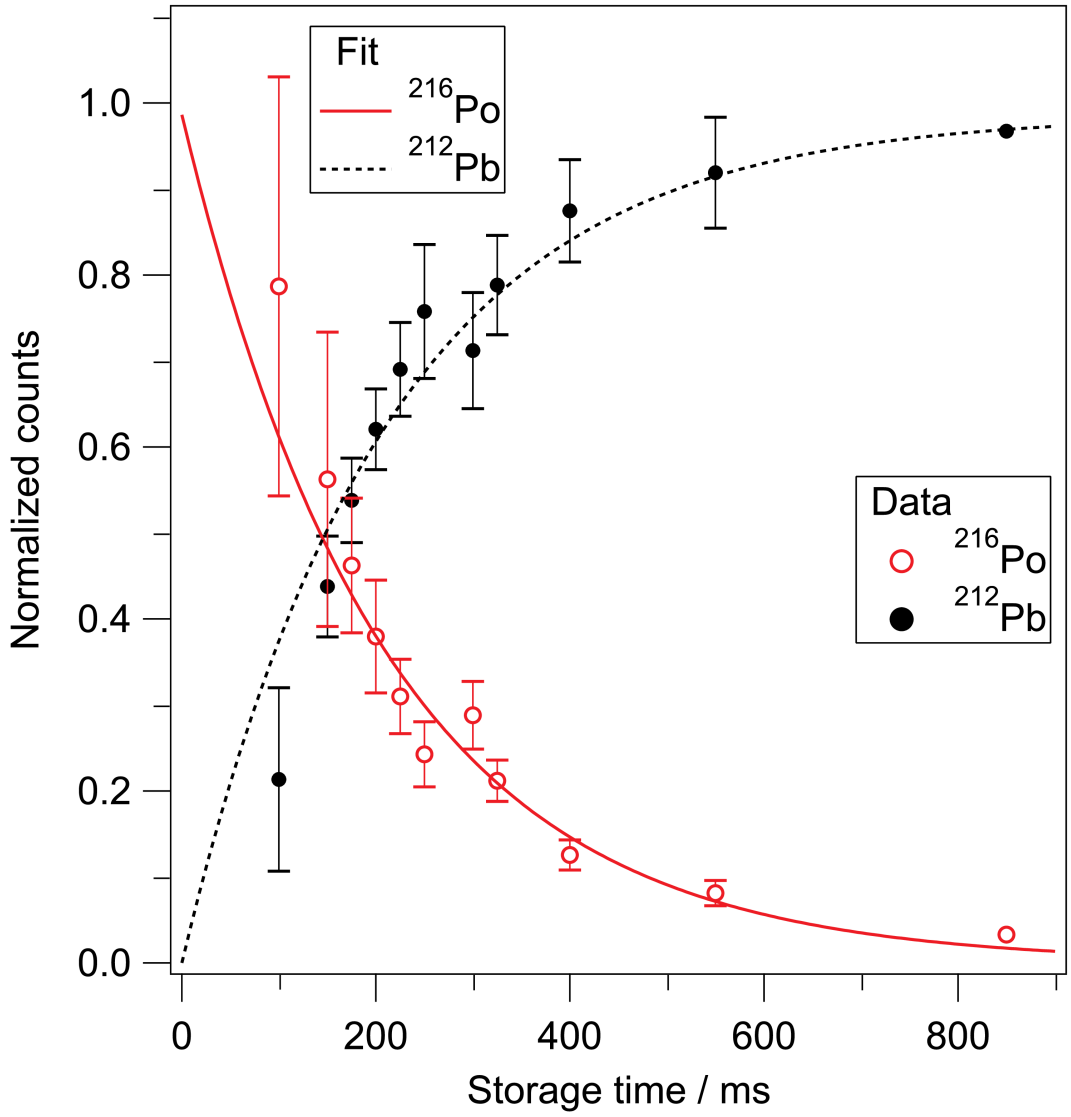

Figure 5.7: Measured counts of the nuclides ^{216}Po and ^{212}Pb for different storage times in the CSC. Normalization of counts is done to their sum. The lines represent a global fit to both data sets using Eq. (5.1) and Eq. (5.3). From the global fit, a half-life for ^{216}Po of (145 ± 11) ms is obtained, which agrees well with the literature value of (145 ± 2) ms.

5.3 Measurement of ^{119}Sb and its isomer

The method was also tested during the beam time at GSI in 2016 for the measurement of a half-life and decay branching ratios of the ^{119m2}Sb isomer [Miskun et al., 2019]. The measurement was done during the first experimental block with fragments produced by ^{238}U primary beam impinging on a beryllium target. Experimental conditions were as described in Section 2.4 with the only difference of shorter ion spills of 200 ms. Short spills coming from the SIS-18 were separated by relatively long breaks ($\sim$ 10 s) in order to allow long storage times in the CSC. Due to the low energy of the primary beam, the separation of fragments in the FRS was not optimal, which resulted in increased statistical uncertainties. Rates of the fragments stopped in the CSC were in the order of 10^3 ions per second, which is, according to Section 4.1, well below the rate threshold corresponding to the onset of space charge effects and to a drop in extraction efficiency of the CSC.

5.3.1 First direct mass measurements and spin assignment for the ^{119m2}Sb isomer

For the ^{119m2}Sb isomer, it is energetically possible to undergo different decays. It can decay by β^+-decay to the nuclide ^{119}Sn, by β^--decay to the nuclide ^{119}Te, and by γ-decay to the ground state ^{119g}Sb. Due to the non-optimal fragment separation in the FRS, all these nuclides and states were produced and transported to the FRS Ion Catcher, stopped in the CSC and measured with the MR-TOF-MS. In Figure 5.8, a measured mass-to-charge spectrum of stopped and extracted fragments is shown. Both nuclides ^{119}Te and ^{119}Sn have long-lived isomeric states (^{119m}Te with an excitation energy of 260.96 keV and a half-life of 4.7 days; ^{119m}Sn with an excitation energy of 89.531 keV and a half-life of 293.1 days) [Audi et al., 2017]. These isomers were not resolved during the measurement, because of the resolving power limitations for ^{119m}Sn and because of the low accumulated statistics for ^{119m}Te. Therefore, the counts of ^{119}Sn and ^{119}Te were fitted with single peaks assuming that only their ground states were populated.

The MR-TOF-MS was operated with a mass resolving power of 290,000. As it can be seen from the spectrum, the peaks of ^{119}Sn and ^{119g}Sb are not fully separated, just as the peaks of ^{119}Te and ^{119m2}Sb. The mass value and abundance of each peak were determined by using the Hyper-EMG function [Purushothaman et al., 2017a] obtained from the calibrant peak. The fits to each separate peak are shown in Fig. 5.8 in different colors, whereas the overall fit is represented by the red curve. The use of the Hyper-EMG proved to be crucial for the analysis, because with its help also the abundances of strongly-overlapping peaks could be measured very accurately.

As it was already discussed in the outline of the method, one of its important advantages is that during the measurement of half-life and decay branching ratios also the masses of mother and daughter nuclides are measured. From mass values, it is

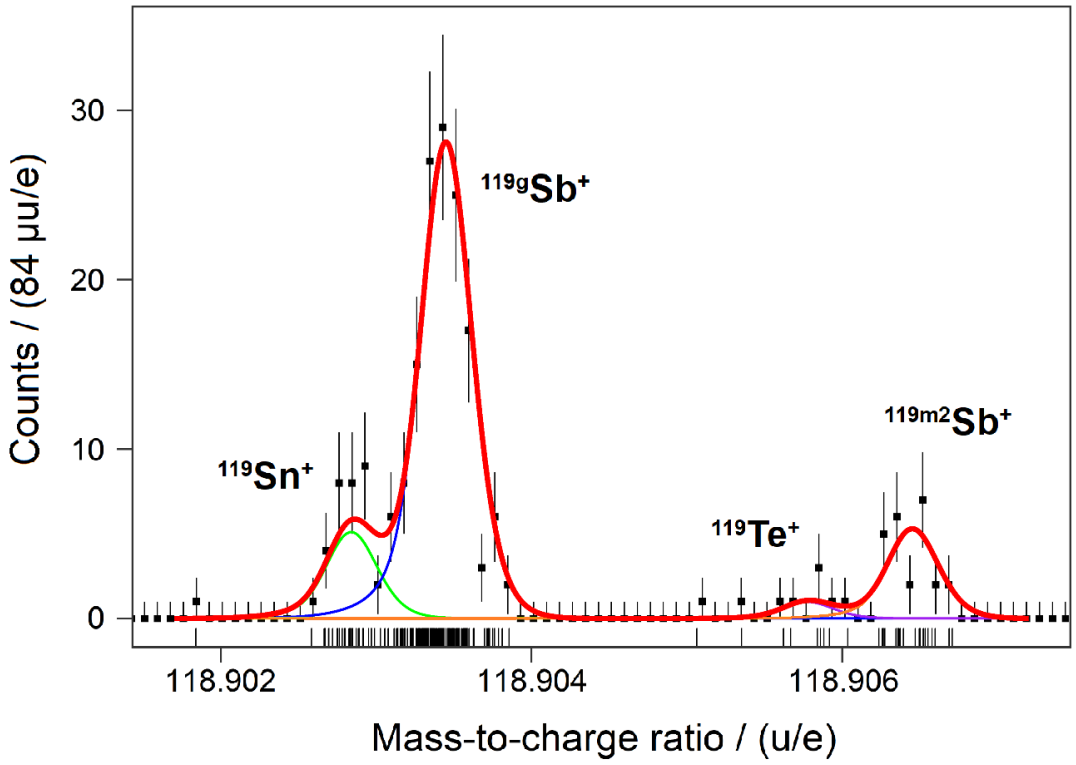

Figure 5.8: Mass spectrum of the nuclides ^{119m2}Sb, ^{119g}Sb, ^{119}Sn, and ^{119}Te measured with the MR-TOF-MS. The nuclides were produced in the FRS at an energy of 300 MeV/u. The mass resolving power of the MR-TOF-MS was 290,000. The red curve represents the overall fit of all peaks; the green, blue, orange, and pink curves represent fits to the peaks of the individual nuclides. The un-binned data are shown below the baseline of the spectrum.

possible to deduce isomers excitation energies, Q-values of nuclear reactions, one- and two-nucleon separation energies, etc.

In this work, the masses of the nuclides ^{119m2}Sb, ^{119g}Sb, ^{119}Sn, and ^{119}Te have been measured. The mass of the nuclide ^{119g}Sb and the excitation energy of the ^{119m2}Sb isomer have been measured directly for the first time. The results are compiled in Table 5.1. The measurement was done with 560 isochronous turns in the MR-TOF-MS, which correspond to the total time-of-flight of ions of 18.9 ms. For the calibration, the ion $^{12}C_2{}^{19}F_5^+$ ($A = 119$) was used. The measured masses of the nuclides ^{119g}Sb, ^{119}Sn, and ^{119}Te are in good agreement with the literature values published in the Atomic Mass Evaluation (AME2016) [Wang et al., 2017]. The measured excitation energy of the ^{119m2}Sb isomer is smaller than the one given in the Atlas of nuclear isomers [Jain et al., 2015]. The detailed discussion on this result follows in the next paragraphs.

^{119m2}Sb, the second isomeric state of ^{119}Sb with a half-life of (850 ± 90) ms, was first discovered in 1979 [Shroy et al., 1979]. However, its excitation energy and spin assignment are still not clearly identified. Several gamma spectroscopy experiments [Shroy et al., 1979, Lunardi et al., 1987, Porquet et al., 2005, Moon et al., 2011] indicated different results. Possible reasons for this are the complexity of a gamma spectrum, multiple γ-rays at almost the same energy, and the existence of another isomeric state with the excitation energy of (2553.6 ± 0.3) keV. The Atlas of nuclear isomers [Jain et al., 2015] and the Evaluated Nuclear Structure Data File (ENSDF) [Symochko et al., 2009], give the following adopted values for ^{119m2}Sb: excitation energy of $(2841.7 \pm 0.4 + x)$ keV, where x is to be determined; spin and parity of $27/2^+$. For the 2841.7 keV level, the adopted spin assignment is $I^\pi = 21/2^-$ [Symochko et al., 2009].

In this work, the excitation energy of ^{119m2}Sb has been measured directly for the first time. The obtained value of (2799 ± 30) keV (see Table 5.1) is 1.4 σ lower than the adopted value of $(2841.7 \pm 0.4 + x)$ keV. This result indicates that the unknown x parameter must be consistent with 0 and that the 2841.7 keV level itself is the long-lived isomeric state, as it was originally proposed in [Lunardi et al., 1987] and later adopted in [Porquet et al., 2005]. Both of these gamma-spectroscopy experiments assigned $I^\pi = 25/2^+$ to the 2841.7 keV level based on the conversion coefficient value of the 288.2 keV transition depopulating the isomer. Therefore, the results obtained in this work confirm the ^{119m2}Sb isomeric state designation of [Lunardi et al., 1987] and [Porquet et al., 2005] and contradict the adopted assignment [Jain et al., 2015, Symochko et al., 2009].

Nuclide	$T_{1/2}$	ME_{FRS-IC} $E_{exc,\ FRS-IC}$ / keV	ME_{AME16} $E_{exc,\ lit}$ / keV	ME_{FRS-IC} - ME_{AME16} $E_{exc,\ FRS-IC}$ - $E_{exc,\ lit}$ / keV	Number of events measured
^{119g}Sb	(38.19 ± 0.22) h	-89482 ± 17	-89474 ± 8	-8 ± 19	857
^{119m2}Sb	$T_{1/2,\ lit} = (850 \pm 90)$ ms $T_{1/2,\ FRS-IC} = (776 \pm 181)$ ms*	2799 ± 30	2841.7 ± 0.4 + x	-43 ± 30	467
^{119}Sn	stable	-90100 ± 36	-90065.0 ± 0.7	-35 ± 36	237**
^{119}Te	(16.05 ± 0.05) h	-87310 ± 177	-87181 ± 8	-129 ± 177	25**

Table 5.1: Results of mass measurements performed at the FRS Ion Catcher [Miskun et al., 2019]. The uncertainties of the measured values reflect the total experimental uncertainty. Literature values are taken from [Audi et al., 2017, Jain et al., 2015, Symochko et al., 2009, Wang et al., 2017]. For ground states of the nuclides, the values of mass excess (ME) are given; for the ^{119m2}Sb isomeric state, the excitation energy E_{exc} is given. The literature values of the nuclides ^{119}Sn and ^{119}Te are given for their ground states.
* Both literature and measured values are given.
** Total number of events for the unresolved ground and isomeric states.

5.3.2 Half-life and decay branching ratios of ^{119m2}Sb

For the measurement of half-life and decay branching ratios, the ions were stored for a duration of up to 1.5 s. Here, the storage time is defined as the time difference between the temporal midpoint of the beam spill entering the CSC and the pulsing down of the extraction nozzle to allow ion extraction. The results are shown in Fig. 5.9. The counts of all nuclides are plotted normalized to their sum. All possible daughters of ^{119m2}Sb have half-lives much longer than the half-life of the mother nuclide and the maximum investigated storage duration: $T_{1/2}$ (^{119g}Sb) = (39.19 ± 0.22) h, $T_{1/2}$ (^{119}Sn) = stable , $T_{1/2}$ (^{119}Te) = (16.05 ± 0.05) h. Therefore, the global fit using Eq. (5.1) for the mother nuclide and Eq. (5.3) for all possible daughters was applied to the data. The results of the global fit are given in Table 5.2. The half-life obtained for the ^{119m2}Sb isomer is (784 ± 203) ms, which is consistent with the literature value of (850 ± 90) ms. The results indicate that ^{119g}Sb is the only daughter nuclide populated from the mother nuclide decay. The decay branching ratios of β^+- and β^--decays are consistent with 0, which results in a constant temporal behavior of ^{119}Te and ^{119}Sn counts. This is the first experimental proof that the ^{119m2}Sb isomer decays only via internal transition. In γ-spectroscopy experiments, the transitions indicating β^+- and β^--decays were not observed, whereas, in the results of this work, it is positively shown that there is no population of β^+- and β^--decay daughter nuclides. In addition, from the results of the global fit, the isomer-to-ground ratio (IR) can be calculated as $IR = y_{01}/A_P$. For the ^{119}Sb fragments, the obtained IR is equal to 0.7 ± 0.3.

The global fit applied to the counts of all measured nuclides is not optimal for the determination of the half-life of ^{119m2}Sb. As it is shown above, the nuclides ^{119}Sn and ^{119}Te have no physical connection to the decay of ^{119m2}Sb. Therefore, their contribution to the global fit not only does not reduce the uncertainties but also results in additional noise and increased errors of the fitted parameters. In order to obtain the measured half-life of the mother nuclide with the smallest uncertainty, only the counts of actual daughter nuclides with a finite branching ratio should be included in the global fit. If using only the data sets of ^{119m2}Sb and ^{119g}Sb, the global fit gives a half-life value for the ^{119m2}Sb isomer of (776 ± 181) ms, which is still consistent with the literature value, but has a smaller uncertainty than the value given in Table 5.2.

^{119m2}Sb	A_P	0.48 ± 0.08
	$T_{1/2}$ / ms	784 ± 203
^{119g}Sb	y_{01}	0.33 ± 0.12
	n_{r1}	0.99 ± 0.51
^{119}Sn	y_{02}	0.19 ± 0.12
	n_{r2}	0.00 ± 0.45
^{119}Te	y_{03}	0.00 ± 0.02
	n_{r3}	0.01 ± 0.08

Table 5.2: Results of the global fit to the ^{119m2}Sb isomer decay and its all possible daughter nuclides population. In the fit, Eq. (5.1) and Eq. (5.3) were used.

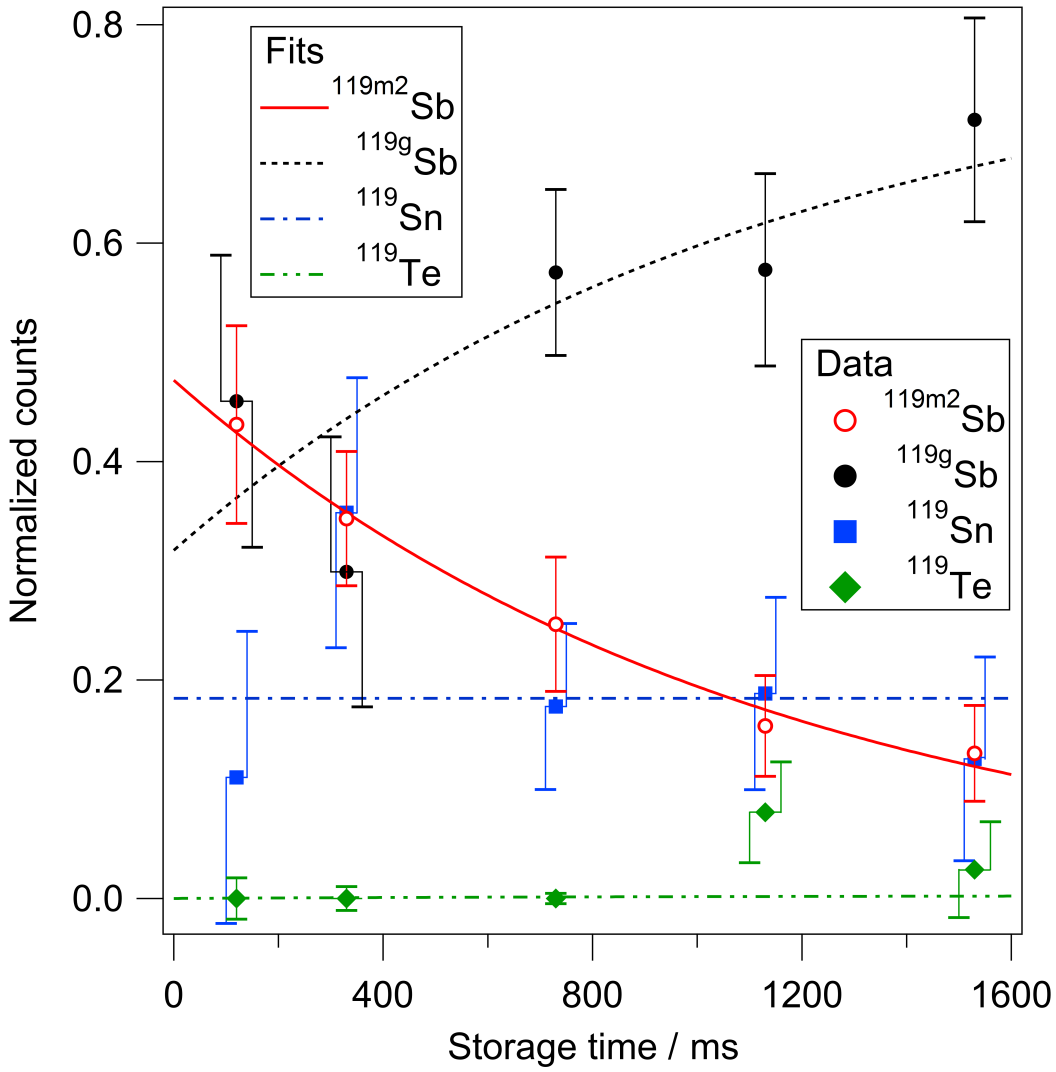

Figure 5.9: Measured counts of the nuclides ^{119m2}Sb, ^{119g}Sb, ^{119}Sn, and ^{119}Te for different storage times in the CSC. Normalization of counts is done to their sum. The lines represent a global fit to all data sets using Eq. (5.1) and Eq. (5.3). From the global fit, a half-life for ^{119m2}Sb of (784 ± 203) ms is obtained, which agrees well with the literature value of (850 ± 90) ms.

5.4 Dynamic storage of ions in the bulk of the stopping cell

As it was demonstrated in the previous sections, the developed method is very powerful for the determination of half-lives and decay branching ratios of exotic nuclei. Implemented at the FRS Ion Catcher, it yields a great potential for future experiments with exotic nuclei. In this section, further improvement of the measurement technique is discussed.

Simultaneous retrapping and measurement of all decay products together with the mother nuclide is one of the most important advantages of the developed method. However, for the reasons explained in Subsection 5.1.2, in order to efficiently recapture the recoils of all decay types, it is important to ensure that the decays happen in the bulk of the stopping gas, away from the electrodes of the CSC. For this, a new concept of dynamic storage of ions inside the CSC has been developed. The idea of this concept is to minimize the time that the ions spend close to the electrodes of the CSC (rings of the DC cage, the RF carpet) by actively switching the DC push field and guiding the ions into the bulk of the stopping gas and away from the electrodes.

The dynamic storage of ions is done in three steps. In the first step, a short ion spill of a few milliseconds is thermalized in the CSC, transported to the RF carpet within the full extraction time (~ 50 ms) and bunched near to the extraction nozzle, which is pulsed to high potential in order to block the extraction of the ions. In the second step, the DC push field is switched to a small negative value, which drags the ions away from the RF carpet surface into the bulk of the helium stopping gas. In less than 10 ms, the ions are already at a distance of about a centimeter away from the electrodes and are safe to undergo decay with full efficiency for the recapture of recoils. The ions then diffuse and drift in the weak electric field in the stopping volume of the CSC for a controllable duration. In the third step, the DC push field is switched back to a large positive value, the ions are transported to the RF carpet and extracted out of the CSC.

This concept was tested in simulations performed with the software packages SIMION [Dahl, 2000, Manura and Dahl, 2006] and ITSIM [Plaß, 2001, Wu et al., 2006, Plaß et al., 2008b]. Electric potential distributions for the electrode geometry resembling the real system were calculated in SIMION. These distributions were then imported in the ITSIM software, where ion trajectories were calculated taking into account the electric fields and the interaction of the ions with the buffer gas. The following experimental conditions were used in the simulations: helium buffer gas of 155 mbar at 80 K, corresponding to a density of 100 μg/cm^3; the RF carpet was operated with a repelling RF voltage of 120 $V_{peak-peak}$ at 6 MHz and 4 V/cm focusing DC field; the DC push field was switched between 10 V/cm and -0.5 V/cm. Ions with a mass-to-charge ratio of 219 u/e were used. The simulations were done using a macroscopic collision model, which describes the ion motion in a gas medium in terms of ion mobility and diffusion. The reduced ion mobility of 17.5 cm^2/(V·s) was used [Viehland, 2012]. The

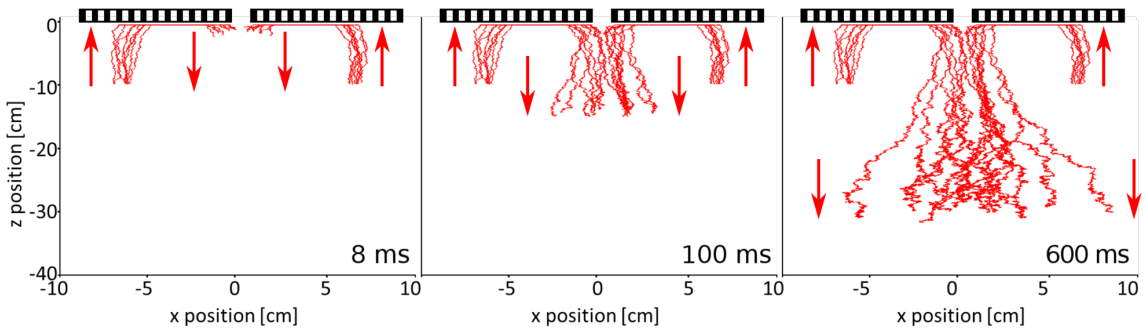

Figure 5.10: Ion trajectories during the dynamic storage in the CSC simulated with ITSIM. The RF carpet is shown as a hash in black; ion trajectories are plotted in red; arrows indicate the direction of ion motion. Ions are thermalized, transported to the RF carpet and bunched at the nozzle as the first step. The switched DC push field drags the ions away from the RF carpet into the bulk of the stopping gas in the second step. Left panel – 8 ms into the second step; middle panel – 100 ms into the second step; right panel – 600 ms into the second step. At 8 ms into the second step, the ions are already at a distance of $\sim$ 1 cm away from the RF carpet surface.

model and simulation parameters were validated with experimental results [Reiter, 2015, Rink, 2017].

Simulated ion trajectories are shown in Fig. 5.10. Each panel represents the downstream section of the CSC. The vertical axis z corresponds to the longitudinal dimension of the CSC (105 cm long) with the RF carpet positioned at $z = 0$. The horizontal axis x corresponds to the radial dimension of the CSC (25 cm in diameter) with the extraction nozzle positioned at $x = 0$. The RF carpet is shown as a hash, its dimensions, as well as the dimensions of the extraction nozzle, are not to scale. The trajectories are plotted in red and the arrows indicate the direction of ion motion. The trajectories of ions coming towards the RF carpet and away from it were separated in the simulations for better visual representation. The first panel shows the ion trajectories during the end of the first step and the beginning of the second step. After 8 ms from the moment of switched DC push field, the ions are already at a distance of $\sim$ 1 cm away from the RF carpet surface. The second and third panels show the trajectories at 100 ms and 600 ms into the second step. As can be seen from the simulations results, the ions slowly drift and diffuse in the dense stopping gas and weak electric field. However, after a certain time ($\sim$ 1 s), the ions might reach the walls of the inner chamber, so if longer storage times are required the first and the second steps can be repeated. Results indicate that the dynamic storage of the ions allows keeping them away from the electrodes for the largest part of the duty cycle, such that the recoils of all decay types are retrapped with full efficiency.

Summary

In this doctoral work, a novel method for simultaneous measurement of masses, isomer excitation energies, half-lives, and decay branching ratios of exotic nuclei has been developed, implemented, and used at the FRS Ion Catcher (FRS-IC) experiment [Plaß et al., 2013a] located at the GSI accelerator facility in Darmstadt, Germany. The method utilizes the advantages of in-flight production and separation of exotic nuclei at relativistic energies in the fragment separator (FRS) [Geissel et al., 1992a], controllable storage of the ions of interest and retrapping of their decay recoils in a gas-filled cryogenic stopping cell (CSC) [Ranjan et al., 2011, Reiter, 2015], and fast, accurate and broadband measurement with a multiple reflection time-of-flight mass spectrometer (MR-TOF-MS) [Plaß et al., 2008a, Dickel, 2010, Dickel et al., 2015b].

The feasibility of the method has been demonstrated in pilot measurements with the FRS Ion Catcher [Miskun et al., 2019]. The measurements have been performed with the nuclide ^{216}Po produced by an internal α-recoil source and with the nuclide ^{119}Sb and its isomer produced by fragmentation of ^{238}U primary beam at an energy of 300 MeV/u. It has been shown that the ions can be stored in the CSC for controllable durations of up to 10 seconds without non-nuclear-decay losses. The α-decay of ^{216}Po and the internal transition of the ^{119m2}Sb isomer produced in the FRS have been investigated by observing simultaneous decay of the mother nuclides and growth of the daughter nuclides. The measured half-life value for ^{216}Po of (145 ± 11) ms is consistent with the literature value of (145 ± 2) ms; and the measured half-life of ^{119m2}Sb of (776 ± 181) ms is consistent with the literature value of (850 ± 90) ms. For the ^{119m2}Sb isomer, for which it is energetically possible to undergo three different types of decay, the decay branching ratios have been measured directly for the first time. It has been experimentally confirmed that the isomer decays by internal transition, whereas the probabilities for β^+- and β^--decays are consistent with 0. The masses of the ground and isomeric states of ^{119}Sb have been measured directly for the first time, as well. Previously, the excitation energy and the spin assignment of the ^{119m2}Sb isomer had not been unambiguously established. The results of γ-ray spectroscopy experiments contradicted each other. In this work, it has been confirmed that the ^{119m2}Sb isomeric state has an energy level of 2841.7 keV, which supports the results reported in [Lunardi et al., 1987, Porquet et al., 2005], where the suggested spin assignment for this isomer is $I^\pi = 25/2^+$. The obtained results indicate that the adopted assignment [Jain et al., 2015, Symochko et al., 2009] for the excitation energy and the spin of ^{119m2}Sb is not correct.

In addition, within the frame of this thesis, a number of technical improvements and upgrades have been introduced to the FRS Ion Catcher setup. (i) A new calibration

^{228}Th recoil ion source has been installed inside the CSC. This source and a discharge source [Greiner, 2013a] have been extensively characterized. Ions produced by the internal sources can be used not only as calibrants for mass measurements with the MR-TOF-MS but also for off-line investigations and tests with the system, such as ion transport optimization, cleanliness tests, tuning of the high-resolution operation modes of the MR-TOF-MS, etc. (ii) The vacuum system has been upgraded, which, in combination with the extended RFQ beamline [Hornung et al., 2018], has resulted in higher possible areal densities of the CSC operation. The safe long-term operation of the CSC at areal densities of helium buffer gas of up to 10 mg/cm^2 has been demonstrated, which is almost a factor of two higher than in the past. The increase in the buffer gas areal density leads to the corresponding increase in the stopping efficiency of the CSC. (iii) In order to increase the selectivity of ion transport, two new techniques have been developed and implemented: the isolation-dissociation-isolation (IDI) method in the RFQ beamline [Greiner et al., 2019] and the separation by ion mobility at the RF carpet. These techniques are powerful tools for suppression of molecular contaminants, removal of unnecessary space charge from the transport beamline, and enhancing the cleanliness of measured spectra. The technical upgrades implemented to the FRS Ion Catcher in this work are an essential part of preparations for the upcoming experiments in the FAIR Phase-0 campaign [Plaß et al., 2019].

Also, in this work, characterization studies have been conducted. (i) The cleanliness of the CSC and the charge states of the thermalized and extracted ions have been investigated. It has been confirmed from the measurements of ions of more than 25 different chemical elements that the charge states are governed by the ionization potential of N_2 molecules, which are the dominant contaminant of the helium buffer gas in the present setup [Miskun et al., 2017]. (ii) Complementary to the work in [Reiter et al., 2016] rate capability studies of the CSC have been conducted. The obtained results are in good agreement with the former investigations. They also verify the simulation model used for calculation of the space charge effects in the CSC [Heiße, 2015] and show that their influence on the RF carpet performance in the present setup is negligible. (iii) In addition, the homogeneity of the matter in the beamline of the FRS has been studied with the FRS Ion Catcher. It has been observed that, for ^{238}U primary beam with an initial energy of 300 MeV/u, the measured width of the range distribution of the ions $\sigma = (7.8 \pm 0.4)$ mg/cm^2 is more than a factor of five larger than the calculated collisional straggling. The results indicate that the the range distribution of the ions for these experimental conditions is dominated by the contribution of the charge-exchange range straggling [Weick et al., 2002]. A thickness variation of the matter in the beamline of the FRS corresponding to $\sim 20 - 30$ μm of aluminum has also been measured.

Outlook

As it has been shown in this work, an important advantage of the novel method for the measurements of half-lives and decay branching ratios is that the nuclide identification and counting are done by direct mass measurement. This can provide independent and complementary information to the results of measurements performed by indirect methods, such as gamma spectroscopy. It can also be used for resolving debates about the spin assignment of excited states in complex cases, as it was demonstrated for the ^{119m2}Sb isomer. According to the Atlas of nuclear isomers [Jain et al., 2015], there are at least 20 other isomeric states in nuclides ranging from Co to Ra, for which excitation energies and spin assignments are still not defined unambiguously, and which are accessible, from their half-lives and excitation energies values, for the measurements with the FRS-IC.

A significant contribution of the developed method can be also expected for the measurements of β-delayed neutron emitters because, unlike the conventional methods, the method developed in this work does not rely on the detection of emitted neutrons, which gives rise to significant systematic uncertainties. This advantage is most prominent for the measurements of multi-neutron emission probabilities P_{xn} (x is the number of emitted neutrons, $x > 1$), where there is a strong need for new complementary measurement methods. The first experiment utilizing the novel method for the measurements of β-delayed neutron emission probabilities will be conducted in the FAIR Phase-0 campaign [Mardor et al., 2017, Plaß et al., 2019]. In addition, efficient recapturing of recoils of different decay types in the dense gas of a stopping cell allows high-accuracy studies of nuclides with multiple decay channels. An interesting example for possible investigations is the isomeric state of ^{94}Ag with an excitation energy of (6490 ± 500) keV (21^+, $T_{1/2} = 400$ ms), which can undergo one-proton and two-proton emission [Mukha et al., 2006], β^+-decay, and β-delayed one- and two-proton emission. At last, the concept of recapturing the decay recoils in the CSC and performing direct mass measurements with them can be extended to the production of exotic nuclei by fission [Balabanski et al., 2016, Mardor et al., 2018, Mardor et al., 2019] and by nuclear reactions [Dickel et al., 2018], which take place inside of the stopping cell.

In general, the method developed in this work is a powerful tool for investigations of nuclear properties of the numerous exotic nuclides with half-lives ranging from a few tens of milliseconds to a few tens of seconds. Further performance improvements of the FRS Ion Catcher and implementation of newly developed high-resolution and high transmission modes of the FRS [Haettner et al., 2019] will increase the reach of exotic nuclei towards smaller production cross sections. Together with the developed dynamic storage concept, it will enhance the potential of the novel method for the

measurements of half-lives and decay branching ratios with the FRS Ion Catcher. The method also opens up new possibilities for the investigations of the exotic nuclei contributing to the r-process at the future FAIR facility.

The characterization studies conducted in this work probe the technical limits of the existing stopping cell. The maximum extraction efficiency for the operation of the CSC at an areal density of the helium buffer gas of 10 mg/cm^2 is possible for heavy ions with a mass-to-charge ratio of $\sim$ 220 u/e at a mean extraction time of $\sim$ 55 ms. For lighter ions or for faster extraction times, the maximum extraction efficiency can be achieved at lower areal densities. At the same time, the measurements of the range distributions of the ions under the conditions similar to the ones which are going to be used at the future Low-Energy Branch of the Super-FRS at FAIR [Geissel et al., 2003, Winfield et al., 2013] indicate that even higher areal densities of the buffer gas are required for efficient stopping of the slowed-down relativistic ion beams. The results show that, even though the present CSC has the highest areal density world-wide among similar devices, there is a need for a new-generation stopping cell with even better performance characteristics. The design of the new CSC is already under development and has been reported in [Dickel et al., 2016, Plaß et al., 2018, Amanbayev et al., 2018]. The future setup will incorporate a number of novel concepts, which will allow operation at areal densities of up to $\sim$ 40 mg/cm^2, extraction times down to $\sim$ 10 ms and will be able to operate efficiently with rates of the incoming beams that are three orders of magnitude higher than possible with the existing setup. The next-generation CSC will meet the technical requirements of the Low-Energy Branch and enable measurements of even more exotic nuclei with MATS (precision measurements of very short-lived nuclei using an advanced trapping system for highly-charged ions) and LaSpec (laser spectroscopy of short-lived nuclei) [Rodriguez et al., 2010].

Zusammenfassung

Im Rahmen dieser Doktorarbeit wurde eine neuartige Methode zur gleichzeitigen Messung von Massen, Isomerenanregungsenergien, Halbwertszeiten und Zerfalls-Verzweigungsverhältnissen exotischer Kerne entwickelt, implementiert und eingesetzt am FRS Ion Catcher-Experiment an der GSI-Beschleunigeranlage in Darmstadt, Deutschland. Diese Methode nutzt die Vorteile der Produktion und Trennung exotischer Kerne bei relativistischen Energien im Fragmentseparator (FRS), die kontrollierte Speicherung der Ionen von Interesse und des Einfangs ihrer Tochterkerne in einer gasgefüllten kryogenen Stoppzelle (cryogenic stopping cell, CSC) und die schnelle, genaue und breitbandige Messung mit einem Multireflexions-Flugzeitmassenspektrometer (multiple reflection time-of-flight mass spectrometer, MR-TOF-MS).

Die Machbarkeit der Methode wurde in Pilotmessungen mit dem FRS-Ion-Catcher demonstriert. Diese Messungen wurden mit dem Nuklid ^{216}Po durchgeführt, das von einer internen Quelle erzeugt wurde, und mit dem Nuklid ^{119}Sb und seinem Isomer, die durch Fragmentation eines ^{238}U Primärstrahls bei einer Energie von 300 MeV/u erzeugt wurden. Es konnte gezeigt werden, dass die Ionen für eine wählbare Zeitdauer von bis zu 10 Sekunden in der CSC gespeichert werden können, ohne dass Verluste, abgesehen von radioaktiven Zerfällen, auftreten. Der α-Zerfall von ^{216}Po und die innere Konversion des im FRS produzierten ^{119m2}Sb-Isomers wurden durch die gleichzeitige Beobachtung des Zerfalls der Mutterkerne und des Wachstums der Tochterkerne untersucht . Der gemessene Wert der Halbwertszeit für ^{216}Po von (145 ± 11) ms stimmt mit dem Literaturwert von (145 ± 2) ms überein; und die gemessene Halbwertszeit von ^{119m2}Sb von (776 ± 181) ms stimmt mit dem Literaturwert von (850 ± 90) ms überein. Für das Isomer ^{119m2}Sb, für das drei verschiedene Zerfallsarten energetisch möglich sind, wurden die Zerfalls-Verzweigungsverhältnisse erstmals direkt gemessen. Es wurde experimentell bestätigt, dass das Isomer durch innere Konversion zerfällt, während die Wahrscheinlichkeiten für β^+- und β^--Zerfälle mit 0 übereinstimmen. Die Massen des Grundzustands und des Isomers von ^{119}Sb wurden ebenfalls zum ersten Mal direkt gemessen. Bisher waren die Anregungsenergie und die Spinzuordnung des ^{119m2}Sb-Isomers nicht eindeutig bestimmt worden. Die Ergebnisse von mehreren Gammaspektroskopie-Experimente widersprachen sich. In Rahmen dieser Doktorarbeit wurde bestätigt, dass das Isomer ^{119m2}Sb eine Anregungsenergie von 2841.7 keV hat, was die in [Lunardi et al., 1987, Porquet et al., 2005] angegebenen Ergebnisse unterstützt, in denen für dieses Isomer die Spinzuordnung $I^\pi = 25/2^+$ vorgeschlagen wird. Die in [Jain et al., 2015, Symochko et al., 2009] angenommene Zuordnung für die Anregungsenergie und den Spin von ^{119m2}Sb ist hingegen nicht korrekt.

Darüber hinaus wurden im Rahmen dieser Arbeit einige technische Verbesserun-

gen und Erweiterungen des FRS-Ion-Catcher-Exoeriments vorgenommen. (i) Im der CSC wurde eine neue ^{228}Th-Kalibrationsionenquelle installiert. Diese Quelle und eine Entladungsquelle wurden ausführlich untersucht und charakterisiert. (ii) Das Vakuumsystem wurde aufgerüstet, was in Kombination mit der erweiterten RFQ-Strahlführung zu einer höheren maximalen Flächendichte der CSC ermöglicht. Es wurde der sichere Langzeitbetrieb der CSC bei Flächendichten des Helium-Puffergases von bis zu 10 mg/cm^2 gezeigt; diese Flächendichte beträgt das zweifache des bisher erreichten Wertes. Die Erhöhung der Flächendichte führt zu einer entsprechenden Erhöhung der Stoppeffizienz der CSC. (iii) Um die Selektivität des Ionentransports zu erhöhen, wurden zwei neue Techniken entwickelt und implementiert: die Isolations-Dissoziations-Isolations (IDI) Methode in der RFQ-Strahlführung und die Ionenseparation am RF-Carpet durch die Ionenmobilität. Diese Techniken sind leistungsstarke Werkzeuge zur Unterdrückung molekularer Verunreinigungen, zum Entfernen unnötiger Raumladung aus der Strahlführung und zur Verbesserung der Sauberkeit der Massenspektren. Die durchgeführten Erweiterungen sind ein wesentlicher Teil der technischen Vorbereitungen für die anstehenden Experimente in der FAIR-Phase-0.

Die Sauberkeit der CSC und die Ladungszustände der thermalisierten und extrahierten Ionen von mehr als 25 verschiedenen chemischen Elementen wurden untersucht. Der Einfluss der Raumladung auf die Leistungsfähigkeit des RF-Carpets wurde untersucht und als vernachlässigbar gefunden. Darüber hinaus wurde die Homogenität der Materie im FRS mit dem FRS-Ion-Catcher untersucht.

Die in dieser Arbeit entwickelte neue Methode zur Messung von Halbwertszeiten und Zerfalls-Verzweigungsverhältnissen ist ein leistungsfähiges Instrument zur Untersuchung der Kerneigenschaften von zahlreichen exotischen Nukliden mit Halbwertszeiten zwischen einigen zehn Millisekunden und einigen zehn Sekunden. Das erste wissenschaftliche Experiment, das diese Methode für die Messung von Wahrscheinlichkeiten für β-verzögerte Neutronenemission verwendet, wird in FAIR-Phase-0 durchgeführt werden. Die neue Methode eröffnet auch neue Möglichkeiten in der zukünftigen FAIR-Beschleunigeranlage für die Untersuchung von exotischen Kernen, die am r-Prozess beteiligt sind.

Acknowledgments

It is my great pleasure to thank all the people who contributed to this work.

First and foremost, I would like to express my sincere gratitude to my advisors Prof. Dr. Christoph Scheidenberger and Prof. Dr. Dr. h.c. Hans Geissel for the opportunity of being a part of the IONAS group and working on such an exciting scientific topic. I am extremely grateful for their guidance and support throughout my doctoral study.

I would like to offer my special thanks to Dr. Wolfgang R. Plaß for his help in the preparation of this thesis, for sharing his valuable advice and constructive suggestions whenever they were needed. My grateful thanks are also extended to Dr. Timo Dickel for the day-to-day supervision and introducing me to the exciting world of experimental physics.

I would like to express my deep gratitude to Prof. Dr. Israel Mardor for very productive collaboration in working on the development of the novel method for the measurements of half-lives and branching ratios. His help with data analysis and publishing of the results has been very much appreciated. I want to thank Prof. Dr. M. Pascal Reiter for sharing his experience and knowledge with me and for being always a great example to follow. I would also like to thank Dr. Sivaji Purushothaman for giving a hand in taming the stopping cell and for his personal and professional advice and support.

Many thanks to all present and former members of the IONAS group and the FRS Ion Catcher collaboration who contributed to this work and brightened up my daily routine. I would particularly like to thank Dr. Samuel Ayet, Dr. Marcel Diwisch, Dr. Jens Ebert, Dr. Christine Hornung, Dr. Wayne Lippert, Dr. Ann-Kathrin Rink, Sönke Beck, Julian Bergmann, Florian Greiner, Lizzy Gröf, and Gabriella Kripko-Koncz. Special thanks to Daler Amanbayev, my good friend and colleague for backing me up in difficult moments, for patiently listening to my unstoppable flow of ideas and thoughts, and for his professional help in boosting up a visual aspect of my presentations and this thesis as well. I would also like to thank Dr. Egor Ovcharenko and Daria Kostyleva for their valuable support and encouragement.

I am deeply grateful to Evelin Prinz, Daniela Preß, and Luise Dörsching-Steitz for supporting me in bureaucratic battles. I would like to extend my thanks to Karl-Heinz Behr, Christos Karagiannis, Bogdan Szczepanczyk, and other members of the technical staff of the FRS/Super-FRS for helping me out in the lab with bigger and smaller problems a countless number of times. I also wish to acknowledge the help

provided by the mechanical workshops of JLU Giessen and GSI.

Special thanks to my good friends Maxim Yakovlev, Pavel Rozhkov, and Sachar Dunyavichev, who were there for me through the highs and lows. I greatly appreciate all the shared moments with them that always gave me motivation and strengths to keep going.

At last, I want to express my deepest heartfelt gratitude to my parents Irina and Aleksandr Miskun. Without their unwavering love, support, and profound belief in me, I would never be able to get that far. Thank you.

Bibliography

[Abbott et al., 2017] Abbott, B. P., Abbott, R., Abbott, T., Acernese, F., Ackley, K., Adams, C., Adams, T., Addesso, P., Adhikari, R., Adya, V., et al. (2017). GW170817: observation of gravitational waves from a binary neutron star inspiral. *Phys. Rev. Lett.*, 119(16):161101.

[Alfonso et al., 2015] Alfonso, M., Tereshatov, E., DeVanzo, M., Sefcik, J., Bennett, M., Mayorov, D., Werke, T., and Folden III, C. (2015). New recoil transfer chamber for thermalization of heavy ions produced in fusion–evaporation reactions. *Nucl. Instrum. Methods A*, 798:52–61.

[Amanbayev et al., 2018] Amanbayev, D., Ayet, S., Dickel, T., Geissel, H., Greiner, F., Miskun, I., Purushothaman, S., Plaß, W. R., Rink, A.-K., and Scheidenberger, C. (2018). Development of the stopping cell for the Low-Energy Branch of the Super-FRS. *GSI Sci. Rep. 2017*, 2018-1:117 p.

[Angert and Schmelzer, 1969] Angert, N. and Schmelzer, C. (1969). The UNILAC, a variable energy linear accelerator for atomic ions of any mass. *Kerntech.*, 11:690–695.

[Audi et al., 2017] Audi, G., Kondev, F. G., Wang, M., Huang, W. J., and Naimi, S. (2017). The NUBASE2016 evaluation of nuclear properties. *Chinese Phys. C*, 41(3):030001.

[Aumann, 2007] Aumann, T. (2007). Prospects of nuclear structure at the future GSI accelerators. *Prog. Part. Nucl. Phys.*, 59(1):3–21.

[Ayet San Andrés, 2018] Ayet San Andrés, S. (2018). *Developments for Multiple-Reflection Time-of-Flight Mass Spectrometers and Their Application to High-Resolution Accurate Mass Measurements of Short-Lived Exotic Nuclei*. PhD thesis, Justus Liebig University Gießen.

[Ayet San Andrés et al., 2019] Ayet San Andrés, S., Hornung, C., Ebert, J., Plaß, W. R., Dickel, T., Geissel, H., Scheidenberger, C., Bergmann, J., Greiner, F., Haettner, E., Jesch, C., Lippert, W., Mardor, I., Miskun, I., Patyk, Z., Pietri, S., Pihktelev, A., Purushothaman, S., Reiter, M. P., Rink, A.-K., Weick, H., Yavor, M. I., Bagchi, S., Charviakova, V., Constantin, P., Diwisch, M., Finlay, A., Kaur, S., Knöbel, R., Lang, J., Mei, B., Moore, I. D., Otto, J.-H., Pohjalainen, I., Prochazka, A., Rappold, C., Takechi, M., Tanaka, Y. K., Winfield, J. S., and Xu, X. (2019).

High-resolution, accurate multiple-reflection time-of-flight mass spectrometry for short-lived, exotic nuclei of a few events in their ground and low-lying isomeric states. *Phys. Rev. C*, 99:064313.

[Äystö and Jokinen, 2003] Äystö, J. and Jokinen, A. (2003). Ion beam coolers in nuclear physics. *J. Phys. B: At. Mol. Opt. Phys.*, 36:573–584.

[Balabanski et al., 2016] Balabanski, D. L., Ibrahim, F., Krasznahorkay, A., Boztosun, I., Choudhury, D., Coban, S., Constantin, P., Csige, L., Cuong, P. V., Dickel, T., Djapo, H., Dobrin, I., Essabaa, S., Filipescu, D., Franchoo, S., Georgiev, G., Gheorge, I., Ghita, D., Glodariu, T., Gupta, M., Jokinen, A., Kaur, J., Marginean, N., Marginean, R., Moore, I., Pentilla, H., Petcu, C., Plaß, W., Sava, T., Savard, G., Scheidenberger, C., and Yordanov, D. (2016). Photofission experiments at ELI-NP. *Rom. Rep. Phys.*, 68:621.

[Batchelor, 1967] Batchelor, G. K. (1967). *An Introduction to Fluid Dynamics*. Cambridge Mathematical Library. Cambridge University Press.

[Bateman, 1910] Bateman, H. (1910). Solution of a system of differential equations occurring in the theory of radioactive transformations. *Proc. Cambridge Philos. Soc.*, 15:423.

[Bentley, 1980] Bentley, P. D. (1980). The modern cryopump. *Vacuum*, 30:145–158.

[Bergmann, 2020] Bergmann, J. (2020). *In preparation*. PhD thesis, Justus Liebig University Gießen.

[Bethe, 1932] Bethe, H. (1932). Bremsformel für elektronen relativistischer Geschwindigkeit. *Zeitschrift für Physik*, 76(5-6):293–299.

[Blasche and Franczak, 1992] Blasche, K. and Franczak, B. (1992). The heavy ion synchrotron SIS. In *Proc. EPAC*, page 9.

[Bloch, 1933] Bloch, F. (1933). Zur Bremsung rasch bewegter Teilchen beim Durchgang durch Materie. *Annalen der Physik*, 408(3):285–320.

[Blumenfeld et al., 2013] Blumenfeld, Y., Nilsson, T., and Duppen, P. V. (2013). Facilities and methods for radioactive ion beam production. *Phys. Scr.*, 152:014023.

[Bohr, 1913] Bohr, N. (1913). II. On the theory of the decrease of velocity of moving electrified particles on passing through matter. *The London, Edinburgh, and Dublin Philosophical Magazine and Journal of Science*, 25(145):10–31.

[Bollen et al., 1992] Bollen, G., Kluge, H.-J., Otto, T., Savard, G., and Stolzenberg, H. (1992). Ramsey technique applied in a Penning trap mass spectrometer. *Nucl. Instrum. Methods B*, pages 490–493.

[Bosch et al., 1996] Bosch, F., Faestermann, T., Friese, J., Heine, F., Kienle, P., Wefers, E., Zeitelhack, K., Beckert, K., Franzke, B., Klepper, O., et al. (1996). Observation of bound-state β- decay of fully ionized ^{187}Re: ^{187}Re- ^{187}Os cosmochronometry. *Phys. Rev. Lett.*, 77(26):5190.

[Bradbury and Nielsen, 1936] Bradbury, N. E. and Nielsen, R. A. (1936). Absolute values of the electron mobility in hydrogen. *Phys. Rev.*, 49:388–393.

[Brown and Gabrielse, 1986] Brown, L. S. and Gabrielse, G. (1986). Geonium theory: Physics of a single electron or ion in a Penning trap. *Rev. Mod. Phys.*, 58(1):233–311.

[Brunner et al., 2013] Brunner, T., Lapierre, A., Andreoiu, C., Brodeur, M., Delheji, P., Ettenauer, S., Frekers, D., Gallant, A., Gernhäuser, R., Grossheim, A., et al. (2013). Trapped-ion decay spectroscopy towards the determination of ground-state components of double-beta decay matrix elements. *Eur. Phys. J. A*, 49(11):142.

[Brunner et al., 2012] Brunner, T., Mueller, A., O'Sullivan, K., Simon, M. C., Kossick, M., Ettenauer, S., Gallant, A. T., Mané, E., Bishop, D., Good, M., Gratta, G., and Dilling, J. (2012). A large Bradbury Nielsen ion gate with flexible wire spacing based on photo-etched stainless steel grids and its characterization applying symmetric and asymmetric potentials. *Int. J. Mass Spectrom.*, 309:97–103.

[Cameron and Eggers, 1948] Cameron, A. E. and Eggers, D. F. (1948). An ion "velocitron". *Rev. Sci. Instrum.*, 19:605–607.

[Dahl, 2000] Dahl, D. A. (2000). SIMION for the personal computer in reflection. *Int. J. Mass Spectrom.*, 200(1-3):3 – 25.

[Dawson, 1976] Dawson, P. H. (1976). *Quadrupole Mass Spectrometry and its applications*. Elsevier Scientific Publishing Company, Amsterdam-Oxford-New York.

[Dehmelt, 1967] Dehmelt, H. G. (1967). Radiofrequency spectroscopy of stored ions I: Storage. *Adv. At. Mol. Phys.*, 3:53–72.

[Dendooven, 1997] Dendooven, P. (1997). The development and status of the IGISOL technique. *Nucl. Instrum. Methods B*, 126(1-4):182–189.

[Dickel, 2010] Dickel, T. (2010). *Design and Commissioning of an Ultra-High-Resolution Time-of-Flight Based Isobar Separator and Mass Spectrometer*. PhD thesis, Justus Liebig University Gießen.

[Dickel et al., 2018] Dickel, T., Constantin, P., Winfield, J., Ayet San Andrés, S., Bagchi, S., Balabanski, D., Beck, S., Geissel, H., Greiner, F., Haettner, E., Hornung, C., Heinz, S., Kankainen, A., Karpov, A., Kostyleva, D., Kuzminchuk, N., Kindler, B., Lommel, B., Mardor, I., Martinez Pinedo, G., Miskun, I., Mukha, I., Münzenberg, G., Patyk, Z., Piasetzky, E., Pietri, S., Plaß, W. R., Pomerantz, I.,

Prochazka, A., Purushothaman, S., Rappold, C., Saito, T., Saiko, V., Scheidenberger, C., and Weick, H. (2018). Reaction studies with the FRS Ion Catcher: A novel approach and universal method for the production, identification of and experiments with unstable isotopes produced in multi-nucleon transfer reactions with stable and unstable beams. *GSI Sci. Rep. 2017*, 2018-1:112.

[Dickel et al., 2015a] Dickel, T., Plaß, W. R., Ayet San Andres, S., Ebert, J., Geissel, H., Haettner, E., Hornung, C., Miskun, I., Pietri, S., Purushothaman, S., Reiter, M. P., Rink, A. K., Scheidenberger, C., Weick, H., Dendooven, P., Diwisch, M., Greiner, F., Heiße, F., Knöbel, R., Lippert, W., Moore, I. D., Pohjalainen, I., Prochazka, A., Ranjan, M., Takechi, M., Winfield, J. S., and Xu, X. (2015a). First spatial separation of a heavy ion isomeric beam with a multiple-reflection time-of-flight mass spectrometer. *Phys. Lett. B*, 744:137–141.

[Dickel et al., 2015b] Dickel, T., Plaß, W. R., Becker, A., Czok, U., Geissel, H., Haettner, E., Jesch, C., Kinsel, W., Petrick, M., Scheidenberger, C., and Yavor, M. I. (2015b). A high-performance multiple-reflection time-of-flight mass spectrometer and isobar separator for the research with exotic nuclei. *Nucl. Instrum. Methods A*, 777:172–188.

[Dickel et al., 2016] Dickel, T., Plaß, W. R., Geissel, H., Heiße, F., Miskun, I., Purushothaman, S., Reiter, M. P., Rink, A.-K., and Scheidenberger, C. (2016). Conceptional design of a novel next-generation cryogenic stopping cell for the Low-Energy Branch of the Super-FRS. *Nucl. Instrum. Methods B*, 376:216–220.

[Dickel et al., 2017] Dickel, T., Yavor, M. I., Lang, J., Plaß, W. R., Lippert, W., Geissel, H., and Scheidenberger, C. (2017). Dynamical time focus shift in multiple-reflection time-of-flight mass spectrometers. *Int. J. Mass Spectrom.*, 412:1–7.

[Dillmann and Tarifeño-Saldivia, 2018] Dillmann, I. and Tarifeño-Saldivia, A. (2018). The beta-delayed neutrons at RIKEN project (BRIKEN): Conquering the most exotic beta-delayed neutron-emitters. *Nucl. Phys. News*, 28(1):28–31.

[Dodonov et al., 1997] Dodonov, A., Kozlovsky, V., Loboda, A., Raznikov, V., Sulimenkov, I., Tolmachev, A., Kraft, A., and Wollnik, H. (1997). A new technique for decomposition of selected ions in molecule ion reactor coupled with ortho-time-of-flight mass spectrometry. *Rapid Commum. Mass Spectrom.*, 11:1649–1656.

[Ebert, 2016] Ebert, J. (2016). *Mass Measurements of ^{238}U-Projectile Fragments for the First Time with a Multiple-Reflection Time-of-Flight Mass Spectrometer*. PhD thesis, Justus Liebig University Gießen.

[Eliseev et al., 2014] Eliseev, S., Blaum, K., Block, M., Dörr, A., Droese, C., Eronen, T., Goncharov, M., Höcker, M., Ketter, J., Ramirez, E. M., et al. (2014). A phase-imaging technique for cyclotron-frequency measurements. *Appl. Phys. B*, 114(1-2):107–128.

[Eliseev et al., 2013] Eliseev, S., Blaum, K., Block, M., Droese, C., Goncharov, M., Ramirez, E. M., Nesterenko, D. A., Novikov, Y. N., and Schweikhard, L. (2013). Phase-imaging ion-cyclotron-resonance measurements for short-lived nuclides. *Phys. Rev. Lett.*, 110:082501.

[Eronen et al., 2016] Eronen, T., Kankainen, A., and Äystö, J. (2016). Ion traps in nuclear physics – recent results and achievements. *Prog. Part. Nucl. Phys.*, 91:259 – 293.

[Evdokimov et al., 2012] Evdokimov, A., Dillmann, I., Marta, M., Bosch, F., Dolinskii, A., Kozhuharov, C., Litvinov, Y., Nolden, F., Steck, M., Weick, H., Faestermann, T., Gernhauser, R., and Maier, L. (2012). An alternative approach to measure β-delayed neutron emission. *Proc. of Science*, (NIC XII):115.

[Fermi, 1940] Fermi, E. (1940). The ionization loss of energy in gases and in condensed materials. *Phys. Rev.*, 57(6):485.

[Fick, 1855] Fick, A. (1855). Über Diffusion. *Annalen der Physik*, 170(1):59–86.

[Franzke, 1987] Franzke, B. (1987). The heavy ion storage and cooler ring project ESR at GSI. *Nucl. Instrum. Methods B*, 24/25:18–25.

[Franzke et al., 2008] Franzke, B., Geissel, H., and Münzenberg, G. (2008). Mass and lifetime measurements of exotic nuclei in storage rings. *Mass Spectrom. Rev.*, 27:428–469.

[Garcia et al., 2017] Garcia, F., Turpeinen, R., Äystö, J., Grahn, T., Rinta-Antila, S., Jokinen, A., Voss, B., Kunkel, J., Kleipa, V., Risch, H., Caesar, C., Simons, C., Prochazka, A., Schmidt, C. J., Hoffmann, J., I., R., and H., K. N. H. (2017). Twin GEM-TPC prototype (HGB4) beam test at GSI - a tracking detector for the Super-FRS. *GSI Sci. Rep. 2016*, 2017-1:475 p.

[Geissel et al., 1992a] Geissel, H., Armbruster, P., Behr, K. H., Brünle, A., Burkard, K., Chen, M., Folger, H., Franczak, B., Keller, H., Klepper, O., Langenbeck, B., Nickel, F., Pfeng, E., Pfützner, M., Roeckl, E., Rykaczewski, K., Schall, I., Schardt, D., Scheidenberger, C., Schmidt, K. H., Schröter, A., Schwab, T., Sümmerer, K., Weber, M., Münzenberg, G., Brohm, T., Clerc, H. G., Fauerbach, M., Gaimard, J. J., Grewe, A., Hanelt, E., Knödler, B., Steiner, M., Voss, B., Weckenmann, J., Ziegler, C., Magel, A., Wollnik, H., Dufour, J. P., Fujita, Y., Vieira, D. J., and Sherrill, B. (1992a). The GSI projectile fragment separator (FRS): a versatile magnetic system for relativistic heavy ions. *Nucl. Instrum. Methods B*, 70(1-4):286 – 297.

[Geissel et al., 1992b] Geissel, H., Beckert, K., Bosch, F., Eickhoff, H., Franczak, B., Franzke, B., Jung, M., Klepper, O., Moshammer, R., Münzenberg, G., et al. (1992b). First storage and cooling of secondary heavy-ion beams at relativistic energies. *Phys. Rev. Lett.*, 68(23):3412.

[Geissel et al., 1995] Geissel, H., Münzenberg, G., and Riisager, K. (1995). Secondary Exotic Nuclear Beams. *Annu. Rev. Nucl. Part. Sci.*, 45:163–203.

[Geissel et al., 1989] Geissel, H., Schwab, T., Armbruster, P., Dufour, J., Hanelt, E., Schmidt, K.-H., Scherrill, B., and Münzenberg, G. (1989). Ions penetrating through ion-optical systems and matter - non-Liouvillian phase-space modelling. *Nucl. Instrum. Methods A*, 282:247–260.

[Geissel et al., 2002] Geissel, H., Weick, H., Scheidenberger, C., Bimbot, R., and Gardes, D. (2002). Experimental studies of heavy-ion slowing down in matter. *Nucl. Instrum. Methods B*, 195(1-2):3–54.

[Geissel et al., 2003] Geissel, H., Weick, H., Winkler, M., Münzenberg, G., Chichkine, V., Yavor, M., Aumann, T., Behr, K. H., Böhmer, M., Brünle, A., Burkard, K., Benlliure, J., Cortina-Gil, D., Chulkov, L., Dael, A., Ducret, J.-E., Emling, H., Franczak, B., Friese, J., Gastineau, B., Gerl, J., Gernhäuser, R., Hellström, M., Jonson, B., Kojouharova, J., Kulessa, R., Kindler, B., Kurz, N., Lommel, B., Mittig, W., Moritz, G., Mühle, C., Nolen, J. A., Nyman, G., Roussell-Chomaz, P., Scheidenberger, C., Schmidt, K.-H., Schrieder, G., Sherrill, B., Simon, H., Sümmerer, K., Tahir, N. A., Vysotsky, V., Wollnik, H., and Zeller, A. F. (2003). The Super-FRS project at GSI. *Nucl. Instrum. Methods B*, 204:71–85.

[Geissel et al., 2013] Geissel, H., Winfield, J. S., Berg, G. P. A., Franczak, B., Iwasa, N., Münzenberg, G., Nociforo, C., Plaß, W. R., Scheidenberger, C., Weick, H., Winkler, M., and Yavor, M. (2013). Dispersion-matched spectrometer in the low-energy branch of the Super-FRS for high-resolution measurements with large-emittance relativistic fragment beams. *Nucl. Instrum. Methods B*, 317:277–283.

[Gräff et al., 1980] Gräff, G., Kalinowsky, H., and Traut, J. (1980). A direct determination of the proton electron mass ratio. *Z. Physik A*, 297:35–39.

[Greiner, 2013a] Greiner, F. (2013a). *Bauen und Testen einer Gasionisationsquelle.* Study project, Justus Liebig University Gießen.

[Greiner, 2013b] Greiner, F. (2013b). *Construction and Commissioning of an RF Quadrupole Switchyard (in German).* Bachelor thesis, Justus Liebig University Gießen.

[Greiner, 2017] Greiner, F. (2017). Collision-induced dissociation - an effective method for removing molecular contaminants in beams of short-lived nuclei (in German). Master thesis, Justus Liebig University Gießen.

[Greiner et al., 2019] Greiner, F., Dickel, T., San Andrés, S. A., Bergmann, J., Constantin, P., Ebert, J., Geissel, H., Haettner, E., Hornung, C., Miskun, I., Lippert, W., Mardor, I., Moore, I., Plaß, W. R., Purushothaman, S., Rink, A.-K., Reiter, M. P., Scheidenberger, C., and Weick, H. (2019). Removal of molecular contam-

ination in low-energy RIBs by the isolation-dissociation-isolation method. *Nucl. Instrum. Methods B*, in press.

[Gröf, 2017] Gröf, L. (2017). *Inbetriebnahme und erste Experimente mit einer Kalibrations-Ionenquelle für die Flugzeitmassenspektrometrie*. Bachelor thesis, Justus Liebig University Gießen.

[Haettner et al., 2019] Haettner, E., Franczak, B., Geissel, H., Dickel, T., Pietri, S., Plaß, W., Prochazka, A., Purushothaman, S., Scheidenberger, C., Tanaka, Y., Terashima, S., Weick, H., Winfield, J., and Yavor, M. (2019). New high-resolution and high-transmission modes of the FRS for FAIR phase-0 experiments. *Nucl. Instrum. Methods B*, in press.

[Haettner et al., 2018] Haettner, E., Plaß, W. R., Czok, U., Dickel, T., Geissel, H., Kinsel, W., Petrick, M., Schäfer, T., and Scheidenberger, C. (2018). A versatile triple radiofrequency quadrupole system for cooling, mass separation and bunching of exotic nuclei. *Nucl. Instrum. Methods A*, 880:138–151.

[Hausmann et al., 2000] Hausmann, M., Attallah, F., Beckert, K., Bosch, F., Dolinskiy, A., Eickhoff, H., Falch, M., Franczak, B., Franzke, B., Geissel, H., Kerscher, T., Klepper, O., Kluge, H.-J., Kozhuharov, C., Löbner, K. E. G., Münzenberg, G., Nolden, F., Novikov, Y. N., Radon, T., Schatz, H., Scheidenberger, C., Stadlmann, J., Steck, M., Winkler, T., and Wollnik, H. (2000). First isochronous mass specrometry at the experimental storage ring ESR. *Nucl. Instrum. Methods A*, 446:569–580.

[Heiße, 2015] Heiße, F. (2015). *Investigation of the cryogenic gas-filled stopping cell for the FRS Ion Catcher*. Master thesis, Technische Universität Dresden.

[Herlert et al., 2005] Herlert, A., Beck, D., Blaum, K., Carrel, F., Delahaye, P., George, S., Guénaut, C., Herfurth, F., Kellerbauer, A., Kluge, H., et al. (2005). Mass spectrometry of atomic ions produced by in-trap decay of short-lived nuclides. *New J. Phys.*, 7(1):44.

[Herlert et al., 2012] Herlert, A., Van Gorp, S., Beck, D., Blaum, K., Breitenfeldt, M., Cakirli, R. B., George, S., Hager, U., Herfurth, F., Kellerbauer, A., Lunney, D., Savreux, R., Schweikhard, L., and Yazidjian, C. (2012). Recoil-ion trapping for precision mass measurements. *Eur. Phys. J. A*, 48(7):97.

[Hornung, 2018] Hornung, C. (2018). *High-Resolution Experiments with the Multiple-Reflection Time-Of-Flight Mass Spectrometer at the Fragment Separator FRS*. PhD thesis, Justus Liebig University Gießen.

[Hornung et al., 2018] Hornung, C., Amanbayev, D., Ayet San Andrés, S., Bergmann, J., Dickel, T., Geissel, H., Greiner, F., Gröf, L., Plaß, W. R., Rink, A.-K., and Scheidenberger, C. (2018). An upgrade to the RFQ beam line of the FRS Ion Catcher. *GSI-FAIR Sci. Rep. 2017*, 2018-1:116 p.

[Iliadis, 2015] Iliadis, C. (2015). *Nuclear Physics of Stars*. Wiley-VCH Verlag GmbH & Co.

[ISOLDE, 2015] ISOLDE (2015). ISOLDE yield database.

[Iwasa et al., 1997] Iwasa, N., Geissel, H., Münzenberg, G., Scheidenberger, C., Schwab, T., and Wollnik, H. (1997). MOCADI, a universal Monte Carlo code for the transport of heavy ions through matter within ion-optical systems. *Nucl. Instrum. Methods B*, 126:284–289.

[Jain et al., 2015] Jain, A. K., Maheshwari, B., Garg, S., Patial, M., and Singh, B. (2015). Atlas of nuclear isomers. *Nucl. Data Sheets*, 128:1–130.

[Janik et al., 2011] Janik, R., Prochazka, A., Sitar, B., Strmen, P., Szarka, I., Geissel, H., Behr, K.-H., Karagiannis, C., Nociforo, C., Weick, H., and Winkler, M. (2011). Time projection chambers with C-pads for heavy-ion tracking. *Nucl. Intrum. Methods A*, 640:54–57.

[Javahery and Thomson, 1997] Javahery, G. and Thomson, B. (1997). A segmented radiofrequency-only quadrupole collision cell for measurements of ion collision cross section on a triple quadrupole mass spectrometer. *J. Am. Soc. Mass Spectrom.*, 8:697–702.

[Jesch, 2008] Jesch, C. (2008). *Injektions-Ionenfallensystem für ein Multireflektions-Flugzeitmassenspektrometer*. Diploma thesis, Justus Liebig University Gießen.

[Jesch, 2016] Jesch, C. (2016). *The Multiple-Reflection Time-of-Flight Isobar Separator for TITAN and Direct Mass Measurements at the FRS Ion Catcher*. PhD thesis, Justus Liebig University Gießen.

[Jung et al., 1992] Jung, M., Bosch, F., Beckert, K., Eickhoff, H., Folger, H., Franzke, B., Gruber, A., Kienle, P., Klepper, O., Koenig, W., et al. (1992). First observation of bound-state β- decay. *Phys. Rev. Lett.*, 69(15):2164.

[König et al., 1995] König, M., Bollen, G., Kluge, H.-J., Otto, T., and Szerypo, J. (1995). Quadrupole excitation of stored ion motion at the true cyclotron frequency. *Int. J. Mass Spectrom. Ion Proc.*, 142:95–116.

[Kozlov, 2006] Kozlov, V. (2006). *WITCH, a Penning trap for weak interaction studies*. PhD thesis, Catholic University of Leuven.

[Kozlov et al., 2008] Kozlov, V. Y., Beck, M., Coeck, S., Delahaye, P., Friedag, P., Herbane, M., Herlert, A., Kraev, I., Tandecki, M., Van Gorp, S., et al. (2008). The WITCH experiment: Acquiring the first recoil ion spectrum. *Nucl. Instrum. Methods B*, 266(19-20):4515–4520.

[Kramida et al., 2019] Kramida, A., Ralchenko, Y., and Reader, J. (2019). NIST Atomic Spectra Database (Ver. 5.6.1).

[Kubo, 2003] Kubo, T. (2003). In-flight RI beam separator BigRIPS at RIKEN and elsewhere in Japan. *Nucl. Instrum. Methods B*, 204:97–113.

[Lindhard, 1964] Lindhard, J. (1964). Kgl. Danske Videnskap Selsk. Mat. Fys. Medd. 34, No. 14 (1965). *Phys. Lett*, 12:126.

[Lindhard et al., 1996] Lindhard, J., So, A. H., et al. (1996). Relativistic theory of stopping for heavy ions. *Phys. Rev. A*, 53(4):2443.

[Litvinov et al., 2005] Litvinov, Y. A., Geissel, H., Radon, T., Attallah, F., Audi, G., Beckert, K., Bosch, F., Falch, M., Franzke, B., Hausmann, M., Hellström, M., Kerscher, T., Klepper, O., Kluge, H.-J., Kozhuharov, C., Löbner, K. E. G., Münzenberg, G., Nolden, F., Novikov, Y. N., Quint, W., Patyk, Z., Reich, H., Scheidenberger, C., Schlitt, B., Steck, M., Sümmerer, K., Vermeeren, L., Winkler, M., Winkler, T., and Wollnik, H. (2005). Mass measurement of cooled neutron-deficient bismuth projectile fragments with time-resolved Schottky mass spectrometry at the FRS-ESR facility. *Nucl. Phys. A*, 756:3–38.

[Loboda et al., 2000] Loboda, A., Krutchinsky, A., Loboda, O., McNabb, J., Spicer, V., Ens, W., and Standing, K. (2000). Novel Linac II electrode geometry for creating an axial field in a multipole ion guide. *Eur. J. Mass Spectrom.*, 6:531–536.

[Lorusso et al., 2012] Lorusso, G., Becerril, A., Amthor, A., Baumann, T., Bazin, D., Berryman, J. S., Brown, B. A., Cyburt, R. H., Crawford, H. L., Estrade, A., Gade, A., Ginter, T., Guess, C. J., Hausmann, M., Hitt, G. W., Mantica, P. F., Matos, M., Meharchand, R., Minamisono, K., Montes, F., Perdikakis, G., Pereira, J., Portillo, M., Schatz, H., Smith, K., Stoker, J., Stolz, A., and Zegers, R. G. T. (2012). β-delayed proton emission in the ^{100}Sn region. *Phys. Rev. C*, 86:014313.

[Lunardi et al., 1987] Lunardi, S., Daly, P. J., Soramel, F., Signorini, C., Fornal, B., Fortuna, G., Stefanini, A. M., Broda, R., Meczynski, W., and Blomqvist, J. (1987). Decays of $(\nu h_{11/2}^n)^{10+}$ and $(\pi d_{5/2} \nu h_{11/2}^n)^{25/2+}$ isomers in even-A Sn and odd-A Sb nuclei. *Zeitschrift für Physik A Atomic Nuclei*, 328(4):487–492.

[Manura and Dahl, 2006] Manura, D. J. and Dahl, D. A. (2006). *SIMION 8.0 User Manual*. Sci. Instrument Services, Inc., Idaho Nat. Lab.

[Mardor et al., 2018] Mardor, I., Aviv, O., Avrigeanu, M., Berkovits, D., Dahan, A., Dickel, T., Eliyahu, I., Gai, M., Gavish-Segev, I., Halfon, S., Hass, M., Hirsh, T., Kaiser, B., Kijel, D., Kreisel, A., Mishnayot, Y., Mukul, I., Ohayon, B., Paul, M., Perry, A., Rahangdale, H., Rodnizki, J., Ron, G., Sasson-Zukran, R., Shor, A., Silverman, I., Tessler, M., Vaintraub, S., and Weissman, L. (2018). The Soreq Applied Research Accelerator Facility (SARAF) - Overview, Research Programs and Future Plans. *Eur. Phys. J. A*, 54:91.

[Mardor et al., 2019] Mardor, I., Dickel, T., Amanbayev, D., Ayet, S., Beck, S., Benyamin, D., Bergmann, J., Constantin, P., Cuillerier, A. C., Geissel, H., Gröff, L., Hornung, C., Kripko-Koncz, G., Mollaebrahimi, A., Miskun, I., Plaß, W., Pomp, S., Rotaru, A., Scheidenberger, C., amd C. Will, G. S., and For the Super-FRS Experiment Collaboration (2019). Determining spontaneous fission properties by direct mass measurements with the FRS Ion Catcher. *Submitted to EPJ Web of Conferences*.

[Mardor et al., 2017] Mardor, I., Dickel, T., Ayet, S., Bagchi, S., Beck, S., Geissel, H., Greiner, F., Haettner, E., Hornung, C., Kostyleva, D., Kuzminchuk, N., Kindler, B., Lommel, B., Martínez-Pinedo, G., Miskun, I., Mukha, I., Piasetzky, E., Pietri, S., Plaß, W., Pomerantz, I., Prochazka, A., Purushothaman, S., Rappold, C., Saito, T., Scheidenberger, C., Tanaka, Y., Weick, H., and Winfield, J. (2017). A novel method for measuring β-delayed neutron emission. *Proposal to the G-PAC for FAIR Phase-0 Experiments, GSI Darmstadt*.

[Marshall et al., 1998] Marshall, A. G., Hendrickson, C. L., and Jackson, G. S. (1998). Fourier transform ion cyclotron resonance mass spectrometry: A primer. *Mass Spectrom. Rev.*, 17:1–35.

[Masuda and Fujibayashi, 1970] Masuda, S. and Fujibayashi, K. (1970). *J. I. E. E. Jpn.*, 90:126.

[McLuckey, 1992] McLuckey, S. A. (1992). Principles of collisional activation in analytical mass spectrometry. *J. Am. Soc. Mass Spectrom.*, 3(6):599–614.

[Miskun, 2015] Miskun, I. (2015). *Commissioning, performance and possible applications of RFQ mass-filter in the diagnostic unit of the FRS Ion Catcher facility*. Diploma thesis, Tomsk Polytechnical University, Russia.

[Miskun et al., 2019] Miskun, I., Dickel, T., Mardor, I., Hornung, C., Amanbayev, D., Ayet San Andrés, S., Bergmann, J., Ebert, J., Geissel, H., Górska, M., Greiner, F., Haettner, E., Plaß, W. R., Purushothaman, S., Scheidenberger, C., Rink, A.-K., Weick, H., Bagchi, S., Constantin, P., Kaur, S., Lippert, W., Mei, B., Moore, I., Otto, J.-H., Pietri, S., Pohjalainen, I., Prochazka, A., Rappold, C., Reiter, M. P., Tanaka, Y. K., and Winfield, J. S. (2019). A novel method for the measurement of half-lives and decay branching ratios of exotic nuclei. *Eur. Phys. J. A*, 55(9):148.

[Miskun et al., 2015] Miskun, I., Reiter, M. P., Rink, A., Dickel, T., Ayet San Andrés, S., Ebert, J., Geissel, H., Greiner, F., Haettner, E., Hornung, C., Plaß, W. R., Purushothaman, S., and Scheidenberger, C. (2015). An RFQ based beam line and mass filter to improve identification capabilities at the diagnostics unit of the prototype CSC for the LEB. *GSI Sci. Rep. 2014*, 2015-1:146 p.

[Miskun et al., 2017] Miskun, I., Rink, A.-K., Greiner, F., Ayet, S., Bagchi, S., Bergmann, J., Constantin, P., Dickel, T., Ebert, J., Finley, A., Geissel, H., Haettner, E., Hornung, C., Kaur, S., Lippert, W., Mardor, I., Mei, B., Moore, I.,

Otto, J.-H., Pietri, S., Pikhtelev, A., Plaß, W. R., Pohjalainen, I., Prochazka, A., Purushothaman, S., Rappold, C., Reiter, M. P., Scheidenberger, C., Tanaka, Y., Toernqvist, H., Weick, H., Winfield, J. S., Xu, X., and Yavor, M. (2017). Systematic investigations of charge states and purity of projectile and fission fragments extracted from the stopping cell of the (Super-)FRS. *GSI Sci. Rep. 2016*, page 174 p.

[Miyatake et al., 2018] Miyatake, H., Wada, M., Watanabe, X. Y., Hirayama, Y., Schury, P., Ahmed, M., Ishiyama, H., Jeong, S. C., Kakiguchi, Y., Kimura, S., Moon, J. Y., Mukai, M., Oyaizu, M., and Park, J. H. (2018). Present status of the KISS project. *AIP Conf. Proc.*, 1947(1):020018.

[Moon et al., 2011] Moon, C.-B., Dracoulis, G. D., Bark, R. A., Byrne, A. P., Davidson, P. A., Kibedi, T., Lane, G. J., and Wilson, A. N. (2011). Decay schemes of three-quasiparticle isomers in ^{119,121}Sb and ^{121,123}I. *J. Korean Phy. Soc.*, 59:1539–1542.

[Moore et al., 2010] Moore, I., Kessler, T., Sonoda, T., Kudryavstev, Y., Peräjärvi, K., Popov, A., Wendt, K., and Äystö, J. (2010). A study of on-line gas cell processes at IGISOL. *Nucl. Instrum. Methods B*, 268(6):657–670.

[Moré, 1978] Moré, J. J. (1978). The Levenberg-Marquardt algorithm: implementation and theory. In *Numerical analysis*, pages 105–116. Springer.

[Mott, 1929] Mott, N. F. (1929). The scattering of fast electrons by atomic nuclei. *Proc. R. Soc. London*, 124(794):425–442.

[Mukha et al., 2006] Mukha, I., Roeckl, E., Batist, L., Blazhev, A., Doïing, J., Grawe, H., Grigorenko, L., Huyse, M., Janas, Z., Kirchner, R., La Commara, M., Mazzocchi, C., Tabor, S. L., and Van Duppen, P. (2006). Proton–proton correlations observed in two-proton radioactivity of ^{94}Ag. *Nature*, 439:298–302.

[Musumarra et al., 2009] Musumarra, A., Farinon, F., Nociforo, C., Geissel, H., Baur, G., Behr, K.-H., Bonasera, A., Bosch, F., Boutin, D., Brünle, A., et al. (2009). Electron screening effects on α-decay. In *AIP Conf. Proc.*, volume 1165, pages 415–418. AIP.

[Nieto et al., 2009] Nieto, T. K., Souin, J., Eronen, T., Audirac, L., Äystö, J., Blank, B., Elomaa, V.-V., Giovinazzo, J., Hager, U., Hakala, J., et al. (2009). Half-life, branching-ratio, and q-value measurement for the superallowed 0^+ to $0^+\beta^+$ emitter ^{42}Ti. *Phys. Rev. C*, 80(3):035502.

[Nociforo et al., 2012] Nociforo, C., Farinon, F., Musumarra, A., Bosch, F., Boutin, D., Del Zoppo, A., Figuera, P., Fisichella, M., Geissel, H., Knöbel, R., et al. (2012). Measurements of α-decay half-lives at GSI. *Physica Scripta*, 2012(T150):014028.

[Nolden et al., 2000] Nolden, F., Beckert, K., Caspers, F., Franczak, B., Franzke, B.,

Menges, R., Schwinn, A., and Steck, M. (2000). Stochastic cooling at the ESR. *Nucl. Instrum. Methods A*, 441:219–222.

[Paschen, 1889] Paschen, F. (1889). Über die zum Funkenübergang in Luft, Wasserstoff und Kohlensäure bei verschiedenen Drucken erforderliche Potentialdifferenz. *Annalen der Physik*, 273(5):69–96.

[Patyk et al., 2008] Patyk, Z., Geissel, H., Litvinov, Y. A., Musumarra, A., and Nociforo, C. (2008). α-decay half-lives for neutral atoms and bare nuclei. *Phys. Rev. C*, 78(5):054317.

[Paul and Steinwedel, 1953] Paul, W. and Steinwedel, H. (1953). Ein neues Massenspektrometer ohne Magnetfeld. *Z. Naturforschung*, 8a:448–451.

[Petrick, 2008] Petrick, M. (2008). *Aufbau und Erprobung einer neuartigen Separationsmethode für exotische Kerne bei relativistischen Energien*. PhD thesis, Justus Liebig University Gießen.

[Petrick et al., 2008] Petrick, M., Plaß, W., Behr, K.-H., Brünle, A., Caceres, L., Clark, J., Di, Z., Elisseev, S., Facina, M., Fettouhi, A., Geissel, H., Hüller, W., Huyse, M., Karagiannis, C., Kindler, B., Knöbel, R., Kudryavtsev, Y., Kurcewicz, J., Levant, T., Litvinov, Y. A., Lommel, B., Maier, M., Morrissey, D., Münzenberg, G., Portillo, M., Savard, G., Scheidenberger, C., Duppen, P. V., Weick, H., Winkler, M., and Zabransky, B. (2008). Online test of the FRS Ion Catcher at GSI. *Nucl. Instrum. Methods B*, 266:4493–4497.

[Pfützner et al., 1994] Pfützner, M., Geissel, H., Münzenberg, G., Nickel, F., Scheidenberger, C., Schmidt, K.-H., Sümmerer, K., Brohm, T., Voss, B., and Bichsel, H. (1994). Energy deposition by relativistic heavy ions in thin argon absorbers. *Nucl. Instrum. Methods B*, 86:213–218.

[Pfützner et al., 2012] Pfützner, M., Karny, M., Grigorenko, L., and Riisager, K. (2012). Radioactive decays at limits of nuclear stability. *Reviews of modern physics*, 84(2):567.

[Pian et al., 2017] Pian, E., d'Avanzo, P., Benetti, S., Branchesi, M., Brocato, E., Campana, S., Cappellaro, E., Covino, S., d'Elia, V., Fynbo, J., et al. (2017). Spectroscopic identification of r-process nucleosynthesis in a double neutron-star merger. *Nature*, 551(7678):67.

[Pietri, 2015] Pietri, S. (2015). Private communication.

[Plaß, 2001] Plaß, W. R. (2001). *The Dependence of RF Ion Trap Mass Spectrometer Performance on Electrode Geometry and Collisional Processes*. PhD thesis, Justus Liebig University Gießen.

[Plaß et al., 2018] Plaß, W. R., Amanbayev, D., Andelkovic, Z., Ayet San Andrés,

S., Bagchi, S., Balabanski, D., Beck, S., Bergmann, J., Block, M., Blum, D., Constantin, P., Danaila, S., Dendooven, P., Dickel, T., Dort, K., Ebert, J., Geissel, H., Greiner, F., Gröff, L., Haettner, E., Harakeh, M. N., Heisse, F., Herfurth, F., Hornung, C., Jesch, C., Kalantar-Nayestanaki, N., Mardor, I., Merisanu, M., Miskun, I., Moore, I. D., Petrick, M., Pietri, S., Pohjalainen, I., Purushothaman, S., Ranjan, M., Reiter, M. P., Rink, A.-K., Schäfer, D., Scheidenberger, C., Spataru, A., State, A., Weick, H., Winfield, J. S., Winkler, M., and Yavor, M. I. (2018). *Technical Report for the Design, Construction and Commissioning of the Cryogenic Stopping Cell of the Super-FRS*. Technical design report, Justus Liebig University Gießen.

[Plaß et al., 2015] Plaß, W. R., Dickel, T., Ayet San Andres, S., Ebert, J., Greiner, F., Hornung, C., Jesch, C., Lang, J., Lippert, W., Majoros, T., Short, D., Geissel, H., Haettner, E., amd A.-K. Rink, M. P. R., Scheidenberger, C., and Yavor, M. I. (2015). High-performance multiple-reflection time-of-flight mass spectrometers for research with exotic nuclei and for analytical mass spectrometry. *Phys. Scr. T*, 166:014069.

[Plaß et al., 2008a] Plaß, W. R., Dickel, T., Czok, U., Geissel, H., Petrick, M., Reinheimer, K., Scheidenberger, C., and Yavor, M. I. (2008a). Isobar separation by time-of-flight mass spectrometry for low-energy radioactive ion beam facilities. *Nucl. Instrum. Methods B*, 266:4560–4564.

[Plaß et al., 2008b] Plaß, W. R., Dickel, T., Fabian, B., and Haettner, E. (2008b). An advanced concept for mass spectrometry simulations – the Ion Trajectory Simulation program ITSIM 6. In *Proceedings of the 56th ASMS Conference on Mass Spectrometry and Allied Topics*, page MP 015, Denver, USA.

[Plaß et al., 2019] Plaß, W. R., Dickel, T., Mardor, I., Pietri, S., Geissel, H., Scheidenberger, C., Amanbayev, D., San Andrés, S. A., Äystö, J., Balabanski, D. L., et al. (2019). The science case of the FRS Ion Catcher for FAIR Phase-0. *Hyperfine Interactions*, 240(1):73.

[Plaß et al., 2007] Plaß, W. R., Dickel, T., Petrick, M., Boutin, D., Di, Z., Fleckenstein, T., Geissel, H., Jesch, C., Scheidenberger, C., and Wang, Z. (2007). An RF quadrupole-time-of-flight system for isobar-separation and multiplexed low energy rare-isotope beam experiments. *Eur. Phys. J. Special Topics*, 150:367–368.

[Plaß et al., 2013a] Plaß, W. R., Dickel, T., Purushothaman, S., Dendooven, P., Geissel, H., Ebert, J., Haettner, E., Jesch, C., Ranjan, M., Reiter, M. P., Weick, H., Amjad, F., Ayet, S., Diwisch, M., Estrade, A., Farinon, F., Greiner, F., Kalantar-Nayestanaki, N., Knöbel, R., Kurcewicz, J., Lang, J., Moore, I., Mukha, I., Nociforo, C., Petrick, M., Pfuetzner, M., Pietri, S., Prochazka, A., Rink, A.-K., Rinta-Antila, S., Schäfer, D., Scheidenberger, C., Takechi, M., Tanaka, Y. K., Winfield, J. S., and Yavor, M. I. (2013a). The FRS Ion Catcher - a facility for high-precision experiments with stopped projectile and fission fragments. *Nucl. Instrum. Methods B*, 317:457–462.

[Plaß et al., 2013b] Plaß, W. R., Dickel, T., and Scheidenberger, C. (2013b). Multiple-reflection time-of-flight mass spectrometry. *Int. J. Mass Spectrom.*, 349:134–144.

[Pohjalainen, 2018] Pohjalainen, I. (2018). *Gas-phase chemistry, recoil source characterization and in-gas-cell resonance laser ionization of actinides at IGISOL.* PhD thesis, University of Jyväskylä.

[Porquet et al., 2005] Porquet, M. G., Venkova, T., Lucas, R., Astier, A., Bauchet, A., Deloncle, I., Prévost, A., Azaiez, F., Barreau, G., Bogachev, A., Buforn, N., Buta, A., Curien, D., Doan, T. P., Donadille, L., Dorvaux, O., Duchêne, G., Durell, J., Ethvignot, T., Gall, B. P. J., Grimwood, D., Houry, M., Khalfallah, F., Korten, W., Lalkovski, S., Le Coz, Y., Meyer, M., Minkova, A., Piqueras, I., Redon, N., Roach, A., Rousseau, M., Schulz, N., Smith, A. G., Stézowski, O., Theisen, C., and Varley, B. J. (2005). High-spin structures of $^{121,123,125,127}_{51}$Sb nuclei: Single proton and core-coupled states. *Eur. Phys. J. A*, 24(1):39–49.

[Poth, 1990] Poth, H. (1990). Electron cooling: theory, experiment, application. *Physics reports*, 196(3-4):135–297.

[Purushothaman et al., 2017a] Purushothaman, S., Ayet San Andrés, S., Bergmann, J., Dickel, T., Ebert, J., Geissel, H., Hornung, C., Plaß, W. R., Rappold, C., Scheidenberger, C., Tanaka, Y. K., and Yavor, M. I. (2017a). Hyper-EMG: A new probability distribution function composed of Exponentially Modified Gaussian distributions to analyze asymmetric peak shapes in high-resolution time-of-flight mass spectrometry. *Int. J. Mass Spectrom.*, 421:245–254.

[Purushothaman et al., 2017b] Purushothaman, S., Dickel, T., Ayet, S., Bagchi, S., Behr, K.-H., Bergmann, J., Blatz, T., Constantin, P., Ebert, J., Finley, A., Geissel, H., Greiner, F., Haettner, E., Hornung, C., Kaur, S., Lippert, W., Lommel, B., Mardor, I., Mei, B., Miskun, I., Moore, I., Otto, J.-H., Pietri, S., Pikhtelev, A., Plaß, W. R., Pohjalainen, I., Prochazka, A., Rappold, C., Reiter, M. P., Rink, A.-K., Scheidenberger, C., Szczepanczyk, B., Tanaka, Y., Weick, H., and Winfield, J. S. (2017b). A gas degrader for the Low-Energy Branch of the Super-FRS at FAIR. *GSI Sci. Rep. 2016*, page 180.

[Purushothaman et al., 2013] Purushothaman, S., Reiter, M. P., Haettner, E., Dendooven, P., Dickel, T., Geissel, H., Ebert, J., Jesch, C., Plaß, W. R., Ranjan, M., Weick, H., Amjad, F., Ayet, S., Diwisch, M., Estrade, A., Farinon, F., Greiner, F., Kalantar-Nayestanaki, N., Knöbel, R., Kurcewicz, J., Lang, J., Moore, I., Mukha, I., Nociforo, C., Petrick, M., Pfuetzner, M., Pietri, S., Prochazka, A., Rink, A.-K., Rinta-Antila, S., Scheidenberger, C., Takechi, M., Tanaka, Y. K., Winfield, J. S., and Yavor, M. I. (2013). First online results of a cryogenic stopping cell with short-lived heavy uranium fragments produced at 1000 MeV/u. *Eur. Phys. Lett.*, 104:42001.

[Ranjan et al., 2015] Ranjan, M., Dendooven, P., Purushothama, S., Dickel, T., Reiter, M. P., Ayet, S., Haettner, E., Moore, I. D., Kalantar-Nayestanaki, N., Geissel,

H., Plaß, W. R., Schäfer, D., Scheidenberger, C., Schreuder, F., Timersma, H., Van de Walle, J., and Weick, H. (2015). Design, construction and cooling system performance of a prototype cryogenic stopping cell for the Super-FRS at FAIR. *Nucl. Instrum. Methods A*, 770:87–97.

[Ranjan et al., 2011] Ranjan, M., Purushothaman, S., Dickel, T., Geissel, H., Plaß, W. R., Schäfer, D., Scheidenberger, C., Van de Walle, J., Weick, H., and Dendooven, P. (2011). New stopping cell capabilities: RF carpet performance at high gas density and cryogenic operation. *Eur. Phys. Lett.*, 96:52001.

[*R* Core Team, 2018] *R* Core Team (2018). *R: A Language and Environment for Statistical Computing*. *R* Foundation for Statistical Computing, Vienna, Austria.

[Reiter, 2011] Reiter, M. P. (2011). *Simulation of the cryogenic stopping cell of the FRS Ion Catcher experiment and construction of a novel RFQ beam line system.* Master thesis, Justus Liebig University Gießen.

[Reiter, 2015] Reiter, M. P. (2015). *Pilot Experiments with Relativistic Uranium Projectile and Fission Fragments Thermalized in a Cryogenic Gas-Filled Stopping Cell.* PhD thesis, Justus Liebig University Gießen.

[Reiter et al., 2016] Reiter, M. P., Rink, A.-K., Dickel, T., Haettner, E., Heiße, F., Plaß, W. R., Purushothaman, S., Amjad, F., Andrés, S. A. S., Bergmann, J., Blum, D., Dendooven, P., Diwisch, M., Ebert, J., Geissel, H., Greiner, F., Hornung, C., Jesch, C., Kalantar-Nayestanaki, N., Knöbel, R., Lang, J., Lippert, W., Miskun, I., Moore, I. D., Nociforo, C., Petrick, M., Pietri, S., Pfützner, M., Pohjalainen, I., Prochazka, A., Scheidenberger, C., Takechi, M., Tanaka, Y. K., Weick, H., Winfield, J. S., and Xu, X. (2016). Rate capability of a cryogenic stopping cell for uranium projectile fragments produced at 1000 MeV/u. *Nucl. Instrum. Methods B*, 376:240–245.

[Rink, 2017] Rink, A.-K. (2017). *Mass and Life-Time Measurement of the 1.7 ms* ^{215}*Po Isotope - A crucial Test of the Novel Concept of the Cryogenic Ion Catcher for the Super FRS at GSI-FAIR.* PhD thesis, Justus Liebig University Gießen.

[Rissanen et al., 2007] Rissanen, J., Elomaa, V.-V., Eronen, T., Hakala, J., Jokinen, A., Rahaman, S., Rinta-Antila, S., and Äystö, J. (2007). Conversion electron spectroscopy of isobarically purified trapped radioactive ions. *Eur. Phys. J. A*, 34(2):113–118.

[Rodriguez et al., 2010] Rodriguez, D. et al. (2010). MATS and LaSpec: High-precision experiments using ion traps and lasers at FAIR. *Eur. Phys. J. Special Topics*, 183:1–123.

[Savard et al., 1991] Savard, G., Becker, S., Bollen, G., Kluge, H. J., Moore, R. B., Otto, T., Schweikhard, L., Stolzenberg, H., and Wiess, U. (1991). A new cooling technique for heavy ions in a Penning trap. *Phys. Lett. A*, 158(5):247–252.

[Scheidenberger et al., 1994] Scheidenberger, C., Geissel, H., Mikkelsen, H., Nickel, F., Brohm, T., Folger, H., Irnich, H., Magel, A., Mohar, M., Münzenberg, G., et al. (1994). Direct observation of systematic deviations from the bethe stopping theory for relativistic heavy ions. *Phys. Rev. Lett.*, 73(1):50.

[Scheidenberger et al., 1996] Scheidenberger, C., Geissel, H., Mikkelsen, H., Nickel, F., Czajkowski, S., Folger, H., Irnich, H., Münzenberg, G., Schwab, W., Stöhlker, T., et al. (1996). Energy-loss-straggling experiments with relativistic heavy ions in solids. *Phys. Rev. Lett.*, 77(19):3987.

[Schury et al., 2006] Schury, P., Bollen, G., Block, M., Morrissey, D., Ringle, R., Prinke, A., Savory, J., Schwarz, S., and Sun, T. (2006). Beam purification techniques for low energy rare isotope beams from a gas cell. *Hyperfine Interact.*, 173:165–170.

[Shroy et al., 1979] Shroy, R. E., Gaigalas, A. K., Schatz, G., and Fossan, D. B. (1979). High-spin states in odd-mass $^{113-119}$Sb: $\Delta j = 1$ bands on $9/2^+$ proton-hole states. *Phys. Rev. C*, 19:1324–1343.

[Simon, 2008] Simon, A. (2008). *Entwicklung und Test eines CFK-basierten RF-Quadrupols für ein Multireflektions-Flugzeitmassenspektrometer*. Bachelor thesis, Justus Liebig University Gießen.

[Steck et al., 1996] Steck, M., Beckert, K., Eickhoff, H., Franzke, B., Nolden, F., Reich, H., Schlitt, B., and Winkler, T. (1996). Anomalous temperature reduction of electron-cooled heavy ion beams in the storage ring ESR. *Phys. Rev. Lett.*, 77:3803.

[Sternheimer and Peierls, 1971] Sternheimer, R. and Peierls, R. (1971). General expression for the density effect for the ionization loss of charged particles. *Phys. Rev. B*, 3(11):3681.

[Stolz et al., 1999] Stolz, A., Faestermann, T., Körner, H.-J., Schneider, R., Wefers, E., and Winkler, S. (1999). A detector system for the identification of relativistic heavy ions at high rates. *GSI Sci. Rep. 1998*, page 174.

[Symochko et al., 2009] Symochko, D., Browne, E., and Tuli, J. (2009). Nuclear data sheets for a = 119. *Nuclear Data Sheets*, 110(11):2945 – 3105. Data extracted from the ENSDF database, version 2019-02-14.

[Takamine et al., 2005] Takamine, A., Wada, M., Ishida, Y., Nakamura, T., Okada, K., Yamazaki, Y., Kambara, T., Kanai, Y., Kojima, T. M., Nakai, Y., Oshima, N., Yoshida, A., Kubo, T., Ohtani, S., Noda, K., Katayama, I., Hostain, P., Varentsov, V., and Wollnik, H. (2005). Space-charge effects in the catcher gas cell of a RF ion guide. *Rev. Sci. Instrum.*, 76:103503.

[Takamine et al., 2007] Takamine, A., Wada, M., Ishida, Y., Nakamura, T., Okada,

K., Yamazaki, Y., Kanai, Y., Kojima, T. M., Yoshida, A., Kubo, T., Ohtani, S., Noda, K., Katayama, I., Lioubimov, V., Schuessler, H. A., Varentsov, V., and Wollink, H. (2007). Improvement of the slow RI beam transport using Carbon-OPIG. *RIKEN Accel. Prog. Rep.*, 40.

[Tarasov and Bazin, 2008] Tarasov, O. B. and Bazin, D. (2008). LISE++: Radioactive beam production with in-flight separators. *Nucl. Instrum. Methods B*, 266(19-20):4657–4664.

[Thoennessen, 2013] Thoennessen, M. (2013). Current status and future potential of nuclide discoveries. *Rep. Prog. Phys.*, 76(5):056301.

[Tolmachev et al., 1997] Tolmachev, A. V., Chernushevich, I. V., Dodonov, A. F., and Standing, K. G. (1997). A collisional focusing ion guide for coupling an atmospheric pressure ion source to a mass spectrometer. *Nucl. Instrum. Methods B*, 124:112–119.

[Trötscher et al., 1992] Trötscher, J., Balog, K., Eickhoff, H., Franczak, B., Franzke, B., Fujita, Y., Geissel, H., Klein, C., Knollmann, J., Kraft, A., Löbner, K. E. G., Magel, A., Münzenberg, G., Przewloka, A., Rosenauer, D., Schäfer, H., Sendor, M., Vieira, D. J., Vogel, B., Winkelmann, T., and Wollnik, H. (1992). Mass measurements of exotic nuclei at the ESR. *Nucl. Instrum. Methods B*, 70:455–458.

[Viehland, 2012] Viehland, L. A. (2012). Zero-field mobilities in helium: highly accurate values for use in ion mobility spectrometry. *Int. J. Ion Mobil. Spec.*, 15:21–29.

[Wada, 2013] Wada, M. (2013). Genealogy of gas cells for low-energy RI-beam production. *Nucl. Instrum. Methods B*, 317:450–456.

[Wada et al., 2003] Wada, M., Ishida, Y., Nakamura, T., Yamazaki, Y., Kambara, T., Ohyama, H., Kanai, Y., Kojima, T. M., Nakai, Y., Ohshima, N., Yoshida, A., Kubo, T., Matsuo, Y., Fukuyama, Y., Okada, K., Sonoda, T., Ohtani, S., Noda, K., Kawakami, H., and Katayama, I. (2003). Slow RI-beams from projectile fragment separators. *Nucl. Instrum. Methods B*, 204:570–581.

[Wang et al., 2017] Wang, M., Audi, G., Kondev, F. G., Huang, W. J., Naimi, S., and Xu, X. (2017). The AME2016 atomic mass evaluation (II). Tables, graphs and references. *Chinese Phys. C*, 41(3).

[Weber et al., 2013] Weber, C., Müller, P., and Thirolf, P. (2013). Developments in Penning trap (mass) spectrometry at MLLTRAP: Towards in-trap decay spectroscopy. *Int. J. Mass Spectrom.*, 349:270–276.

[Weick, 2019] Weick, H. (2019). Private communication.

[Weick et al., 2018] Weick, H., Geissel, H., Iwasa, N., Scheidenberger, C., and Sanchez, J. R. (2018). Improved accuracy of the code ATIMA for energy loss of heavy ions in matter. *GSI Sci. Rep. 2017*, 2018-1:130 p.

[Weick et al., 2000] Weick, H., Geissel, H., Scheidenberger, C., Attallah, F., Baumann, T., Cortina, D., Hausmann, M., Lommel, B., Münzenberg, G., Nankov, N., Nickel, F., Radon, T., Schatz, H., Schmidt, K., Stadlmann, J., Sümmerer, K., Winkler, M., and Wollnik, H. (2000). Slowing down of relativistic few-electron heavy ions. *Nucl. Instrum. Methods B*, 164-165:168–179.

[Weick et al., 2002] Weick, H., Sørensen, A., Geissel, H., Scheidenberger, C., Attallah, F., Chichkine, V., Elisseev, S., Hausmann, M., Irnich, H., Litvinov, Y., et al. (2002). Energy-loss straggling of (200–1000) mev/u uranium ions. *Nucl. Instrum. Methods B*, 193(1-4):1–7.

[Weissman et al., 2002] Weissman, L., Ames, F., Äysto, J., Forstner, O., Reisinger, K., Rinta-Antila, S., and ISOLDE, R. (2002). In-trap conversion electron spectroscopy. *Nucl. Instrum. Methods A*, 492(3):451–463.

[Will, 2019] Will, C. (2019). *Achieving One Million Mass Resolving Power with a Multiple-Reflection Time-of-Flight Mass Spectrometer*. Master thesis, Justus Liebig University Gießen.

[Winfield et al., 2013] Winfield, J. S., Geissel, H., Gerl, J., Münzenberg, G., Nociforo, C., Plaß, W. R., Scheidenberger, C., Weick, H., Winkler, M., and Yavor, M. I. (2013). A versatile high-resolution magnetic spectrometer for energy compression, reaction studies and nuclear spectroscopy. *Nucl. Instrum. Methods A*, 704:76–83.

[Wolf et al., 2016] Wolf, R., Atanasov, D., Blaum, K., Kreim, S., Lunney, D., Manea, V., Rosenbusch, M., Schweikhard, L., Welker, A., Wienholtz, F., and Zuber, K. (2016). Background-free beta-decay half-life measurements by in-trap decay and high-resolution MR-ToF mass analysis. *Nucl. Instrum. Methods B*, 376:275 – 280.

[Wollnik and Przewloka, 1990] Wollnik, H. and Przewloka, M. (1990). Time-of-flight mass spectrometers with multiply reflected ion trajectories. *Int. J. Mass Spectrom. Ion Processes*, 96:267–274.

[Wu et al., 2006] Wu, G., Cooks, R. G., Ouyang, Z., Yu, M., Chappell, W. J., and Plass, W. R. (2006). Ion trajectory simulation for electrode configurations with arbitrary geometries. *J. Am. Soc. Mass Spectrom.*, 17:1216–1228.

[Yavor, 2009] Yavor, M. (2009). *Optics of Charged Particle Analyzers*, volume 157 of *Advances in Imaging and Electron Physics*. Academic Press, Elsevier, Amsterdam.

[Yavor et al., 2015] Yavor, M. I., Plaß, W. R., Dickel, T., Geissel, H., and Scheidenberger, C. (2015). Ion-optical design of a high-performance multiple-reflection time-of-flight mass spectrometer and isobar separator. *Int. J. Mass Spectrom.*, 381-382:1–9.

[Yee et al., 2013] Yee, R. M., Scielzo, N. D., Bertone, P. F., Buchinger, F., Caldwell, S., Clark, J. A., Deibel, C. M., Fallis, J., Greene, J. P., Gulick, S., Lascar, D.,

Levand, A. F., Li, G., Norman, E. B., Pedretti, M., Savard, G., Segel, R. E., Sharma, K. S., Sternberg, M. G., Van Schelt, J., and Zabransky, B. J. (2013). β-delayed neutron spectroscopy using trapped radioactive ions. *Phys. Rev. Lett.*, 110:092501.

[Ziegler and Biersack, 1985] Ziegler, J. F. and Biersack, J. P. (1985). The stopping and range of ions in matter. In *Treatise on heavy-ion science*, pages 93–129. Springer.

[Ziegler et al., 2010] Ziegler, J. F., Ziegler, M. D., and Biersack, J. P. (2010). SRIM - the stopping and range of ions in matter (2010). *Nucl. Instrum. Methods B*, 268:1818–1823.